University of California
Santa Barbara

Thermodynamics and Creep Behavior of $L1_2$-containing Co-base Superalloys

A dissertation submitted in partial satisfaction
of the requirements for the degree

Doctor of Philosophy
in
Materials

by

Robert K. Rhein

Committee in charge:

Professor Tresa M. Pollock, Chair
Professor Anton Van der Ven
Professor Matthew R. Begley
Professor Linda R. Petzold

March 2019

The Dissertation of Robert K. Rhein is approved.

Professor Anton Van der Ven

Professor Matthew R. Begley

Professor Linda R. Petzold

Professor Tresa M. Pollock, Committee Chair

January 2019

Thermodynamics and Creep Behavior of $L1_2$-containing Co-base Superalloys

by

Robert K. Rhein

Acknowledgements

Before starting out on the process toward achieving my Ph.D., I did not have a very well-developed sense of the immense task that lay ahead of me. The past six years have taught me a great deal, both professionally and personally. Without the support of my family, friends, and colleagues, this degree would have been unobtainable and I am deeply grateful for their support. I would like to thank several of them here.

I would first like to thank my family, especially my brother, James, and my parents, Charles and Christine. They have supported me immensely through this endeavor and I could not have done it without them. I also thank my many incredible teachers and professors who helped guide my interest in science and materials throughout my earlier education.

At the University of California, Santa Barbara, I would like to thank several people. I would first like to thank the students in my cohort, especially Will, Brent, and Jackie. I also want to thank my housemates over the years, including Gary, Peter, Leah, Greg, Marissa, Dan, Doug, Nathan, and Elayne. I'd like to thank Anirudh and Jon for their immense patience and assistance. Thanks also to all the colleagues working on cobalt superalloys, especially Mike, Colin, and Sean. I'd also like to thank all of the people who I've explored California with over the past six years, especially the backpacking crew.

I'd like to thank Chris Torbet for his patience and assistance over the years. I have been incredibly fortunate to have been taught and advised by several outstanding professors at UCSB. Thank you to Prof. Linda Petzold and Prof. Matthew Begley for serving on my committee. A huge thank you to Prof. Anton Van der Ven for his assistance in so many aspects of this work. Lastly, I want to deeply thank Prof. Tresa Pollock for her patience, guidance, and support as my advisor during the past six years. I can't adequately convey what it has meant to me.

I also want to acknowledge the National Science Foundation for funding this work. Thanks again to all and to those I may not have mentioned.

Curriculum Vitæ

Robert K. Rhein

Education

2019	Ph.D. in Materials (Expected), University of California, Santa Barbara.
2010	M.S. in Materials Science and Engineering, University of Michigan.
2008	B.S. in Materials Science and Engineering, University of Michigan.

Publications

6. L. Feng, D. Lv, **R.K. Rhein**, J.G. Goiri, M.S. Titus, A. Van der Ven, T.M. Pollock, and Y. Wang. "Shearing of γ' Particles in Co-base and Co-Ni-base superalloys," *Acta Materialia*. 161 (2018). [**doi**]
5. **R.K. Rhein**, P.G. Callahan, S.P. Murray, J.-C. Stinville, M.S. Titus, A. Van der Ven, and T.M. Pollock. "Creep Behavior of Quinary γ' Strengthened Co-based Superalloys," *Metallurgical and Materials Transactions A*. 49 (9) (2018). [**doi**]
4. M.S. Titus, **R.K. Rhein**, P.B. Wells, P.C. Dodge, G.B. Viswanathan, M.J. Mills, and T.M. Pollock. "Solute Segregation and Deviation from Bulk Thermodynamics at Nanoscale Crystalline Defects," *Science Advances*. 2 (12) (2016). [**doi**]
3. C.A. Stewart, **R.K. Rhein**, A. Suzuki, T.M. Pollock, and C.G. Levi. "Oxide Scale Formation in Novel γ - γ' Cobalt-Based Alloys," *Superalloys 2016*. 991-999 (2016). [**doi**]
2. **R.K. Rhein**, P.C. Dodge, M.H. Chen, M.S. Titus, T.M. Pollock, and A. Van der Ven. "Role of Vibrational and Configurational Excitations in Stabilizing the $L1_2$ Structure in Co-rich Co-Al-W alloys," *Physical Review B*. 92, 174117- (2015). [**doi**]
1. **R.K. Rhein**, M.D. Novak, C.G. Levi, and T.M. Pollock. "Bimetallic Low Thermal-Expansion Panels of Co-base and Silicide-Coated Nb-base Alloys for High-Temperature Structural Applications," *Materials Science and Engineering: A*. 528, 3973-3980 (2011). [**doi**]

Abstract

Thermodynamics and Creep Behavior of $L1_2$-containing Co-base Superalloys

by

Robert K. Rhein

$L1_2$-containing Co-base superalloys are of significant interest due to their high temperature strength and oxidation resistance. Previous research has shown that this class of alloys has demonstrated creep performance comparable to second-generation Ni-base superalloys. Like Ni-base superalloys, Co-base superalloys derive their strength from a two-phase γ-γ' microstructure consisting of cuboidal ordered $L1_2$ precipitates embedded within a solid solution matrix. The thermal stability of this $L1_2$ precipitate phase is therefore of great importance if these alloys are to retain their mechanical properties in high-temperature applications. Topics explored in this study include: (i) thermal stability of the $L1_2$ γ' precipitate phase, (ii) the creep performance of quinary Co-base superalloys, (iii) the deformation mechanisms present in these alloys, and (iv) oxidation behavior of these alloys.

The primary challenge in developing Co-base superalloys is to stabilize the $L1_2$ γ' phase. It has been shown that Co-base superalloys exhibit lower γ' solvus temperatures than their Ni-base counterparts. A comprehensive first-principles study was performed for the Co-Al-W ternary system in order to determine the stability of the $L1_2$ γ' phase field. This analysis was first performed on the 75 at% Co pseudobinary line and it was found that the $L1_2$ γ' phase is indeed stable at W-rich compositions at temperatures above 600 °C. This was then extended to the full Co-Al-W ternary system where a small phase field of $L1_2$ was also found at high temperature.

Higher-order d-block alloying additions were identified using subsequent first-principles

calculations and single crystals of quinary Co-base superalloy compositions were cast using the conventional Bridgman process. Creep deformation mechanisms were characterized, with lower 900 °C temperature deformation dominated by antiphase boundary (APB) formation and higher 982 °C temperature deformation dominated by superlattice intrinsic stacking fault (SISF) formation. Additional simulations were performed using generalized stacking fault (GSF) surfaces as input to further investigate deformation mechanisms during creep. A parametric study was conducted in which different dislocation configurations interacted with different precipitate morphologies. The formation of SISFs is a dominant creep deformation mechanism in Co-base superalloys, and the solute segregation around them is an important consideration. To this end, experimental and modeling efforts were performed in order to qualitatively predict the changes in composition near these faults. Oxidation behavior of several CoNi-base superalloy compositions were additionally investigated to determine which compositions form a continuous, protective α-Al_2O_3 scale.

Contents

Chapter 1

Introduction: Superalloy Chemistry and Applications

1.1 Gas Turbine Engines

Land-based gas turbine engines are a major source of U.S. electrical production. The advent of hydraulic fracturing in recent years has greatly increased the availability of the fuel for these engines, accounting for a significant rise in the amount of electricity generated from natural gas, as seen in Figure 1.1 [1]. These trends are projected to continue, with natural gas consumption becoming the dominant means of electricity generation in the United States in the coming decades. As gas turbine engines convert thermal energy into mechanical energy, the thermal efficiency of these engines can be roughly taken from the Carnot cycle [2]. The most obvious means of increasing efficiency in these engines is therefore to increase the operating temperature in the high pressure section of the turbine. For a combined-cycle land-based gas turbine engine, a 10 °C increase in operating temperature roughly yields a 1% increase in efficiency. Taken over the entire power generation sector, an increase in efficiency of 1% would yield significant

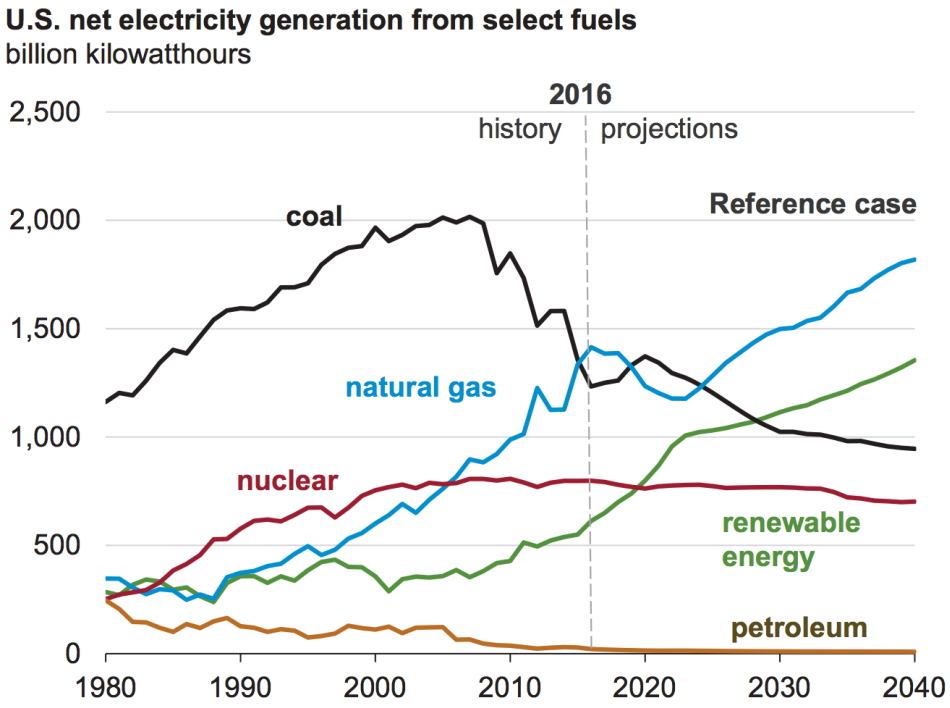

Figure 1.1: Historical and projected domestic electrical production by source. [1]

fuel cost savings of $60 billion over 15 years [3]. The operating temperature and attendant efficiency of these engines are limited by the materials properties of the high-temperature components.

The blade components within the high-pressure turbine section are subject to the most aggressive thermomechanical environment during operation of gas turbine engines. The materials in these blades have to satisfy a number of design criteria, including high strength and resistance to oxidation, creep, and fatigue. The gas temperatures within the high-pressure turbine section can reach 1500 °C, and so it is critical that these materials retain their properties at a significant fraction of their melting point. Ni-base superalloys are the typical material choice for the blade components as they are able to withstand aggressive mechanical loads at these elevated temperatures. However, further increases in operating temperature and turbine energy efficiency are constrained by the melting

point of Ni-base superalloys, motivating the search for alternative materials systems for these components.

1.2 Ni-base Superalloys

1.2.1 Processing Development

Superalloys in use today reflect over 70 years of scientific and engineering advances in alloy chemistry and processing. After World War II, the development of jet turbine engines necessitated the search for new materials systems that would be able to withstand aggressive thermomechanical environments. These first superalloys were typically wrought, and several distinct Fe-, Co-, and Ni-based compositions were developed. Advances in alloy chemistry in the subsequent decades led to alloys with significantly improved mechanical properties due to solid solution and precipitate strengthening. Ni-base superalloys came to dominate the market for blading applications due to their ability to balance several favorable properties, including corrosion resistance, mechanical strength, fatigue resistance, and microstructural stability [2].

The advent of Ni-base superalloys with significant amounts of precipitate phases made processing wrought alloys difficult, and necessitated the development of new processing techniques. Figure 1.2 shows the normalized improvement in creep life for Ni-base superalloys as a function of time as improved processing techniques were developed [2]. Producing Ni-base superalloy blades via vacuum induction casting allowed for higher purity components, leading to further improvements in creep life [4]. Additional developments in casting methods allowed for directional solidification of grains during processing, eliminating transverse grain boundaries that weaken creep performance. From there, grain boundaries in blade components were completely eliminated using single crystal casting

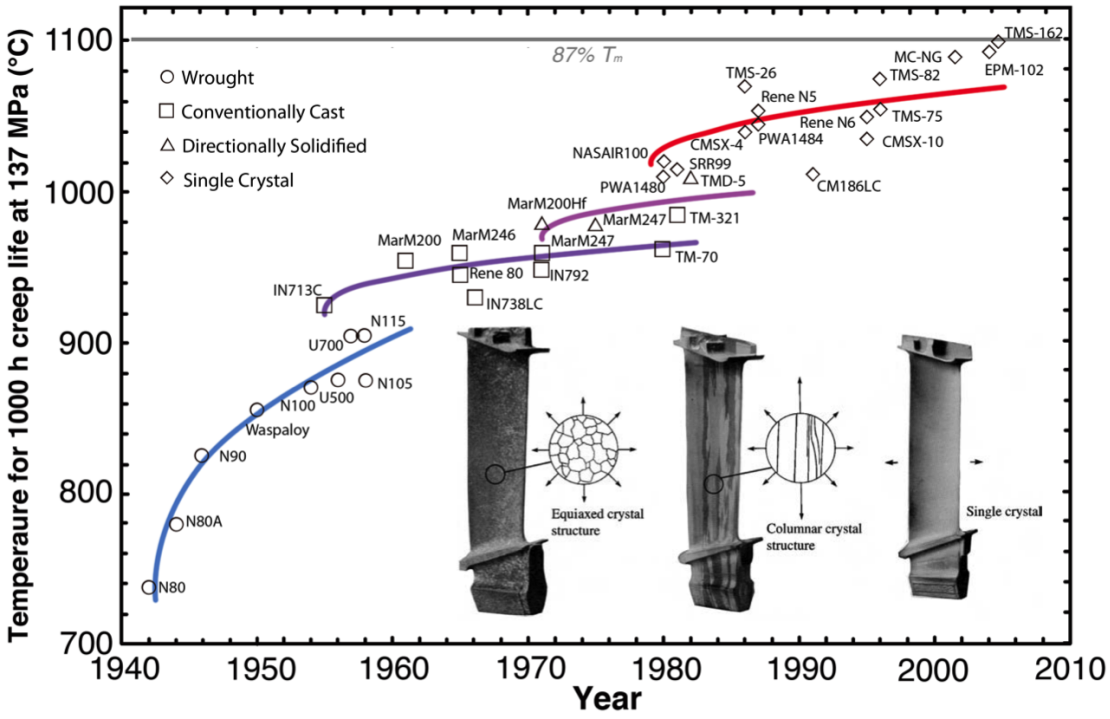

Figure 1.2: Evolution of creep performance of Ni-base superalloys by year, normalized at 1000h and 137 MPa of creep life for comparative purposes. Different processing techniques are denoted by separate lines, coloring courtesy of Michael Titus. Adapted from [2].

techniques, allowing for improved alloy chemistry as the incorporation of grain-boundary strengthening elements was no longer a requirement [5]. These single crystal superalloys have the most favorable creep and fatigue properties as the elimination of grain boundaries makes them more resistant to mechanical deformation [2].

1.2.2 Alloy Chemistry and Microstructure

The chemistry of modern Ni-base superalloys is based on the Ni-Al binary system, as shown in Figure 1.3. If the Ni-rich section of the phase diagram is considered, it is apparent that there is significant solid solubility of Al within the face-centered cubic (FCC) γ Ni phase. Increasing Al content further, a two phase γ-γ' phase field is present.

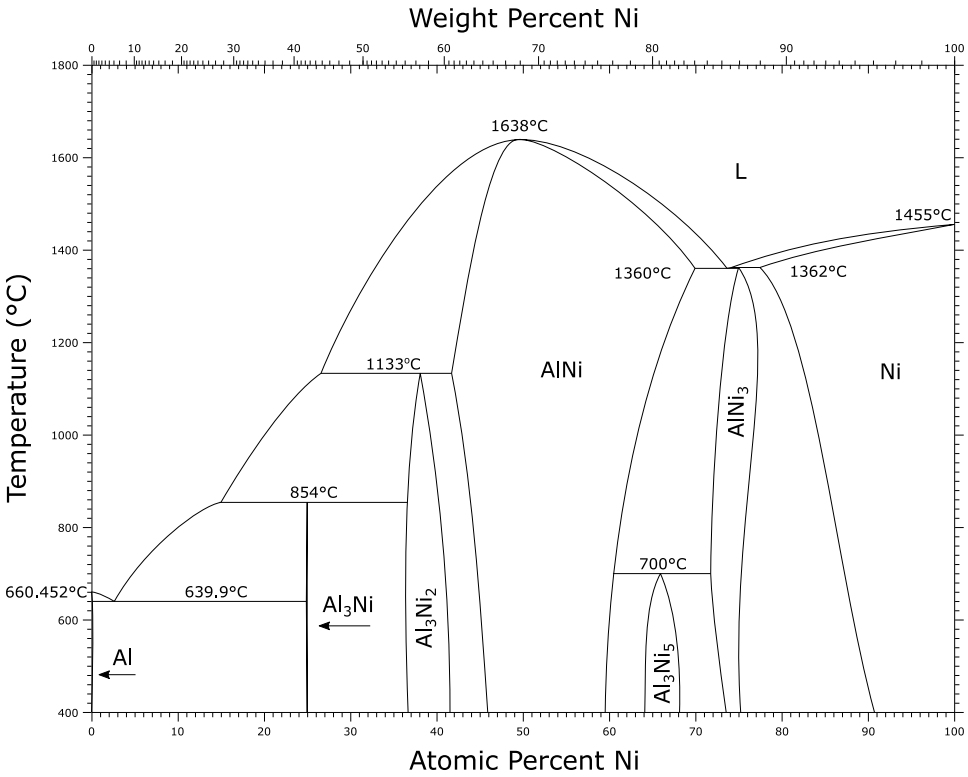

Figure 1.3: Binary phase diagram of the Al-Ni system adapted from Okamoto. Adapted image courtesy of William Lenthe. [7]

The nominally stoichiometric Ni_3Al γ' phase is an ordered intermetallic $L1_2$ structure and typically exists as coherently embedded precipitates within the disordered γ matrix phase [2]. Strengthening of the overall superalloy is achieved primarily by increasing the volume fraction of the Ni_3Al γ' phase and the inclusion of solid solution strengthening elements in the γ matrix phase [6].

A number of additional alloying elements are added to this baseline binary system to improve various properties. Cr is often added in order to improve oxidation and corrosion resistance. Elements such as W, Ta, Mo, Re, and Ru are included in order to impede dislocation motion in the γ matrix phase via solid solution strengthening. In the case of polycrystalline superalloys, elements such as B and C are added to limit the susceptibility of grain boundaries to damage. Relatively small amounts of these elements readily form

borides and carbides. These phases precipitate in the liquid during solidification or subsequently in the solid state and segregate to high angle grain boundaries in the final microstructure.

Precipitate strengthening is the most effective form of mechanical strengthening in Ni-base superalloys, especially at elevated temperature [8]. While early Ni-base superalloy compositions contained small volume fractions of nanoscale precipitates, the coherently embedded γ' $L1_2$ phase can exist in equilibrium with the gamma matrix at significantly greater volume fraction. These precipitates nucleate and grow as a regular array of coherent particles, as shown in 1.4, and are resistant to shearing by dislocations.

These coherently embedded γ' precipitates are most responsible for the favorable mechanical properties of Ni-base superalloys at elevated temperature.

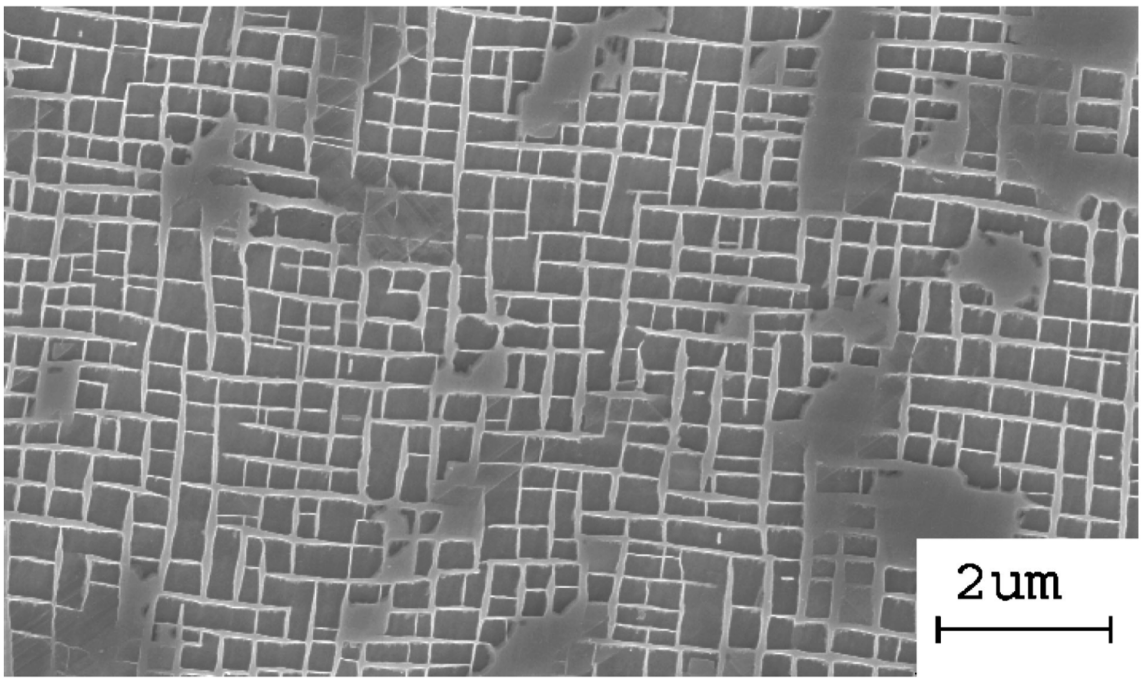

Figure 1.4: Characteristic Ni-base superalloy microstructure, showing a high volume fraction of coherent, embedded γ' precipitates From [9].

1.3 Co-base Superalloys

1.3.1 Chemistry and Microstructure

Cobalt has a both a higher melting point and, in alloyed form, more favorable oxidation properties than nickel [10, 11]. Conventional wrought Co-base superalloys have been used for airfoil and combustor applications in gas turbine engines for several decades. These alloys are typically strengthened by a combination of solid solution elements and carbide precipitates and have superior hot corrosion and fatigue properties in lower-temperature applications [2, 8]. While these carbides impart some strength, it was not until recently that an intermetallic $L1_2$ γ' phase analogous to the Ni-base system was found in a Co-base system. In 2006, researchers discovered the existence of this $L1_2$ intermetallic compound in the Co-Al-W ternary system, enabling a class of Co-base superalloys that can be used in higher-temperature applications than their wrought counterparts [12]. Like Ni-base superalloys, this nominally Co_3(Al,W) $L1_2$ phase exists in equilibrium with a FCC solid solution phase at high temperature. This two-phase field is relatively narrow in the ternary system, as shown in Figure 1.5.

Co has a melting temperature 50 °C higher than that of Ni, and Co-base superalloy compositions have been shown to exhibit melting temperatures 100 °C higher than Ni-base superalloys. Further alloying additions beyond the ternary system do not generally depress the melting temperature. As creep performance is correlated with melting temperature, Co-base superalloys with a γ-γ' microstructure may have the ability to operate at higher temperatures relative to Ni-base superalloys, providing significant fuel savings by improving engine efficiency.

Processing of Co-base superalloys is also analogous to processing in the Ni-base system. Single crystals of Co-base superalloys can also be cast via the Bridgman process. Unlike Ni-base superalloys, freckles and other casting defects are less prevalent in Co-

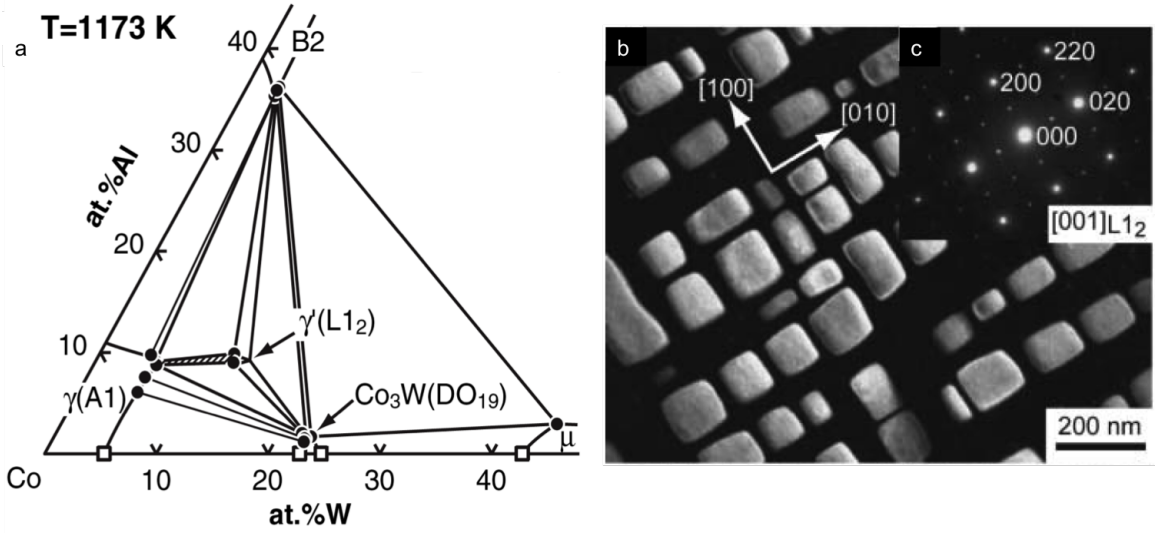

Figure 1.5: Initially proposed ternary phase diagram of the (a) Co-Al-W system. Dark field TEM micrographs are shown in (b) indicating the ordered $L1_2$ γ' phase in equilibrium with the solid solution matrix along with (c) the characteristic $L1_2$ superlattice reflections for b = [001]. Adapted from [12].

base superalloys [13]. This is a result of favorable partitioning between the liquid and solid during casting arising from the inclusion of relatively more dense alloying elements than are present in Ni-base compositions. W and Ta preferentially partition to the liquid during solidification and prevent the density inversions that induce convective instabilities in the melt. Thus, dendrite breakage and fragmentation is mitigated, allowing for large components to be cast with relatively few defects, which is particularly important in physically large components such as land-based turbine engines. [13].

After casting and an annealing and precipitation heat treatment, the final microstructure of Co-base superalloys in the Co-Al-W ternary system is remarkably similar to the Ni-base superalloys. The morphology of the $L1_2$ γ' precipitates is determined by the degree of lattice parameter misfit, δ, between the matrix and precipitate phases [14]. This

misfit value is typically taken as:

$$\delta = \frac{a_{\gamma'} - a_{\gamma}}{1/2(a_{\gamma'} - a_{\gamma})} \tag{1.1}$$

In this equation, a represents the lattice parameter of the two separate phases. For Ni-base superalloys, the lattice parameter of the disordered γ matrix phases is almost always slightly larger than that of the precipitate γ' phase, resulting in a negative lattice misfit values between -0.2% and -0.4% [14]. However, Co-base superalloys typically have larger lattice parameters in the precipitate phase, resulting in positive misfit values of approximately the same magnitude [12]. While these lattice misfit values do not prevent the two phases from maintaining coherency, they do induce significant stresses in both phases. In both cobalt and nickel, there is significant elastic anisotropy in the ordered precipitates, with relatively weaker face centers than face corners. This anisotropy accounts for the cuboidal shape of the precipitate phase [15].

1.3.2 γ' Stability

Although the microstructure of coherently embedded, ordered precipitates in a solid solution matrix is identical between Ni- and Co-base alloys, there are significant distinctions between the behavior of the two systems at turbine operating temperature. While Co-base superalloys typically possess higher melting temperatures than their Ni-base counterparts, the γ' phase has a generally lower solvus temperature in the Co-base case, as shown in Figure 1.6. Finding means of increasing the $L1_2$ γ' solvus temperature while maintaining a two-phase γ- γ' microstructure is therefore a major concern.

Following the 2006 discovery of the experimental $L1_2$ phase, a great deal of initial work was concerned with assessing its stability in the baseline ternary Co-Al-W system. Assessing $L1_2$ stability within the ternary is complicated by the fact that it does not

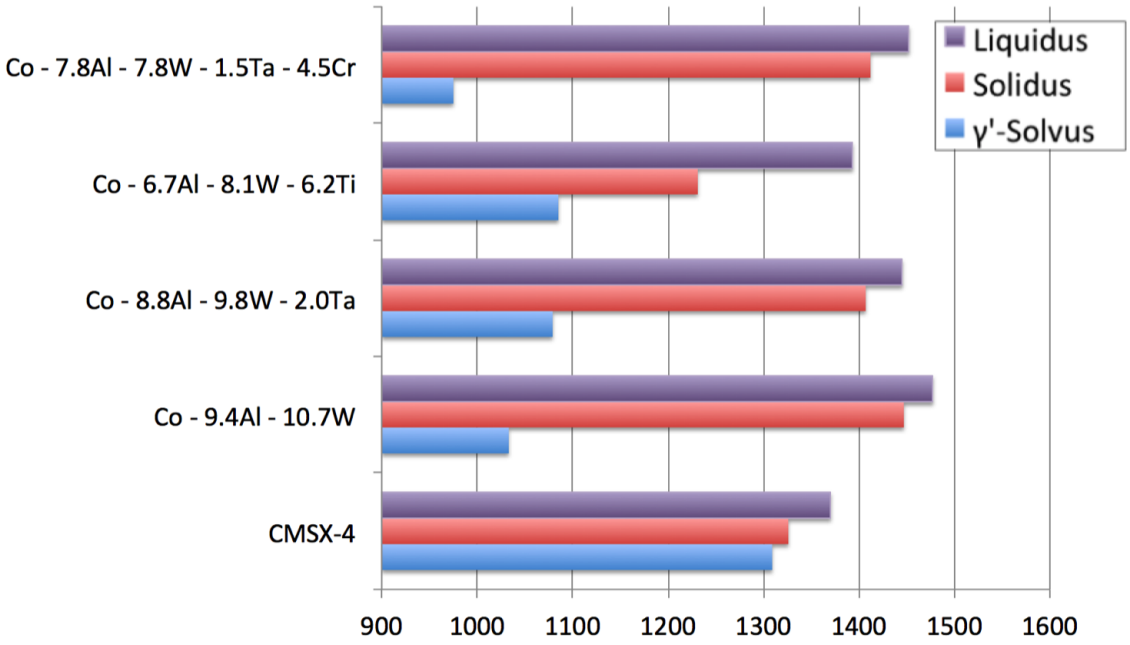

Figure 1.6: Transition temperatures of four different Co-base superalloys relative to the second generation Ni-base superalloy CMSX-4. Higher order alloying additions beyond the ternary Co-Al-W can increase the γ' solvus [16].

appear on the solidus surfaces and is therefore not a phase that appears immediately on solidification [17]. As is apparent in Figure 1.5, the range of compositions over which $L1_2$ is stable at 900 °C is quite narrow, and the phase is thermodynamically competitive with a three-phase mixture of elemental Co, B2 CoAl, and $D0_{19}$ Co_3W. Experimental test ribbons annealed for up to 8000 hours at 900 °C at a number of compositions around the $L1_2$ phase field reported by Sato seem to indicate that $L1_2$ is metastable at very long annealing times, as final annealed microstructures contain a four-phase mixture at apparent equilibrium. While this would seem to be in violation of the Gibbs phase rule for a ternary system, it is possible that coherency strain between the γ and γ' phases serves to confer an extra degree of freedom on the system [18, 19]. Notably, further studies conducted at 950 °C for long annealing times did not demonstrate the same phase transformation, and $L1_2$ precipitate phase fractions were maintained [20].

Other researchers have demonstrated that, for single crystal compositions, the ternary

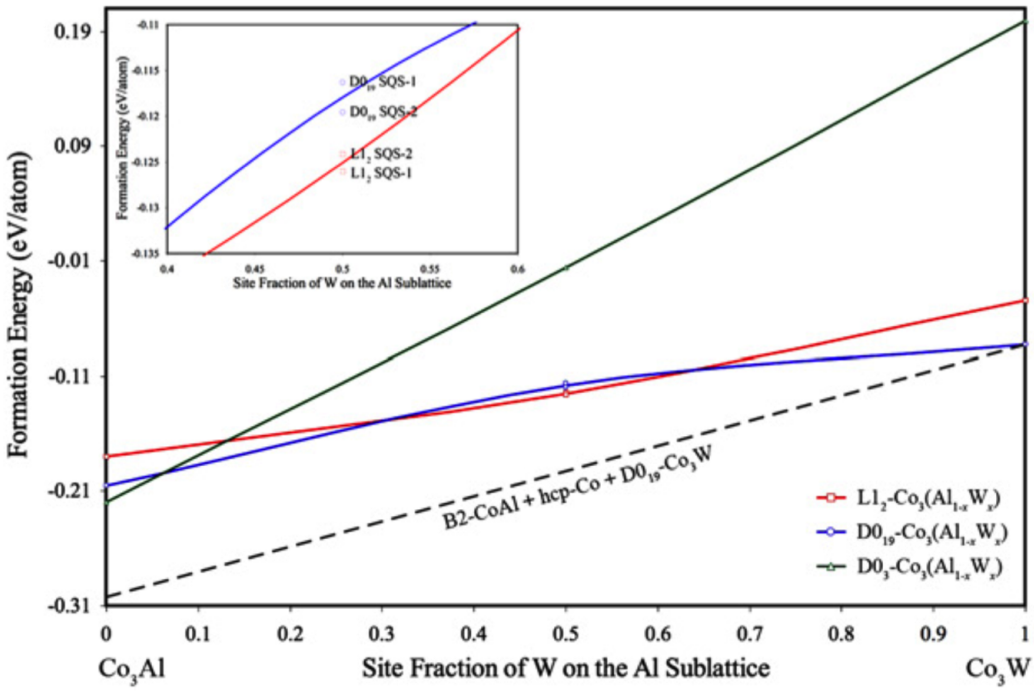

Figure 1.7: Formation energies of special quasi-random $L1_2$ $Co_3Al_{1-x}W_x$ structures calculated via DFT. These formation energies are plotted in red and compared to the formation energy of the three-phase mixture, denoted by the dashed line.

γ-γ' microstructure remains stable even at extended annealing times and under creep conditions [21]. This suggests that the presence of grain boundaries plays an important role in the development of deleterious phases under extreme annealing conditions. It is likely that tungsten diffusion accounts for the sluggish kinetics of transformation in compositions where B2 CoAl or $D0_{19}$ Co_3W develop. It may also be the case that these phases nucleate more easily at grain boundaries. However, this alone does not explain the presence of four phases in a ternary system.

As the initial experimental evidence of $L1_2$ γ' precipitate stability was inconclusive, a number of studies were performed on assessing the thermodynamics in the Co-Al-W system using calculations and first-principles methods. The first of these was reported by Jiang using $L1_2$ special quasi-random structures (SQS) and density functional

theory (DFT) to model the stability of γ' at 0 K. The formation energies of several experimentally-observed compounds in the Co-rich part of the Co-Al-W were calculated. Two $L1_2$ γ' SQS cells were constructed with equimolar mixing of Al and W on the $L1_2$ B sublattice and their formation energies also were calculated using DFT. As is clear in Figure 1.7, these $L1_2$ structures are unstable relative to a three phase mixture of elemental Co, B2 CoAl, and $D0_{19}$ Co_3W. As this preliminary study was confined to a few compositions and limited to 0 K, it does not demonstrate conclusive proof of the instability or metastability of $L1_2$ compounds in the Co-Al-W ternary system. Rather, it suggests that other finite temperature effects play an important role in stabilizing the $L1_2$ phase relative to these other compounds.

Having a working understanding of the underlying thermodynamics and phase equilibria in the Co-Al-W system is essential if this class of alloys is to be used in turbine applications. Traditionally, this information is compiled in Computer Coupling of Phase Diagrams and Thermochemistry (CALPHAD) databases which take as input free energy polynomial functions that are fit to experimental data. While this method is quite robust in regions where there is a good deal of experimental data, it becomes less accurate in compositional domains in which the underlying polynomial functions have to extrapolate in order to reach. Initial CALPHAD constructions done by several independent groups were fit to experimental data in which the γ' phase was stable [22, 23, 24]. In these models, literature values were used as input for the underlying unary and binary systems in order to construct a full ternary description. As a result, the quality of these models is determined by the quality of the underlying experimental data and they have a limited ability to accurately extrapolate beyond the region used for fitting.

A thermodynamic description of the complete Al-Co-W was recently revised using the CALPHAD method, treating the $L1_2$ precipitate phase as metastable over the entire compositional and temperature range. While this model takes in some DFT data for

fitting, it is mostly built around experimentally observed phase fractions. As seen in Figure 1.8, the aggregated 0 K DFT data across the 75 at % Co pseudobinary line shows no compositional region over which the $L1_2$ phase is stable. Notably, the authors of this study found it necessary to include vacancy terms in the underlying Redlich-Kistler polynomials in order to account for the presence of a disordered B2 CoAl phase with appreciable solid solubility. All interaction terms between the three constituent species and these vacancies were assigned large positive values [25].

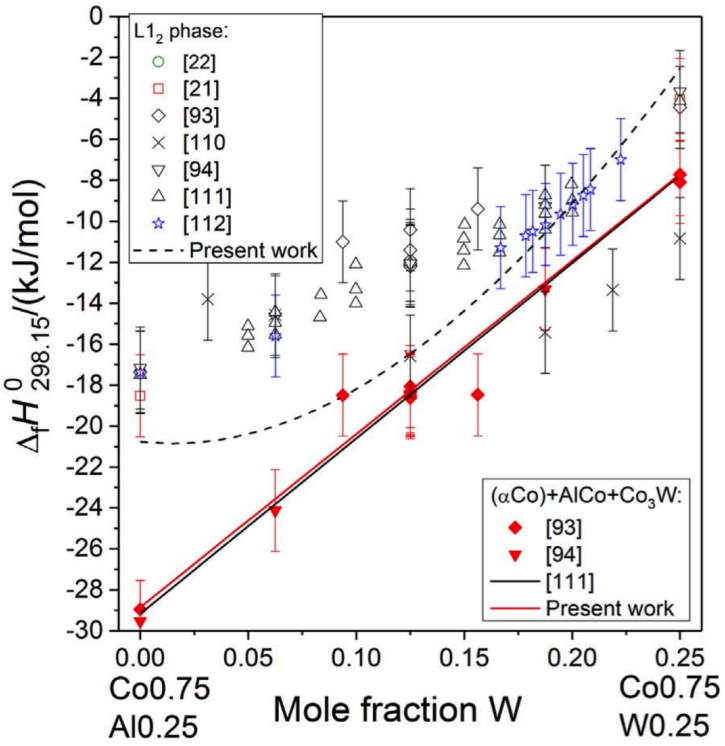

Figure 1.8: Formation energies of several $L1_2$ Co_3(Al,W) structures calculated via DFT compiled from the existing literature. The $L1_2$ formation energies are assessed relative to a three-phase ground state mixture in red and black. From [25].

While the CALPHAD models do an excellent job of defining the phase boundaries of the stable phases, there is difficulty in assessing regions where a phase exhibits metastability and instability. Also, due to the large number of significant finite temperature effects in the Co-Al-W system, it is particularly difficult to assign polynomial values in

this instance. First-principles based methods are excellent means of quickly assessing 0 K formation energies of a given compound, but are unable to assess finite temperature free energy information in isolation. Until recent advances in computing power, it was difficult to accurately gather sufficient compositional data to build a complete description of the thermodynamics of a ternary system. Today, we can rapidly gather thousands of unique formation energies for compounds across compositional space.

Using the cluster expansion method, we are able to build thermodynamic descriptions for individual phases as a function of composition and configuration at 0 K. This 0 K description can be linked to finite temperature entropy effects using statistical mechanics. Recent code developed by the Van der Ven group [26, 27, 28] has been shown to model finite temperature thermodynamics, kinetics, and phase stability in several systems, including lithium batteries, magnesium alloys, and nickel superalloys using this cluster expansion formalism. A major aspect of the research reported here is extending this formalism to investigate stability in the Co-Al-W ternary baseline system, as well as higher-order systems.

1.4 Mechanical Behavior in Superalloys

The stability of the two-phase γ-γ' microstructure is important from a mechanical, as well as thermal, standpoint. Without the ability to resist shear at elevated temperatures, the precipitate phase is unable to impart adequate strength to the overall component. A complete understanding of the varying ways in which the precipitate phase undergoes mechanical deformation is therefore a requirement. Co-base superalloys plastically deform in similar, but distinct ways from their Ni-base counterparts, much of which can be traced back to alloy chemistry. As with assessing thermodynamics, first-principles methods can once again be employed to quickly determine the energetics of deformation.

1.4.1 Heterogeneous Deformation

Plastic deformation in metals is accomplished primarily by dislocation motion. Superalloys gain their strength by impeding the motion of these dislocations in a variety of ways. Considering that land-based turbine blades spend the majority of their lifetime under extreme thermal and mechanical conditions, resistance to plastic deformation via creep is typically the primary design consideration for superalloys. The creep deformation mechanisms differ considerably in the two phases.

During the initial phase of primary creep, plastic deformation is mainly accommodated via the motion of dislocations through the narrow γ matrix channels in between the γ' precipitate phase. As the γ phase is a disordered FCC solid solution, the dislocations are of the $\frac{a}{2}[110]$ type and glide on (111) planes through these channels. The γ phase heterogeneously accommodates the majority of this initial plastic deformation largely due to the misfit between the two phases, as the effective shear stress on a dislocation will be relatively larger in the horizontal or vertical γ channels, depending on the sign of the misfit, δ [2].

For nickel superalloys, which typically have a negative misfit, applying a tensile load along the [001] crystallographic direction largely relieves the misfit stresses in the vertical γ matrix channels. The opposite is true in the horizontal channels, as any tensile applied load will exacerbate the existing misfit stresses and cause dislocations in those channels to experience a greater resolved shear stress. In order to become mobile in the matrix channels, these dislocations must experience a greater resolved shear stress than the Orowan bowing stress, τ:

$$\tau = \frac{\mu b}{l} \tag{1.2}$$

In this equation, μ is the critical resolved shear stress of the material, b is the Burgers

vector of the dislocation, and l is the width of the γ matrix channels projected onto the relevant (111) slip plane. In this fashion, several dislocations can migrate through matrix channels and pile up at the γ-γ' interface. Before any shear occurs within the γ' precipitate phase, the misfit stress that exists at the interface can be mitigated as the dislocation deposits a leading screw dislocation segment in the phase with the smaller lattice parameter. This and other climb phenomena locally relieve the misfit stress at the interface. As several dislocations glide through the γ matrix channels and build up at the interface during creep deformation, they interact with each other and form regular dislocation networks. These networks further reduce the misfit stress between the two phases and prevent long-range dislocation motion. Figure 1.9 shows these dislocation networks in two Ni-base superalloys.

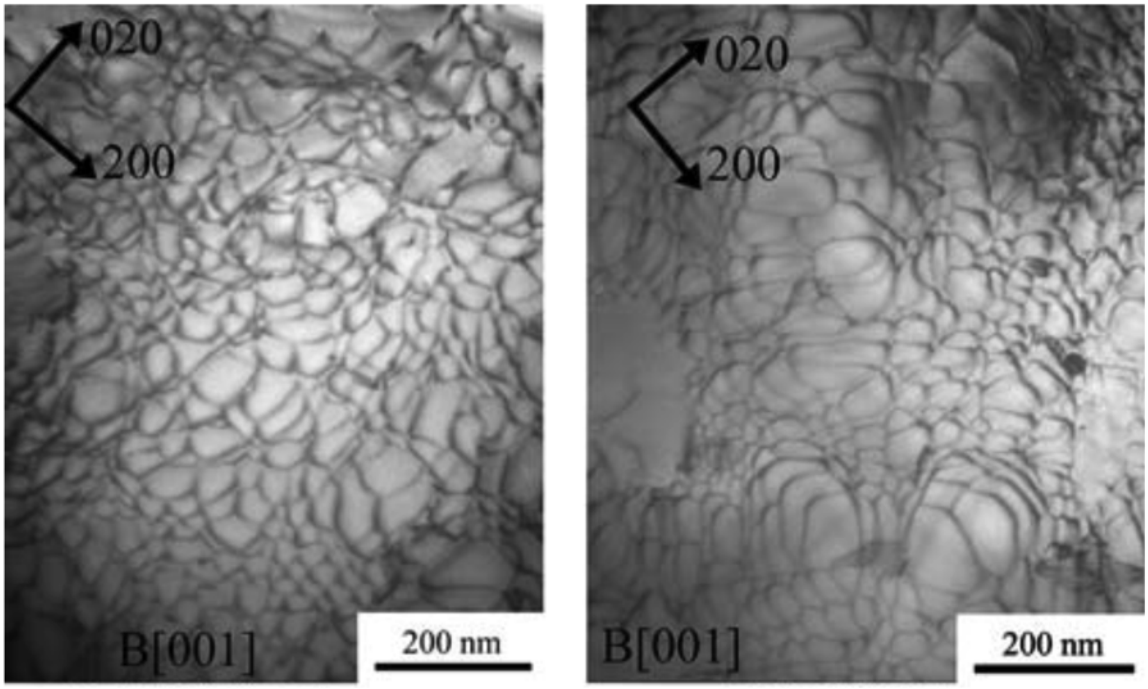

Figure 1.9: Regular networks of dislocations in two Ni-base superalloys shown in bright-field TEM at 0.5% and 1.0% creep strain, respectively. From [29].

After these networks form, additional deformation is typically accommodated by the

precipitate rafting phenomenon. Rafting is the process by which precipitates elongate and merge together along certain crystallographic planes, as seen in Figure 1.10. As this is a diffusive process, it is prevalent only at elevated temperature and after the easier glide-accommodated deformation has occurred. The direction of coarsening is determined by the direction of the applied load, σ, and the misfit strain, δ. In nickel-base superalloys, which typically have negative misfit strains, the precipitates coarsen perpendicular to the applied load whereas in cobalt-base, which typically have positive misfit strains, the direction of coarsening is parallel to the applied load. This phenomenon can be so strong that the microstructure can effectively invert, where now the $L1_2$ γ' phase serves as the matrix with embedded γ precipitates. When this occurs, further deformation can be accomodated by shearing in the $L1_2$ phase [30].

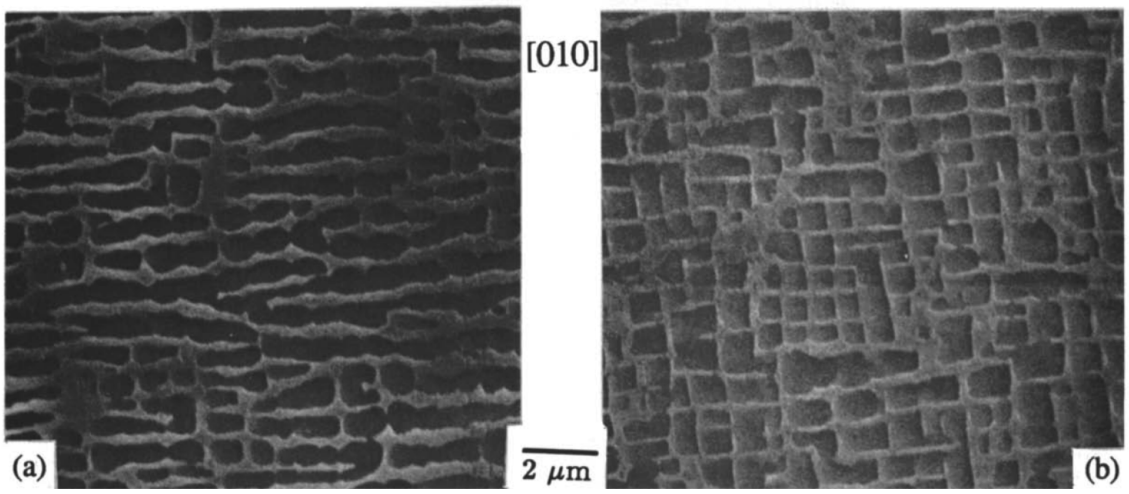

Figure 1.10: Post-crept inhomogeneous microstructure of Ni-base superalloy a) Rafting has occurred in direction perpendicular to loading axis b) No rafting occurs in direction parallel to loading axis. From [29].

1.4.2 $L1_2$ faulting

Superalloys generally owe a great deal of their resistance to deformation by the resistance of the $L1_2$ γ' precipitate phase to shearing events. During the initial phases of

primary creep, deformation in the γ' phase can be accommodated by the slip of $\langle 112 \rangle$ $\{111\}$ type dislocations. This shearing is accompanied by the formation of a stacking fault (SF) of either the superlattice instrinsic (SISF) or superlattice extrinsic (SESF) type [30]. Early TEM revealed that the majority of deformation during this mode occurs on $\{111\}$ type planes [31].

A complete a$\langle 112 \rangle$-type dislocation can dissociate in a couple different ways that satisfy Frank's rule. One dissociation reaction results in the formation of an antiphase boundary (APB) while the other results in the formation of both an SISF and SESF. If an APB is formed, the resultant partial dislocations are still relatively long, and the diffuse dislocation cores are of too high an energy to make this the dominant faulting type. The relatively more compact partial dislocations that accompany SISF and SESF formation mean that these are the dominant faulting mechanisms observed in the $L1_2$ γ' precipitate phase in Ni-base superalloys. These faults are analogous to the stacking faults observed in purely FCC materials.

The formation of SISFs in Ni-base superalloys is likely due to the interactions of two $\langle 110 \rangle$-type dislocations interacting at the γ-γ' interface:

$$\frac{a}{2}\langle 011 \rangle + \frac{a}{2}\langle 101 \rangle \rightarrow \frac{a}{2}\langle 112 \rangle \rightarrow \frac{a}{3}\langle 112 \rangle + SISF + \frac{a}{6}\langle 112 \rangle \tag{1.3}$$

In this reaction, two $\langle 110 \rangle$-type dislocations interact at the γ-γ' interface and a leading $\frac{a}{3}\langle 112 \rangle$ partial dislocation shears across the γ' precipitate, leaving behind a faulted SISF region. The trailing $\frac{a}{6}\langle 112 \rangle$ is effectively pinned at the interface, as its shearing across the precipitate would result in the formation of a high-energy APB. This is not experimentally-observed in either Ni-based or Co-based superalloys. SESF formation is possible if another set of $\langle 110 \rangle$-type dislocations interact at the interface and another leading partial shears across the existing SISF. A schematic illustrating these faults on

the (111) plane is shown in Figure 1.11.

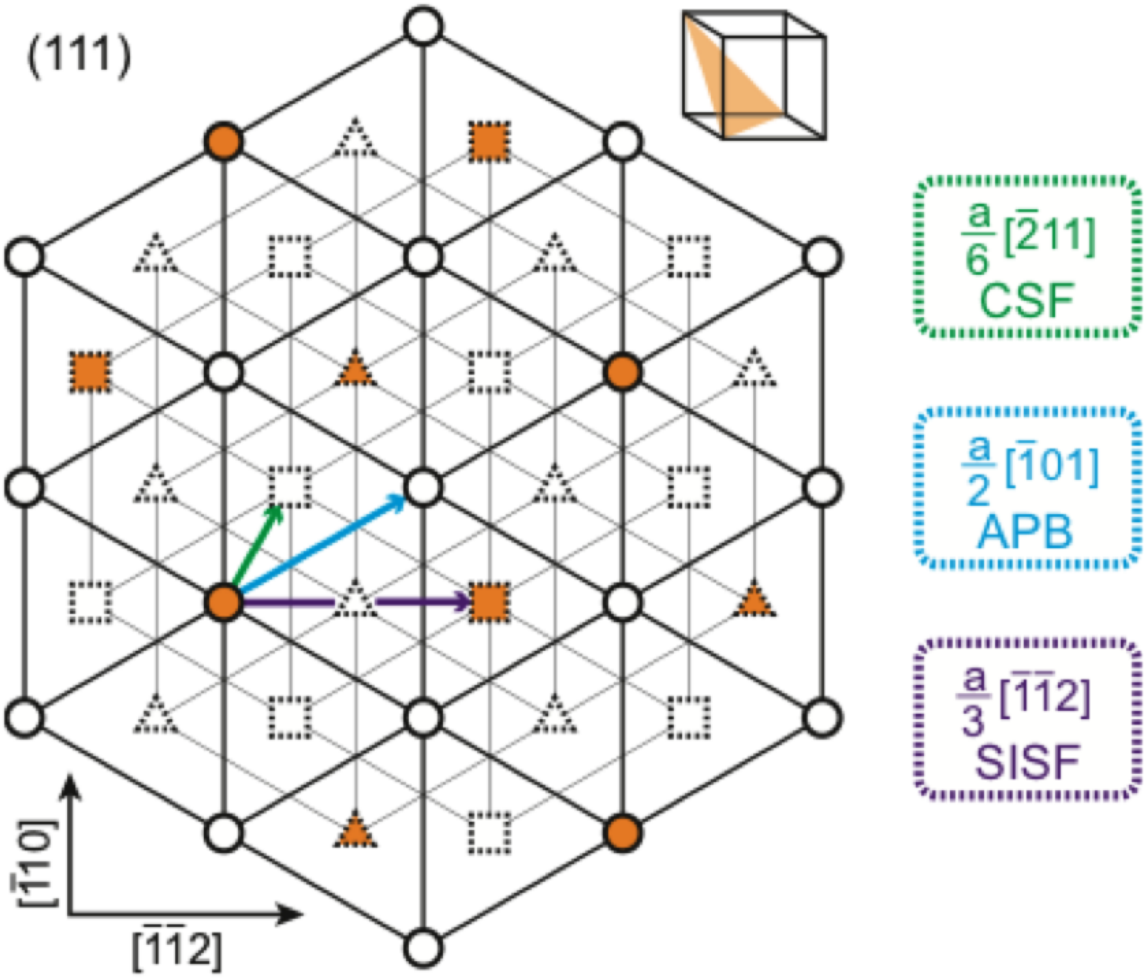

Figure 1.11: A schematic representation of (111) layers in the $L1_2$ structure showing the partial dislocations associated with each kind of possible fault. Different shapes represent distinct (111) layers in the ABC stacking sequence. Open shapes correspond to the majority A sublattice (Ni/Co) while closed shapes correspond to the B sublattice (Al/W). Adapted and reproduced from [32].

While the above dissociation reaction is the most commonly accepted explanation of SISF-producing shearing events within the $L1_2$ γ' precipitate phase, it is not the only one. Other reactions exist which do not violate Frank's rule and produce SISFs. While these events may not be completely understood, what is clear is that the types of dislocations

present in the γ channels and at the interface play a critical role in determining the type of faulting that will be observed within the precipitate phase. As such, knowledge of the energetics of the various faults can be used to tailor superalloy chemistries that are more resistant to faulting.

1.4.3 $L1_2$ deformation via shearing and APB formation

Glide events can also occur in the $L1_2$ phase, especially after the microstructure has inverted. Two possible dissociation events are possible with the a$\langle 110 \rangle$ Burgers vector [33]:

$$a\langle 110\rangle\{\bar{1}11\} \rightarrow \frac{a}{3}\langle 211\rangle\{\bar{1}11\} + SISF + \frac{a}{3}\langle 12\bar{1}\rangle\{\bar{1}11\} \tag{1.4}$$

$$a\langle 110\rangle\{\bar{1}11\} \rightarrow \frac{a}{2}\langle 110\rangle\{\bar{1}11\} + APB + \frac{a}{2}\langle 110\rangle\{\bar{1}11\} \tag{1.5}$$

The first of these equations results in the formation of an SISF bounded by two $\frac{a}{3}$ dislocation dipoles. This SISF is directly comparable to the existence of intrinsic stacking faults in the disordered matrix phase, with a locally missing (111) plane that breaks the ABC stacking sequence such that it is locally ABA. In this way, the formation of an SISF can be thought of as transitioning from a fully FCC stacking sequence to an arrangement with local HCP stacking around the fault.

The second of the above equations involves the shearing of the $L1_2$ γ' phase by an $\frac{a}{2}$ $\langle 110 \rangle$ type dislocation and the formation of an APB defect. In this kind of defect, the local stacking sequence remains unchanged but local chemistry is altered as nearest-neighbor bonds are violated. In Ni-base superalloys, the formation of this APB is generally energetically unfavorable, leading to partial dislocation spacings that are relatively small.

Additional deformation can be accommodated by a thermally-activated climb process of the $\frac{a}{2}\langle 110\rangle$ superpartial dislocations onto {100} planes. The energy in the $L1_2$ phase required to form an APB is generally lower on the {100} planes than it is on the {111} type, which is the energetic driving force for this thermally-activated climb. As there is typically a high complex stacking fault (CSF) energy between the Shockley partials from the $\frac{a}{2}\langle 110\rangle$ dissociation, the superpartials dissociate on {111} planes, locking the dislocation configuration and preventing further deformation. This is known as a Kear-Wilsdorf lock, as shown in Figure 1.12. As this process is thermally-activated, it is present only at higher temperatures and is responsible for the anomalous increase in strength in the $L1_2$ phase.

As the lock forms on the (100) type plane, an extended APB forms between the two dissociated superpartials. As the energy of the (100) APB is less than that of the original (111) APB, there is no driving force for cross-slip back onto the (111) plane. [34]

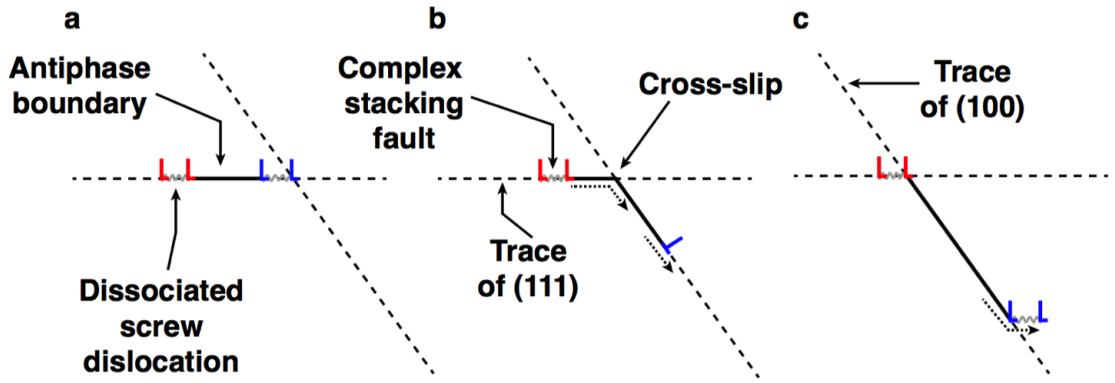

Figure 1.12: Kear-Wilsdorf lock process schematic. a) Glide along (111) plane, b) leading screw dislocation cross-slipping onto (100) plane, c) Kear-Wilsdorf lock with small CSF extending back onto (111) planes. Adapted from [34].

Chapter 2

Methodology

2.1 First principles methods

First principles modeling was used in several instances in this work. The formation energies of several distinct configurations of atoms in various crystal structures were assessed using density functional theory (DFT). DFT is a method of investigating the electronic structure of condensed phases, and is particularly well-suited for modeling the behavior of metallic elements. Until recently, it has been relatively difficult to gather the amount of foundational 0 K calculations necessary to explore the phase stability of multi-component systems. Recent advances in computing speed have made it relatively easier to rapidly acquire this information, allowing for the exploration of systems containing hundreds or thousands of configurations as in this work (Figure 2.1).

The Vienna Ab-initio Simulation Package (VASP) was the program used to calculate the formation energies of several hundred unique FCC, BCC, and HCP orderings on the given lattice [35, 36, 37]. The projector augmented wave method was used and all potentials used the spin-polarized generalized gradient approximation (GGA) [36, 38, 39]. An energy cutoff of 500 eV and a Γ-centered k-point mesh were used. k-point

convergence tests were run on initial parent cell primitive structures to within an error of 0.5 meV/atom and the k-point mesh grids of subsequently generated larger supercells were scaled to this result. All calculations performed used the projector augmented wave (PAW) pseudopotential as this has been demonstrated to have high accuracy in calculating solid cohesive energies [40].

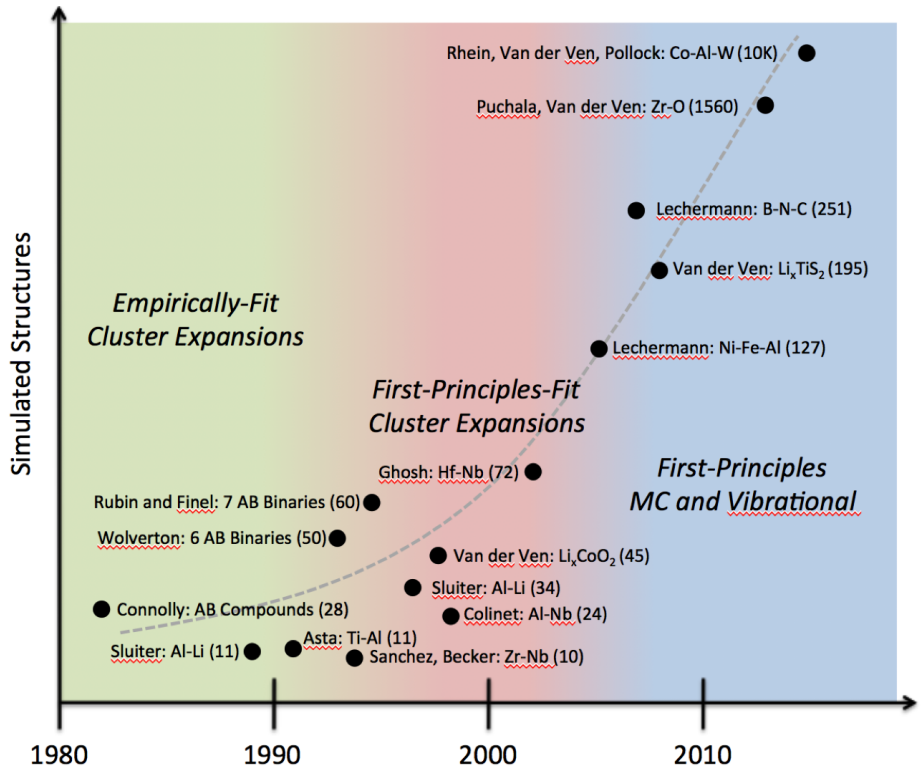

Figure 2.1: Number of structures in example systems explored via DFT over time.

2.1.1 Cluster Expansion Formalism

Phase stability in the Co-Al-W system was studied via the cluster expansion method. A given ordering on an n-atom lattice can be expressed as a vector of occupation site variables $\vec{\sigma} = \{\sigma_1, \sigma_2, \sigma_3, ..., \sigma_n\}$. For the Co-Al-W crystal structures considered, this occupation variable is assigned a value of -1,0, or 1 depending on the species occupying

a given lattice site. Formation energies at 0 K, E_f, can be obtained for each ordering relative to the pure elements in their respective ground states, according to:

$$E_f(\vec{\sigma}) = E(\vec{\sigma}) - X_{Co}E_{Co} - X_{Al}E_{Al} - X_W E_W \tag{2.1}$$

in which $E(\vec{\sigma})$ is the total energy per atom of a given ordering obtained via DFT and X_i and E_i are the atomic fraction and elemental formation energy of a given species. The baseline reference ground states of elemental Co, Al, and W at 0 K are HCP, FCC, and BCC, respectively.

To obtain finite temperature free energies and determine phase stability, a configurational cluster expansion formalism was used [41, 42, 43]. In this approach, a set of DFT formation energies is used to build a generalized expression for the formation energy of any ordering of atoms, $\vec{\sigma}$, on a given crystal structure:

$$E_f(\vec{\sigma}) = V_0 + \sum_{\alpha} V_\alpha \phi_\alpha(\vec{\sigma}) \tag{2.2}$$

where $\phi_\alpha(\vec{\sigma})$ is a cluster function corresponding to the product of the occupation variables of the sites in cluster α:

$$\phi_\alpha(\vec{\sigma}) = \prod_{i \in \alpha} \sigma_i \tag{2.3}$$

The V_α expansion coefficients are termed the effective cluster interactions (ECI) and the cluster expansion is summed over all clusters of sites α.

While the sum in the above expression for formation energy extends over all sites α within a crystal structure, the terms need to be truncated at a certain cutoff. In practice, relatively few non-zero ECIs need to be included in a cluster expansion in order to rapidly and accurately predict the formation energy of a given configuration on the lattice.

2.1.2 Configurational Free Energy Effects

The CASM package [44, 45, 46, 47] was used to enumerate the symmetrically distinct supercells for each crystal structure, fit the ECIs of the cluster expansion, and perform Monte Carlo simulations to determine finite temperature energies. Cluster expansions were performed separately for the FCC, BCC, and HCP crystal structures and ECIs were parameterized using a genetic algorithm [48] and deep first search method [45]. Formation energies were weighted by their distance from the metastable convex hull in order to increase the accuracy of the cluster expansion.

Monte Carlo simulations were used in order to capture the effects of configurational free energy on the system. For these calculations, the grand canonical ensemble was used, in which chemical potential and temperature are the thermodynamic variables. In each Monte Carlo simulation, a large supercell was generated and allowed to equilibrate under a given set of chemical potential and temperature conditions. Initially, temperature was held constant at a sufficiently high temperature such that the underlying structure would equilibrate as completely disordered. Chemical potential space was then discretized to get a set of initial compositions and characteristic potentials. Subsequent cooling and heating runs could then be discretely integrated using the trapezoid rule to obtain an expression for the configurational free energy term:

$$G(x,T) = G_0 + \sum_i \widetilde{\mu}_i (x_i - x_{i-1}) \tag{2.4}$$

2.1.3 Vibrational Free Energy Effects

Vibrational free energy contributions were calculated using the quasiharmonic approximation for selected ordered structures. Large supercells were constructed for the selected structures and force constants were extracted from VASP DFT calculations in

which isolated atoms were perturbed relative to their equilibrium position using the frozen phonon approach [49, 50]. At temperatures above the Debye transition, the harmonic approximation for vibrational energy is given by:

$$F_{vib}(T) = k_B T \sum_m ln(\frac{hv_m}{k_B T}) \tag{2.5}$$

where v_m are the frequencies of the normal modes of oscillation. Large supercells were constructed from baseline primitive cells and the CASM vibrational package was used to identify symmetric operations within the given crystal structure. A minimum number of critical perturbations were identified to capture the entire phonon spectrum. Identified atoms were perturbed 0.03 Å from their equilibrium position. These perturbed supercells were allowed to run in VASP as before, but were run statically so as not to allow the structure to relax back to its equilibrium position.

Force constants were obtained with a least-squares fit and the eigenvalues used to construct the dynamical matrix from which phonon dispersion curves were calculated [51]. Several volumes were allowed to vary ±5% within the quasiharmonic approximation in order to capture the effects of thermal expansion. Helmholtz free energy surfaces as a function of temperature and volume were subsequently generated. The minimum energy path as a function of temperature across this surface is the vibrational free energy term, which can be summed linearly with the 0 K formation energies to yield an expression for an overall finite temperature free energy term.

2.1.4 The 75 at% Co pseudobinary

Initially, this cluster expansion study focused solely on the 75 at% Co pseudobinary line that past work done by other researchers had considered at 0 K, as shown in Figure 2.1. The formation energies of 63 distinct orderings on the $L1_2$ crystal structure were

calculated via DFT. In addition to this, the formation energies of several line compounds from the experimental Co-Al-W phase diagram were calculated. In this pseudobinary study, the $L1_2$ structures were the only ternary compositions considered. No solid solubility on the A sublattice was considered, as Al/W occupancy on the B sublattice was the only site that was allowed to vary.

All formation energies calculated via DFT were referenced to the ground state energies of the pure elements in their crystallographic ground state, such that:

$$G_0(x) = E_0 - \sum_i x_i g_0 \tag{2.6}$$

Where E_0 is the unreferenced energy per atom calculated via DFT and x_i and g_0 are the concentration and reference energy of the pure elements, respectively. In the case of Co-Al-W, the ground states are HCP Co, FCC Al, and BCC W.

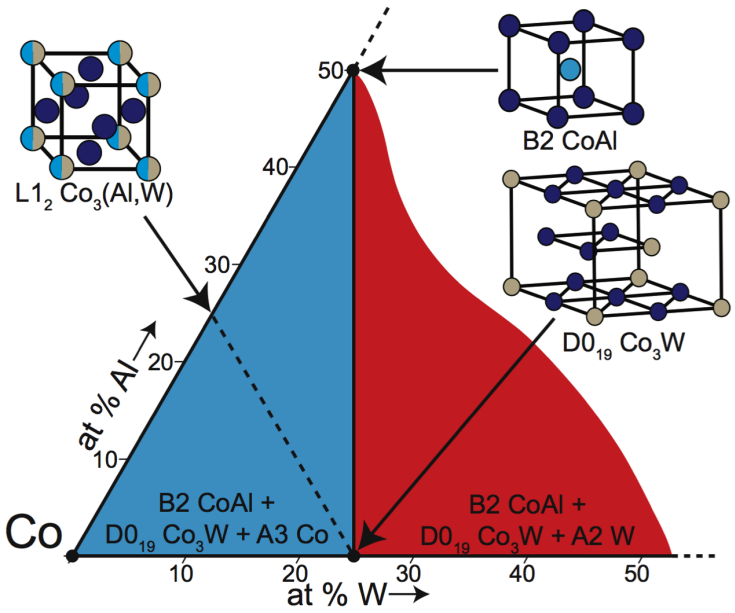

Figure 2.2: 75 at% Co psuedobinary line examined via DFT and binary cluster expansion. Colored regions correspond to 0 K ground state three-phase regions.

2.1.5 Ternary Cluster Expansion

After the pseudobinary cluster expansion was completed, a full ternary cluster expansion was completed for the FCC, BCC, and HCP crystal structures in the Co-Al-W system. One major complication of doing a full ternary, or higher-order, cluster expansion is the sheer number of formation energies that must be calculated via DFT in order to get an accurate fit:

Table 2.1: Number of unique supercells corresponding to the pseudobinary and full ternary cluster expansions.

Supercell Size	Binary	Ternary
1	-	3
2	-	6
3	-	21
4	2	96
5	-	165
6	-	790
7	-	1245
8	3	7482
12	6	747150
16	24	$\approx 10^7$

Because of the computationally-prohibitive number of distinct orderings in higher-order systems, a cutoff limit must be placed. For the ternary cluster expansion in this work, formation energies of supercells containing eight or fewer atoms were calculated. While this is useful in order to obtain an overall baseline, it does not adequately capture regions of fine compositional detail. In order to capture this, a number of large supercells around particular compositional areas of interest were also calculated. Specifically, these include the regions around pure elemental Co, B2 CoAl, and the experimentally-observed $L1_2$ phase.

Nearly every phase in the Co-Al-W ternary system can be described as an ordering on an FCC, BCC, or HCP lattice, with the exception of some quasicrystal structures

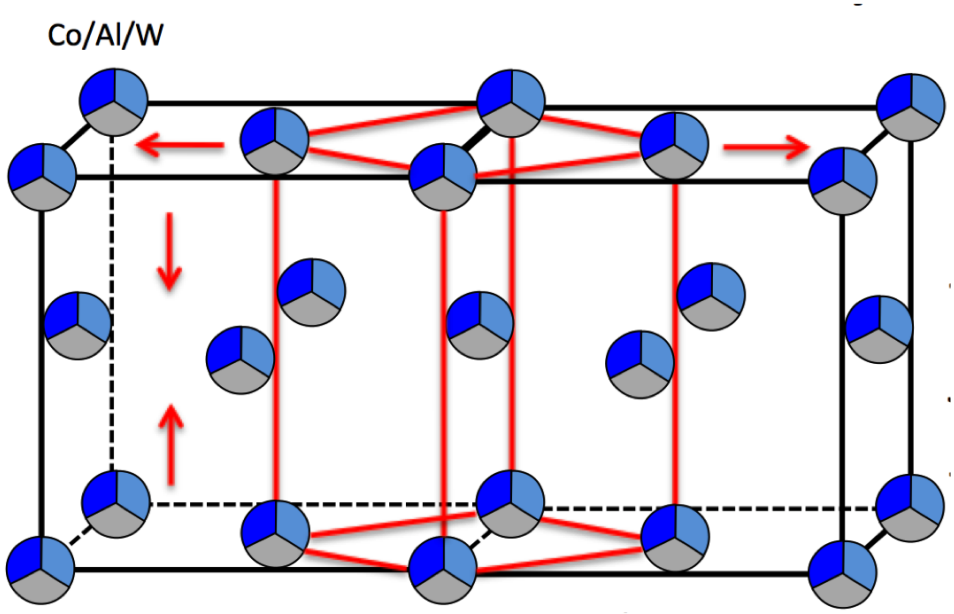

Figure 2.3: Schematic illustration the Bain strain pathway available to FCC Co-Al-W to transform into BCC

on the Al-rich end of the Co-Al binary. Many of these orderings break the original cubic symmetry of the parent crystal structure. For instance, while a pure FCC crystal lattice has 12 nearest neighbors, upon relaxation via DFT that may no longer be the case. Typically, this effect is small and the number of nearest neighbors retained upon relaxation is relatively close to the original structure. However, certain orderings of FCC, BCC, and HCP are dynamically unstable and undergo considerable deformation during DFT relaxation to the point where they more closely resemble an ordering on a different parent crystal structure.

We ultimately do not want to include these structures that relax away from their original parent crystal in the overall cluster expansion of the original lattice. Strain can be used as an order parameter to identify specific orderings that relax to a different structure. One such strain tensor is the Hencky strain, defined in terms of the stretch

tensor, $\mathbf{U}$:

$$\mathbf{E} = \mathbf{ln}\mathbf{U} \tag{2.7}$$

$$\mathbf{E} = \begin{bmatrix} \epsilon_{xx} & \epsilon_{xy} & \epsilon_{xz} \\ \epsilon_{xy} & \epsilon_{yy} & \epsilon_{yz} \\ \epsilon_{xz} & \epsilon_{yz} & \epsilon_{zz} \end{bmatrix} = \mathbf{E^T} \tag{2.8}$$

This strain tensor has six independent components, and it is convenient to cast these components into a set of symmetry adapted strain metrics, defined as linear combinations of the Hencky strain components:

$$e_1 = \frac{\epsilon_{xx} + \epsilon_{yy} + \epsilon_{zz}}{\sqrt{3}} \tag{2.9}$$

$$e_2 = \frac{\epsilon_{xx} - \epsilon_{yy}}{\sqrt{2}} \tag{2.10}$$

$$e_3 = \frac{2\epsilon_{zz} - \epsilon_{yy} - \epsilon_{xx}}{\sqrt{6}} \tag{2.11}$$

$$e_4 = \sqrt{2}\epsilon_{yz} \tag{2.12}$$

$$e_5 = \sqrt{2}\epsilon_{xz} \tag{2.13}$$

$$e_6 = \sqrt{2}\epsilon_{xy} \tag{2.14}$$

The components of the Hencky strains decouple any volume dependence in the terms e_2 to e_6. All of the volume dilation is captured in the e_1 term, while the e_2 and e_2 describe tetragonal and orthorhombic distortions of the original crystal. The other components represent shear terms.

A common transition pathway in FCC and BCC crystals is the Bain path, as shown in Figure 2.3. The symmetry adapted strain metric components above enable us to represent all symmetrically equivalent FCC-to-BCC transitions in a two-dimensional space spanned by the e_2 and e_3 components. If we consider a conventional FCC unit cell with cubic axes aligned along the Cartesian x-y-z directions, it can be transformed to BCC by a contraction in the z-axis accompanied by simultaneous expansion in the x and y directions. There are three equivalent pathways for this kind of transition, corresponding to contraction along the three Cartesian axes. By casting the final parameters of our relaxed DFT supercells in terms of the e_2 and e_3 components, we are easily able to bin supercells into the structure they most closely resemble. Several structures, particularly along the Co-Al binary, are susceptible to this kind of transition and so were appropriately filtered before any cluster expansion was fit.

2.1.6 Fault Energies

Several first principles methods were used in order to capture the effects of composition and ordering on the experimentally observed faulting behavior in the $L1_2$ phase. At the most basic level, the formation of an SISF can be visualized as a transition from a locally $L1_2$ stacking sequence to a locally $D0_{19}$ stacking sequence. In this sense, the difference between the bulk formation energy of those two phases is proportional to the energy of formation of the fault itself. Several $L1_2$ and $D0_{19}$ orderings along the 75 at% Co pseudobinary were enumerated and their formation energies calculated via DFT in

order to gain this baseline information.

In order to more comprehensively study the effects of alloy chemistry on fault energies, the special quasirandom structure (SQS) method was used to enumerate several compositions, including Co_3Al, Co_3W, Co_3Ta, Co_3Ti, Co_3Cr, Co_3V, Co_3Mo and all sub-pseudoternaries. Within each pseudoternary, 13 distinct structures were enumerated for both the $L1_2$ and $D0_{19}$ crystal structures. The $L1_2$ SQS structures contained 24 atoms while the $D0_{19}$ SQS structures contained 32 atoms. Once the formation energies of these structures were calculated, it allowed for a polynomial fit of an SISF energy to be fit at 0 K.

Vibrational calculations were performed on the pure binary $L1_2$ and $D0_{19}$ structures as before using the frozen phonon approach. The resultant vibrational free energies were summed together with the baseline 0 K formation energies to construct an expression for the fault energies as a function of temperature. These surfaces can then be used to identify regions in relatively high-order compositional space that exhibit large fault energies of formation. In this sense, one can identify compositions that are relatively more resistant to fault formation and therefore stronger in creep. These surfaces can also be used to explain some of the chemical segregation behavior that is often observed in post-crept samples [52].

Solute atoms in these faults are known to segregate or deplete from stacking faults in metallic alloys, and specifically in the two-phase γ-γ' Co-Al-W system [53, 54, 55, 56]. Equilibrium in an alloy system is characterized by the equivalence of the chemical potentials of all of the mobile species. However, in a stacking fault, equilibrium is instead determined by the the Suzuki criterion, which corresponds to an equivalence of chemical potential differences. As the Monte Carlo simulations use the grand canonical ensemble, we can easily obtain chemical potential curves as a function of composition. By using this and the Suzuki criterion, we can predict the segregation or depletion of species in a

given Co-Al-W alloy.

To simulate the dynamic shearing process of the $L1_2$ precipitates, 2-D phase-field simulations were conducted. Small 512 x 512 nm square areas were simulated in which a single dislocation was allowed to interact with a single $L1_2$ γ' precipitate for three distinct compositions. To simulate the energetics of the model, a generalized stacking fault (GSF) surface was constructed. This surface was constructed by taking a primitive $L1_2$ cell and elongating it along the z axis into a 1x1x12 supercell. The top (111) layer was then shifted by discrete amounts in order to generate a GSF surface to which a polynomial could be fit. Vacuum layers were included to prevent self-interaction terms.

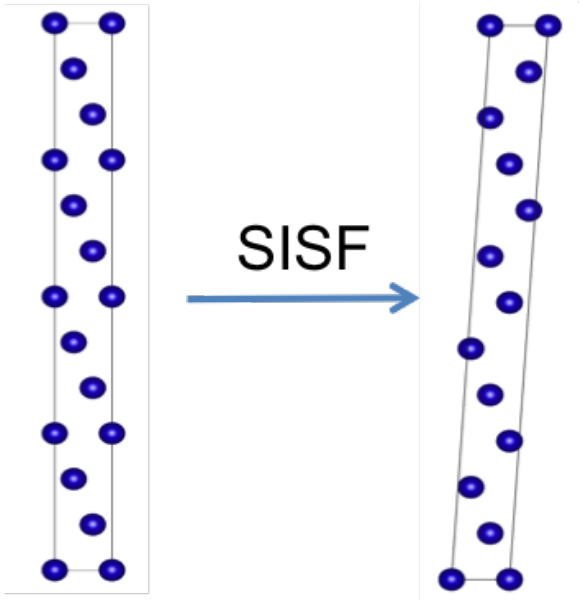

Figure 2.4: Schematic illustration of the (111) shift between the unperturbed FCC supercell and a shift corresponding to the formation of a perfect SISF. Several shifts of this nature can be used to construct the complete GSF surface.

2.1.7 Oxidation

The resistance of Co-base superalloys to oxidation is an important consideration in alloy design. There is wide variation in the type of oxides that can be present in these

alloys depending on the composition of the substrate, especially in higher-order multicomponent alloys. From a first principles standpoint, it can be difficult to directly calculate the activity of oxide species, especially if they have significant solid solubility. If we approximate these oxide compounds as line compounds even at finite temperature, we can use first principles methods to predict the equilibrium layer order of oxides by taking oxygen chemical potential as proportional to oxygen activity.

The first step in calculating the oxide layer sequence is determining the formation energies of the pure oxide species at 0 K via DFT. From there, we can define a new characteristic potential that includes a formation energy and chemical potential term. By minimizing this characteristic potential with varying chemical potential, we can determine the order of oxides on the substrate by assuming oxygen chemical potential increases as we get closer to the surface.

2.2 Experimental methods

First principles methods were used to inform a variety of experiments. The models were used to find a variety of compositions that would have a stable two-phase microstructure, be resistant to $L1_2$ shear, and have adequate oxidation properties. The experimental methods used to explore these properties will be discussed in this section.

2.2.1 Alloy composition

Three single crystal Co-based compositions were investigated in this work, their compositions, and their heat treatments are shown in the table below.

Initially, three Co-Al-W quinary compositions with 2 at% additions of Ta, Ti, and Nb were fabricated via arc melting in order to obtain a γ-γ' microstructure saturated in these elements. These elements were chosen as they had previously been shown to have

Table 2.2: Compositions of alloys (at%)

Alloy	Co	Al	W	Ta	Ti	Nb	Heat Treatment
TaTi	78.3	10.7	8.2	1.2	1.6	-	1340C/48 hrs - 1000C/24 hrs
TaNb	78.8	11.3	7.9	1.1	-	0.9	1340C/48 hrs - 1000C/24 hrs
TiNb	78.3	10.6	8.3	-	1.6	1.2	1315C/48 hrs - 1000C/24 hrs

a positive effect on γ' thermomechanical stability, which had been further validated by first principles modeling [57]. After solution heat treatment, and subsequent precipitation heat treatment, the microstructures of these 2 at% containing alloys were found to be nearly two-phase γ-γ', but with a small amount of additional deleterious phases.

In order to develop a composition with two-phase microstructure, electron probe micro-analysis (EPMA) was performed on the γ-γ' regions within each sample and the resultant composition was used to cast a subsequent set of alloys. This process was repeated until three final quinary compositions were found to possess a completely γ-γ' microstructure after heat treatment. Differential thermal analysis (DTA) was performed on these compositions to obtain γ' solvus temperatures.

2.2.2 Alloy processing

Single crystal bars were cast via the conventional Bridgman process. These bars were cast with crystallographic [001] direction parallel to the growth direction. The bars measured approximately 152 mm in length and 20 mm in diameter. Withdrawal rates of 200 mm/h were used during the casting. A schematic of the Bridgman process is shown in Figure 2.5.

An ALD Vacuum Technologies dual Bridgman-LMC furnace was used, although the liquid metal cooling option was not used in this work [59, 60]. Approximately 4 kg ingots of the compositions in question were inductively melted in a Ni-plugged ceramic crucible. The crucible was then heated to a temperature above the melting point of the Ni plug

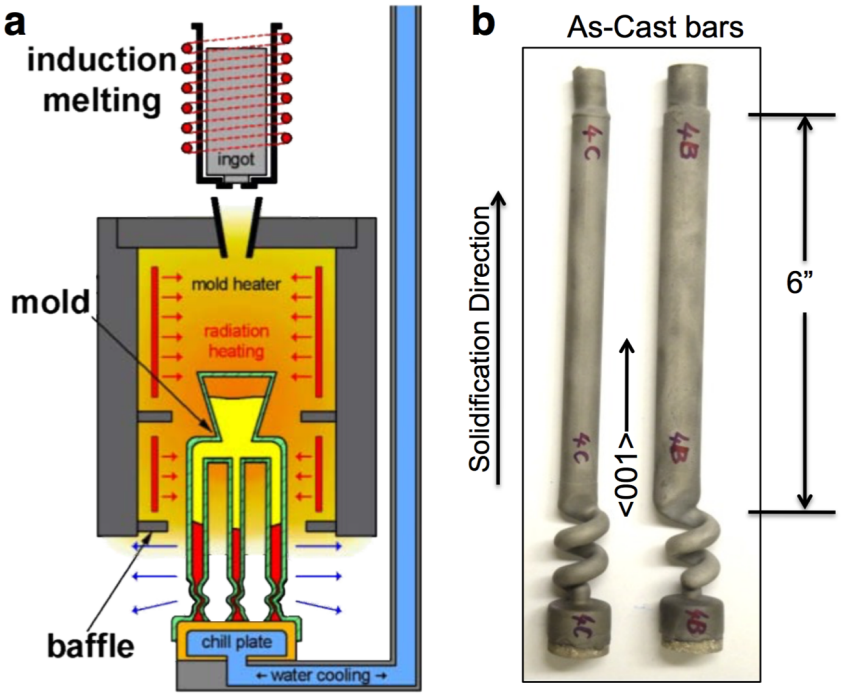

Figure 2.5: a) Schematic of Bridgman casting process. b) Example single crystal bars resulting from Bridgman process. Adapted from [58].

and the molten metal was allowed to pour into a 5 bar ceramic mold located in a heat zone. This mold and the molten metal was maintained at a temperature approximately 100 °C above the liquidus of the alloy.

The mold was subsequently withdrawn from the heat zone at a controlled rate. Spiral grain selectors at the bottom of the mold preferentially control the growth rate of grains with a particular orientation, in this case ultimately selecting an orientation along a [100] type direction. By carefully controlling the withdrawal rate, dendritic growth of a single crystal can then be achieved within the bars themselves.

The resultant single crystals were removed from the mold and heat treated according to the schedule in Table 2.2 in a vacuum resistance furnace. This furnace was backfilled with Ar and heated to a temperature well above the γ' solvus in order to homogenize the as-cast dendritic structure to a complete FCC solid solution. A subsequent aging heat

treatment was then used to nucleate and grow the γ' precipitates.

2.2.3 Microstructural Characterization

In order to characterize the microstructure of the as-cast bars, an etchant solution of 2:1 HCl:H_2O_2 by volume was prepared to determine whether any stray grains had nucleated within the bars. This etchant preferentially attacks the γ phase in Co-base superalloys. The ends of the bars of each composition were sectioned away and electron-probe microanalysis (EPMA) was used to determine whether segregation had occurred within the bar during casting. Back scatter election (BSE) images were also collected on a FEI XL-30 scanning electron microscope (SEM) in order to measure phase fraction.

Differential thermal analysis (DTA) was performed using a Seteram Setsys 18 system on all the alloys investigated. This was done in reference to a Pt sample and the system was calibrated with high-purity Ni and Ag prior to experiment. Transformation temperatures, including the γ' solvus temperature, were recorded during heating and cooling excursions at a rate of 5 K/min.

2.2.4 Creep Testing

Two tensile creep specimens were machined out of each cast bar. High temperature tensile creep tests were conducted in an OXY-GON vacuum resistance furnace with a 3:1 lever arm ratio. In order to accurately capture the deformation of the specimens, extensometers were attached to grooves just outside of the gauge length. Low-voltage displacement transducers (LVDTs) were placed at the bottom of each extensometer and strain measurements were taken by averaging the two resulting measurements.

The single crystal specimens themselves were 76.3 mm in length with a 3 mm gauge diameter and 25.4 mm gauge length. Creep tests varied in temperature from 900 °C to

982 °C and in stress from 248 to 275 MPa. The full parameters of the creep tests are shown in the table below. Temperature was measured by using an R-type thermocouple in contact with the gauge section. Minimum creep rates were established by taking the total average slope over 10 h intervals and taking the minimum value.

Table 2.3: Creep testing of alloys

Sample	Temperature (°C)	Stress (MPa)	End of Test
TaTi-2-1	982	248	Rupture
TaNb-1-1	900	275	2% interrupt
TaNb-2-1	982	248	2% interrupt
TaNb-3-1	982	248	Rupture
TaNb-4-1	900	275	Rupture
TiNb-1-1	900	275	Rupture
TiNb-2-1	900	275	2% interrupt
TiNb-3-1	982	248	Rupture
TiNb-4-1	982	248	20.3% interrupt
TiNb-5-1	950	248	Rupture

Chapter 3

First-Principles Thermodynamics in the Co-Al-W System

3.1 Introduction

Evaluating the thermodynamics of the Co-Al-W ternary system is a critical baseline step in order to design higher-order alloys that have adequate high temperature performance. To this end, several studies have sought to better understand the phase stability of the Co-Al-W system via both CALPHAD and first-principles approaches. The first of these used the special quasirandom structure (SQS) approach with 32-atom supercells and demonstrated that the 0 K formation energy of $L1_2$ $Co_3Al_{0.5}W_{0.5}$ is approximately 70 meV/atom less stable than a three phase mixture of B2 CoAl, A3 Co, and $D0_{19}$ Co_3W [61]. This study assumed equal mixing of Al and W on the B sublattice, although experimentally observed compositions are off stoichiometry with excess Co occupying the B sites and a W concentration higher than that of Al [62]. Other DFT studies exploring the thermodynamic effects of adding vacancies and substitutional defects to the Co-Al-W $L1_2$ structure found that Co antisite defects on Al B sites had a stablizing effect [63].

Furthermore, finite temperature vibrational effects within the harmonic approximation at constant volume were found to increase $L1_2$ stability by reducing the free energy difference between the $L1_2$ and the three-phase mixture above from 70 meV/atom to 11 meV/atom at 1200 K. While this indicates a stabilizing effect due to the vibrational contributions, it is not enough on its own to fully stabilize the $L1_2$ phase [63].

Building on this, a first-principles investigation to establish the role of configurational and vibrational degrees of freedom in determining the stability of $L1_2$ relative to competing phases in the Co-rich part of the Co-Al-W system. A cluster expansion method is combined with Monte Carlo simulations to calculate the configurational free energy of the $L1_2$ phase first along the Co_3Al-Co_3W pseudobinary line and then as a full ternary cluster expansion. Vibrational free energy calculations using the quasiharmonic approximation were also performed and included in the final expression for the Gibbs free energy. The results in this chapter are partially drawn from Rhein, Dodge, et al. [64].

3.2 Pseudobinary Methodology

Our goal was to assess the finite temperature stability of Co-rich $L1_2$ orderings in the Co-Al-W ternary system from first principles. Phase stability is determined by a global minimum of the Gibbs free energy, which can be conveniently visualized when plotting free energies as a function of atomic fractions as schematically illustrated in Figure 3.1. At low temperature, Co-rich alloys in the Co-Al-W ternary decompose into a three phase mixture consisting of pure Co, CoAl, and Co_3W. The free energy of this three phase mixture resides on a plane connecting the free energies of Co, CoAl, and Co_3W as schematically shown in Figure 3.1. Pure Co is stable in the hcp crystal structure (A3) at low temperature but transforms to fcc (A1) above 723 K, while Co-Al adopts the bcc-based B2 ordering. Co_3W is stable in the hcp-based $D0_{19}$ ordering. Although the

experimentally observed $L1_2$ phase in the Co-Al-W is Co-rich, with excess Co occupying the Al and W sites, this initial study was restricted to the pseudobinary $Co_3Al_{1-x}W_x$ composition axis. $L1_2$ becomes thermodynamically stable at temperatures where the free energy of $Co_3Al_{1-x}W_x$ drops below the plane of the free energies of Co, CoAl, Co_3W, as schematically illustrated in Figure 3.1.

Our analysis of phase stability incorporated the effects of both configurational and vibrational excitations. Configurational disorder due to W and Al mixing over the B sublattice of $L1_2$ A_3B along the pseudobinary composition axis x in $L1_2$ $Co_3Al_{1-x}W_x$ will lead to important entropic contributions to the free energy at elevated temperature. Furthermore, several of the other phases that are stable at elevated temperature in the Co-rich part of the Co-Al-W composition space, including A1 Co, B2 CoAl, and $D0_{19}$ Co_3W exhibit solid solubility. Prior experimental work and thermodynamic databases have established that the solid solubility of $D0_{19}$ Co_3W is limited at elevated temperature and can therefore be approximated as a line compound [12, 24]. B2 CoAl, however, exhibits an appreciable degree of off-stoichiometry as a result of Co antisite defects on the Al sublattice, analogous to B2 NiAl [65, 66]. At 1173 K, the B2 structure can accommodate up to 33% Co on the Al sublattice [12]. The configurational entropy associated with this solid solubility may have a significant effect of the free energy of the B2 phase.

Contributions to the free energy from configurational disorder were found using the cluster expansion approach and Monte Carlo simulations. The Al and W ordering over the B sublattice of $L1_2$, for example, can be described with occupation variables σ_i assigned to each site i on the B sublattice with occupation variables taking values of +1 or -1 depending on whether the site is occupied by Al or W. The collection of all occupation variables $\vec{\sigma} = \{\sigma_1, \sigma_2, ..., \sigma_N\}$ uniquely characterizes a configuration over N B-sublattice sites of $L1_2$. The formation energy, $E(\vec{\sigma})$, of a given configuration can then

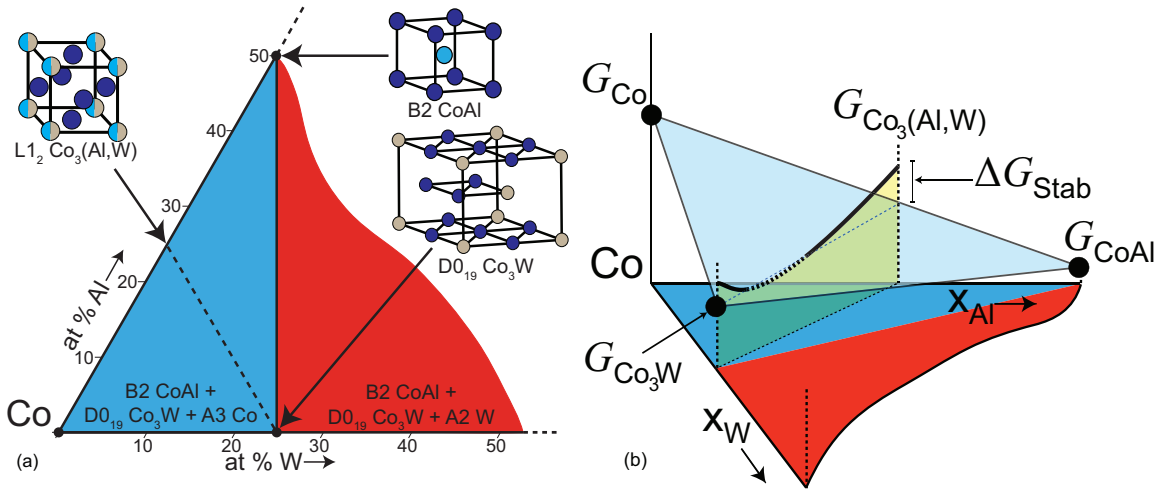

Figure 3.1: (a) Co-rich part of the Co-Al-W phase diagram with labeled crystal structures. Regions with different 0 K ground states are labeled with different colors. Co undergoes a hcp to fcc transition at 723 K. The Co_3Al-Co_3W pseudobinary line corresponding to the cluster expansion is shown. (b) Schematic of the free energies of the crystal structures in the Co-rich part of the Co-Al-W phase diagram at finite temperature.

be expressed as an expansion in terms of polynomial basis functions according to:

$$E(\vec{\sigma}) = V_0 + \sum_{\alpha} V_\alpha \phi_\alpha(\vec{\sigma}) \tag{3.1}$$

where $\phi_\alpha(\vec{\sigma})$ is a cluster function defined as the product of occupation variables belonging to the sites of a cluster labeled α [41]. The coefficients of the cluster functions, V_α, called effective cluster interactions (ECI), depend on the chemistry of the solid and are to be determined from first principles. The resultant cluster expansion can be rapidly evaluated in Monte Carlo simulations to calculate thermodynamic ensemble averages. The CASM package was used to construct and parameterize the cluster expansion and run the Monte Carlo simulations [47, 46, 45, 44].

Binary cluster expansions were constructed for both $L1_2$ $Co_3Al_{1-x}W_x$ and Co rich B2 CoAl due to the importance of configurational disorder in both phases. The expansion coefficients were fit to reproduce a training set of density functional theory energies, each

corresponding to a particular ordering of W and Al over the B sublattice of $L1_2$ or of Co and Al over the Al sublattice of B2 CoAl. A 4-atom $L1_2$ primitive cell was used as a basis for supercell enumeration, in which the face corner site can be occupied by either Al or W, while the face center site is fixed to be Co. All symmetrically distinct configurations of Al and W over the B-sublattice in symmetrically distinct supercells ranging in size between one and five $L1_2$ primitive cells were enumerated. Configurations on B2 supercells up to 18 atoms in size were enumerated from a 2-atom primitive cell in which the Al sublattice was allowed to vary between Al and Co.

The energies of the enumerated configurations as well as those of A1 and A3 Co and $D0_{19}$ Co_3W were calculated with density functional theory using the plane-wave pseudopotential based Vienna *Ab Initio* Simulation Package (VASP) code [36, 67]. The Perdew, Burke, and Ernzerhof (PBE) generalized gradient approximation was used for the exchange and correlation functional with the projected augmented wave (PAW) pseudopotential method [39, 67, 37]. This functional was chosen because of its accuracy in calculating solid cohesive energies [40]. The energies of the ground state crystal structures and selected $L1_2$ configurations were also calculated using the PBEsol functional [68]. An energy cutoff value of 400 eV and a gamma-centered k-point mesh were used. All calculations performed were spin-polarized. K-point convergence tests were performed to within an error of 0.5 meV/atom. Structures were initialized with lattice parameters corresponding to the experimentally-observed $L1_2$ Co_3(Al,W) 3.57 Å and were subsequently fully relaxed.

Grand canonical Monte Carlo simulations were performed on the cluster expansions to calculate the dependence of chemical potential on concentration and temperature. A 12×12×12 simulation cell was used for $L1_2$ $Co_3(Al_{1-x},W_x)$ in which B site occupancy was allowed to vary between Al and W. The free energy of $L1_2$ $Co_3(Al_{1-x},W_x)$ was calculated by integrating the chemical potential with respect to x using Co_3Al as a reference. Monte

Carlo simulations were also performed on the cluster expansion for B2 CoAl to calculate free energies using comparable parameters as for the $L1_2$ structure.

Contributions from vibrational excitations were calculated within the quasi-harmonic approximation. Vibrational free energies for both A1 and A3 Co and for the stoichiometric B2 CoAl and $D0_{19}$ Co_3W compounds were calculated. The vibrational free energy of $L1_2$ along the pseudobinary composition axis $Co_3(Al_{1-x},W_x$ was estimated by linearly interpolating between the vibrational free energies of stoichiometric $L1_2$ Co_3Al and $L1_2$ Co_3W. Force constants were extracted from DFT calculations using the frozen phonon approach. Isolated atoms were displaced relative to their equilibrium positions in large supercells and the resultant forces on all atoms in the supercell were calculated using VASP. Force constants were obtained with a least-squares fit and used to construct the dynamical matrix to calculate phonon diserpersion curves [51]. The volume of the supercells was allowed to vary 5% in 1% increments to enable the calculation of volume dependent Helmholtz free energies. A polynomial fit of the Helmholtz free energy as a function of volume was minimized to calculate the Gibbs free energy as a function of temperature at zero pressure.

3.3 Pseudobinary Results

To parameterize a cluster expansion describing the dependence of the fully relaxed energy on configuration along the pseudobinary $Co_3(Al_{1-x},W_x)$ composition axis, the energies of 63 symmetrically distinct Al and W orderings over the B sublattice of $L1_2$ were calculated. The resulting formation energies ΔE_f are shown in Fig. 3.2a. The formation energies were calculated according to:

$$\Delta E_f = E(\vec{\sigma}) - X_{Co}E_{Co} - X_{Al}E_{Al} - X_W E_W \tag{3.2}$$

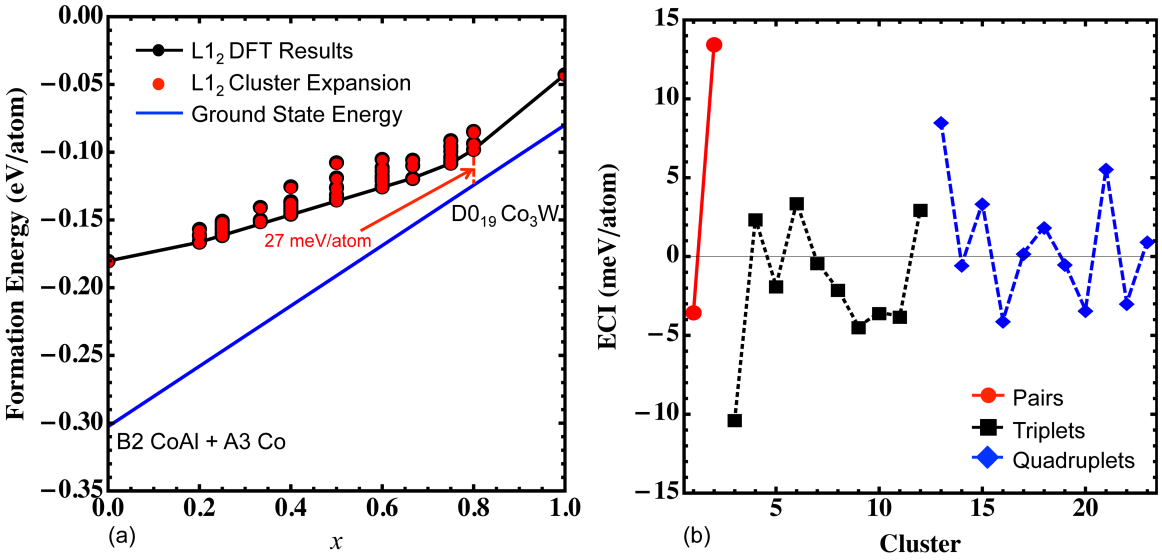

Figure 3.2: (a) Ground state formation energies of the 63 $L1_2$ configurations calculated via DFT and the cluster expansion results relative to the three-phase ground state. X_W represents the atomic fraction of W on the $L1_2$ B sublattice. (b) Magnitude of effective cluster interaction versus cluster number for the $L1_2$ structure.

in which $E(\vec{\sigma})$ is the fully relaxed DFT total energy of configuration $\vec{\sigma}$ and X_i and E_i represent the atomic fraction and DFT energy of the pure elements in their ground states using the PBE functional. Results obtained using the PBEsol functional yielded lattice parameters approximately 1% smaller but did not appreciably change the relative energies between crystal structures. Also shown in Fig. 3.2a is the energy of a three phase mixture of A3 Co-B2 CoAl-$D0_{19}$ Co_3W evaluated along the pseudobinary composition axis x. Fig. 3.2a, clearly shows that $L1_2$ along the pseudobinary composition axis is less stable than a three phase mixture comprising A3 Co-B2 CoAl-$D0_{19}$ Co_3W.

The calculated formation energies in Fig. 3.2a indicate that many Al-W orderings over the B sublattice reside on the convex hull of metastable $L1_2$. Furthermore, the formation energies at fixed concentration x are all very close to each other, exhibiting only a weak dependence on configuration. This is likely due to the fact that the B sublattice sites are separated by a second nearest neighbor distance in fcc and screened by Co on the A sublattice. The variation of the formation energies with composition and

configuration suggests that a solid solution due to Al-W disorder over the B sublattice should form at elevated temperatures in $L1_2$ $Co_3(Al_{1-x},W_x)$

At 0 K, there is no composition at which the $L1_2$ crystal structure is favored relative to the three phase mixture, although it becomes more energetically competitive at compositions that are rich in W. The -605 meV/atom formation energy (relative to A3 Co and A1 Al) of B2 CoAl is the largest in magnitude of all structures considered, effectively destabilizing $L1_2$ structures at the Al rich end of the pseudobinary. It is convenient to consider a relative stability free energy along the pseudobinary, defined as the difference between the free energy of a $L1_2$ based configuration $\vec{\sigma}$ at a particular concentration and the free energy of a three-phase mixture of Co, CoAl, and Co_3W at the same composition:

$$\Delta G_{stab}(x,T) = G_{L1_2}(x,T) - G_{Mixture} \tag{3.3}$$

At zero Kelvin, where the entropy is zero, the free energies in the above definition become equal to formation energies. Due to the very strong relative stability of the B2 CoAl phase, the smallest difference between the three-phase CoAl, Co_3W, and Co mixture and the $L1_2$ Co_3(Al,W) phase at 0 K is 27 meV/atom, as shown in Figure 3.2a. This energy difference lowers to 22 meV/atom if the PBEsol functional is used. This minimum occurs at W rich composition.

The $L1_2$ cluster expansion was fit to the 63 formation energies of Figure 3.2a using a genetic algorithm [48] and a depth first search method [45] to determine the optimal set of basis functions. The final basis set comprised of 25 clusters with the cluster expansion fit having a cross-validation score of 0.5 meV/atom, an error comparable in magnitude to the expected numerical convergence errors of the DFT calculations. The magnitude of the ECIs are shown in Figure 3.2b. The largest pair interaction connects B-sublattice sites of opposite corners of the $L1_2$ cubic unit cell, having a magnitude of 13.5 meV/atom.

The most closely-packed triplet and quadruplet clusters have magnitudes of 10.3 and 8.5 meV/atom, respectively. The formation energies predicted by the cluster expansion are overlaid in red on the DFT formation energies in Fig. 3.2a.

The zero Kelvin DFT prediction that a three phase mixture of A3 Co, B2 CoAl and $D0_{19}$ Co_3W is more stable than any configuration along the $L1_2$ $Co_3(Al_{1-x},W_x)$ pseudobinary suggests that other finite temperature effects are responsible for the experimentally observed $L1_2$ crystal structure. Contributions from configurational entropy to the free energy due to Al/W mixing over the B sublattice of $L1_2$ are a potential source of finite temperature stability. Semi-grand canonical Monte Carlo simulations were performed on the cluster expansion for $L1_2$ $Co_3(Al_{1-x},W_x)$ to calculate a relation between the exchange chemical potential $\tilde{\mu}_W = \mu_W - \mu_{Al}$ and B sublattice concentration x. This exchange chemical can be integrated with respect to x to obtain an expression for the Gibbs free energy, G_{config}, of $L1_2$ according to:

$$G_{config}(x) = G_{config}(x^{ref}) + \int_{x^{ref}}^{x} \tilde{\mu}_W dx \tag{3.4}$$

where x^{ref} represents a reference W concentration on the B sublattice. The reference concentration was taken as x=0 and the Gibbs free energy at that concentration, $G_{config}(x^{ref})$, is equal to the formation energy of the $L1_2$ Co_3Al configuration due to the absence of configurational entropy in a perfectly ordered compound.

The Gibbs free energy is plotted as a function of x at three different temperatures in Fig. 3.3. The effects of configurational entropy are greatest at $Co_3Al_{0.5}W_{0.5}$ where there is equal mixing of Al and W on the B sublattice. At 0 K, the relative stability energy at this composition is 56 meV/atom. When finite temperature contributions due to configurational excitations are accounted for, ΔG_{stab} decreases but remains positive. At 1173 K, where $L1_2$ is experimentally observed, ΔG_{stab} decreases to 43 meV/atom,

indicating that a three phase mixture between Co, CoAl and $D0_{19}$ Co_3W is still favored in spite of the additional configurational entropy in $L1_2$. At concentrations $x > 0.5$, $L1_2$ becomes more competitive relative to the Co-CoAl-Co_3W mixture but the stabilizing effect of configurational entropy is also less than that at $x = 0.5$. Compositions containing 80 ± 2.5 at% W on the $L1_2$ B sublattice remain the most competitive relative to the three-phase ground state in the 873-1473 K temperature range when configurational effects are incorporated. The most favorable composition at 1173 K is $Co_3Al_{0.19}W_{0.81}$ with a stability free energy of ΔG_{stab} = 19.6 meV/atom. Even at temperatures approaching melting, contributions from configurational excitations are not sufficient to stabilize $L1_2$ relative to the three-phase ground state.

The vibrational free energies of pure Co (both fcc and hcp), B2 CoAl, and $D0_{19}$ Co_3W were calculated within the quasi-harmonic approximation. The vibrational entropy is equal to minus the slope of the vibrational free energy with respect to temperature. The vibrational entropies of fcc Co, B2 CoAl, and $D0_{19}$ Co_3W are shown in Figure 3.4a. The B2 CoAl compound has the lowest vibrational entropy among the three phases. Shorter bond lengths are generally associated with stiffer bonds and therefore less vibrational entropy [69]. The nearest neighbor bond length of B2 CoAl is 2.47 Å, which is shorter than the 2.50 Å and 2.55 Å nearest neighbor bond lengths in fcc Co and $D0_{19}$ Co_3W, respectively. Strong Co-Al bonds in B2 CoAl is consistent with the very large magnitude of the B2 CoAl formation energy.

The vibrational free energies of $L1_2$ Co_3Al and $L1_2$ Co_3W were also calculated within the quasi-harmonic approximation. The vibrational entropy as a function of temperature for the two $L1_2$ compounds is shown in Figure 3.4b. At 1173 K, there is an approximate 0.5 k_b/atom difference in vibrational entropy between $L1_2$ Co_3Al and $L1_2$ Co_3W. The vibrational entropy of $L1_2$ Co_3W is slightly lower than that of $L1_2$ Co_3Al in spite of the heavier mass of W. This may be due to stronger bonds in the W-compound as Co-

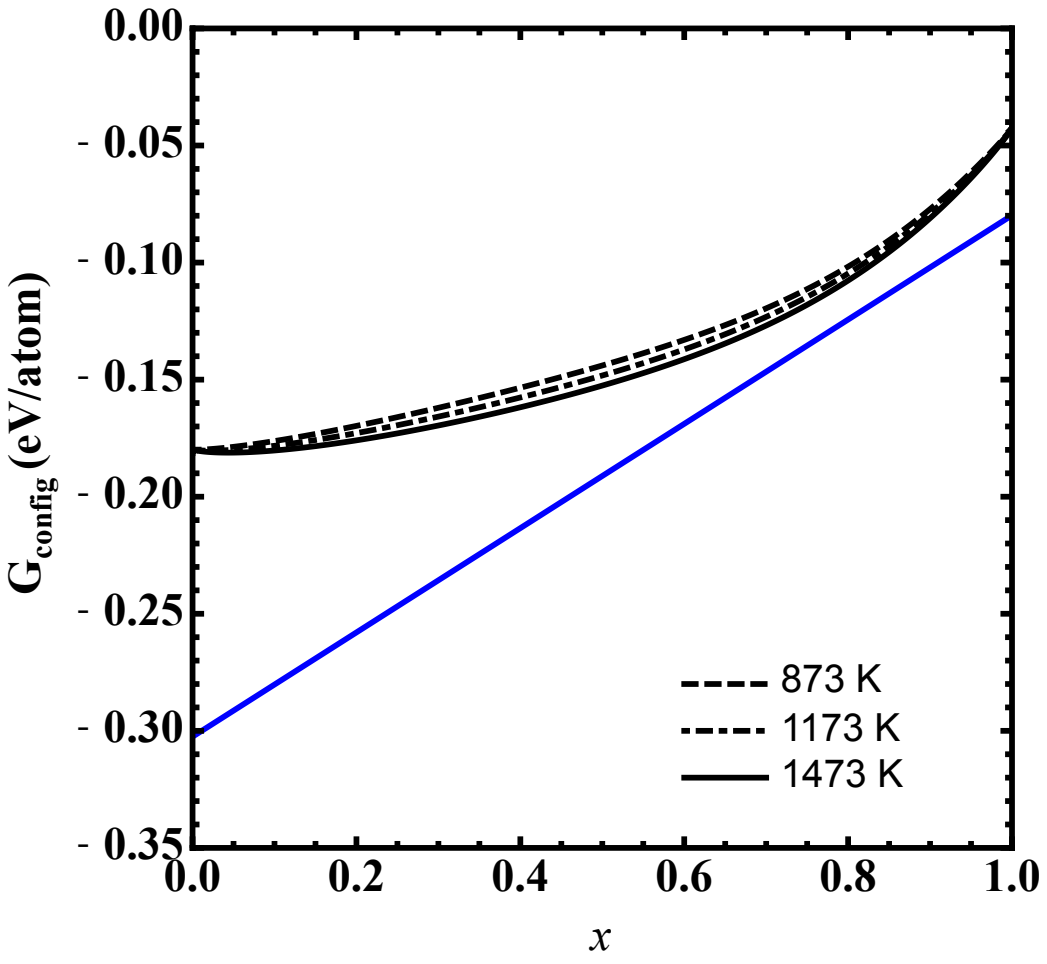

Figure 3.3: Effect of configurational entropy on the $L1_2$ structure. Black $L1_2$ free energy curves at increasing temperature are plotted relative to the free energy of the three-phase ground state in blue.

W prefers close-packed phases at the $L1_2$ composition, while Co-Al prefers a two-phase mixture between bcc based B2 CoAl and Co at the same composition.

It is computationally prohibitive to calculate the vibrational entropy of all 63 structures along the pseudobinary line used to fit the cluster expansion for $L1_2$. Therefore, the vibrational free energy at intermediate compositions were modeled as a rule of mixtures between the Co_3Al and Co_3W endpoints. Configurational and vibrational entropy in the $L1_2$ structure along the Co_3Al-Co_3W pseudobinary line are plotted against each

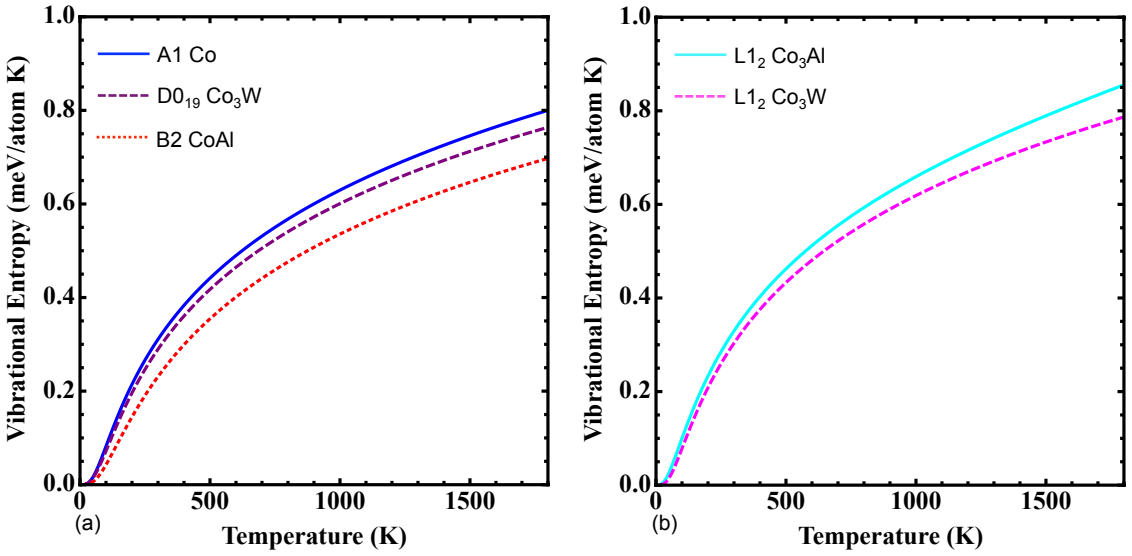

Figure 3.4: Vibrational entropy as a function of temperature of the three phases comprising the ground state (a) and the $L1_2$ endpoints of the pseudobinary (b).

other in Fig. 3.5. In this plot, the vibrational entropy is measured relative to the vibrational entropy of an equivalent three-phase mixture of Co, CoAl, and $D0_{19}$ Co_3W at a given composition. It is clear that vibrational entropy is much greater in magnitude than configurational entropy across the pseudobinary, especially at the Al-rich end. It is also notable that the configurational entropy is very close to the ideal entropy of mixing, suggesting that there is a nearly random solid solution of Al and W on the B sublattice in the $L1_2$ structure.

A complete expression for the Gibbs free energy of a crystal structure is approximated by summing the 0 K formation energy with the configurational and vibrational energy terms. For $L1_2$ along the pseudobinary with B sublattice concentration x, the expression takes the following form:

$$G(x,T) = \Delta E_f + G_{config}(x,T) + G_{vib}(x,T) \tag{3.5}$$

An analogous free energy expression can be obtained for the three phases that make up

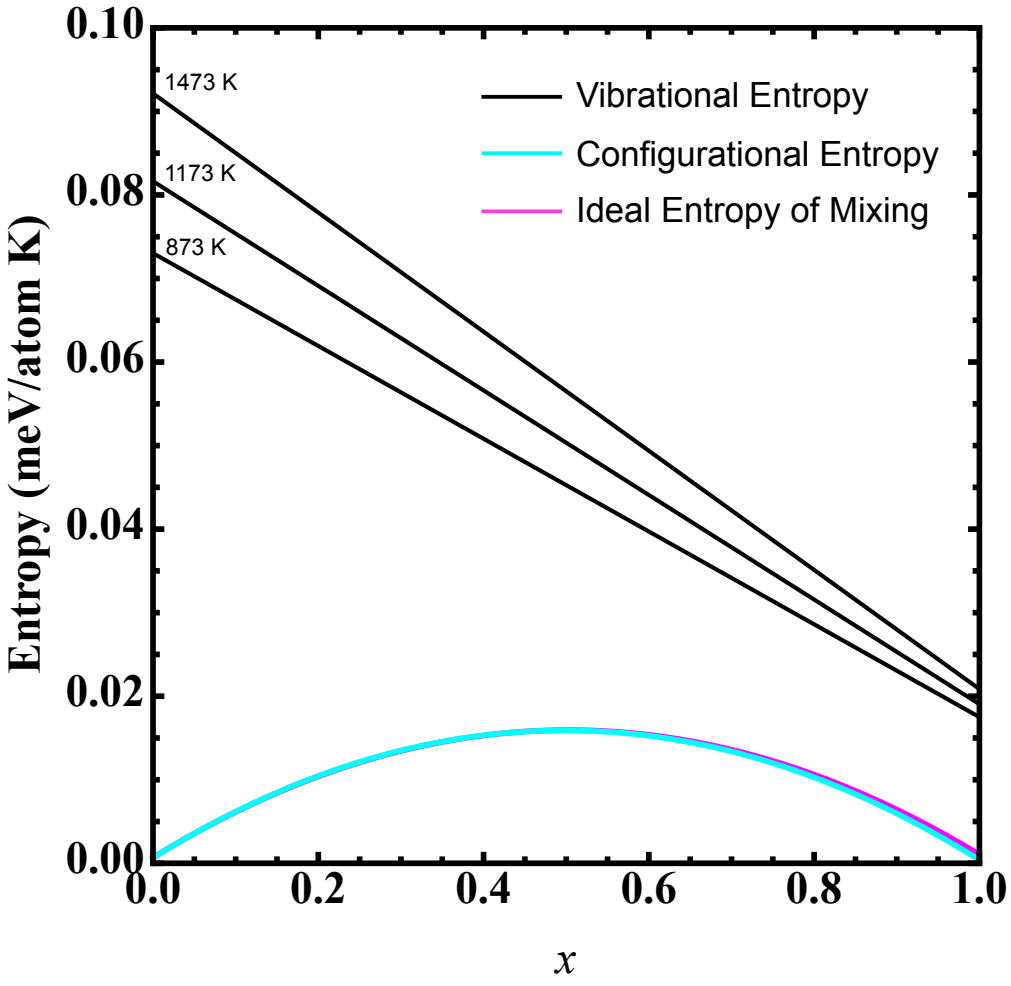

Figure 3.5: The effect of configurational and vibrational entropy in the $L1_2$ phase along the Co_3Al-Co_3W pseudobinary line. Vibrational entropy is assessed as a rule of mixtures between the two end $L1_2$ structures relative to the vibrational entropy of an equivalent three phase mixture of A1 Co, B2 CoAl, and $D0_{19}$ Co_3W at a given composition.

the end points of the convex hull, but treating them as line compounds. The relative stability free energy ΔG_{stab} of $L1_2$ along the pseudobinary is shown in Figure 3.6 with increasing temperature.

At 873 K the $L1_2$ phase becomes stable relative to the Co-CoAl-Co_3W three phase mixture, with a ΔG_{stab} of -2.2 meV/atom with 74% W on the B sublattice. The magnitude of ΔG_{stab} increases with increasing temperature, lowering to -17 meV/atom at

1173 K. The compositions with the greatest $L1_2$ stability at this temperature are those with approximately 70% W on the B sublattice, which is consistent with experimentally-observed compositions [12]. If the PBEsol functional is chosen to calculate formation energies, it is found that ΔG_{stab} will decrease by approximately 5 meV/atom at the most stable $L1_2$ compositions. This choice would lower the calculated transition temperature at which $L1_2$ becomes stable relative to the three phase mixture.

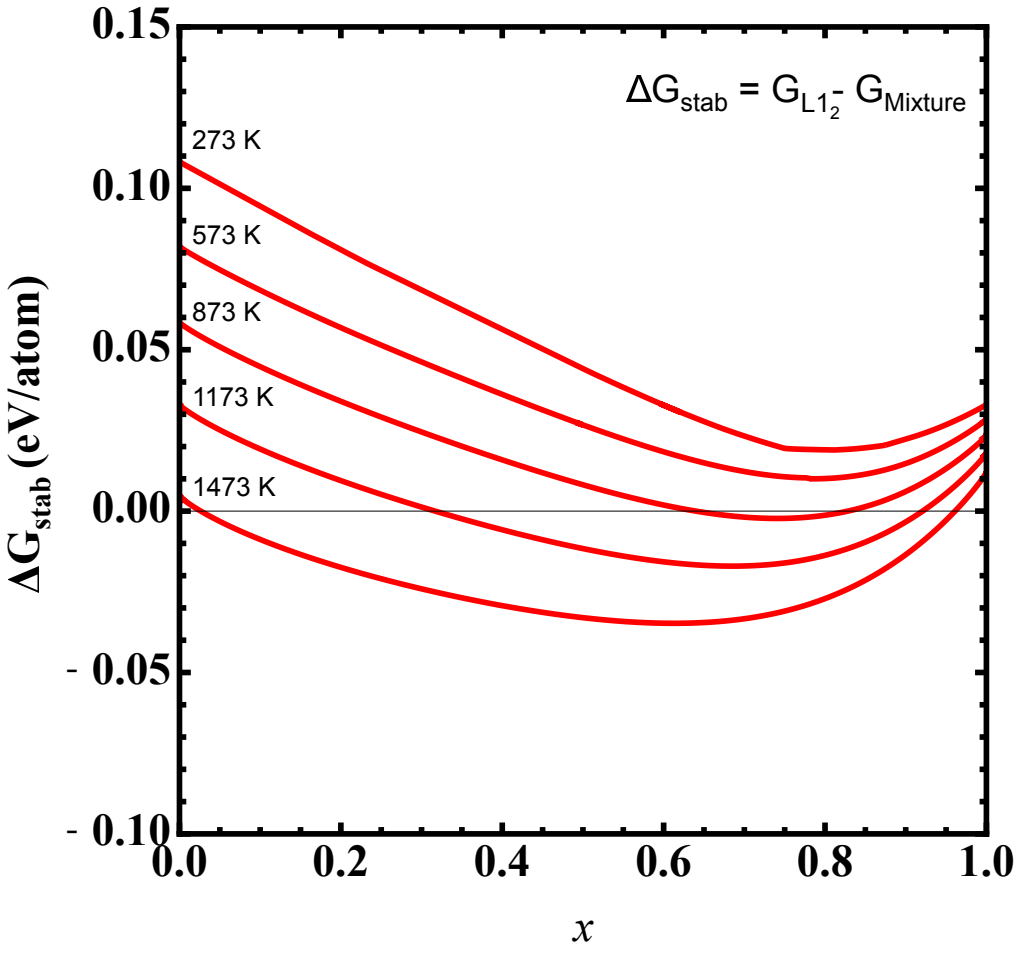

Figure 3.6: Stability energy of the $L1_2$ structure relative to the three-phase ground state with increasing temperature.

Our pseudobinary analysis has assumed that the three phases that are thermodynamically competitive with $L1_2$ can be approximated as line compounds at elevated

temperature. While $D0_{19}$ Co_3W does not exhibit significant solubility, B2 CoAl and fcc Co have appreciable solid solubility and these effects must be accounted for in order to completely assess relative phase stability. Results from Monte Carlo simulations indicate that inclusion of configurational degrees of freedom in the free energy of B2 CoAl does not appreciably change the free energy of the Al-rich end of the Co_3Al-Co_3W pseudobinary. Caution should be used in drawing conclusions from the stability free energy at temperatures approaching the solvus temperature of the $L1_2$ phase as configurational entropy arising from an increased solubility of Al and W in fcc Co will lower its free energy and thereby reduce ΔG_{stab} and make $L1_2$ less stable than predicted here. Incorporating the effects of solid solubility in elemental cobalt through a ternary cluster expansion remains a critical step in rigorously assessing phase stability in the Co-Al-W from first-principles and will be discussed in later sections.

It has been demonstrated that $L1_2$ Co_3(Al,W) is thermodynamically competitive relative to pure Co, CoAl, and Co_3W at high temperature due to the combined effects of configurational and vibrational entropy. Our rigorous treatment of configurational degrees of freedom using the cluster expansion method showed that the entropy due to Al-W disorder over the B site of $L1_2$ at high temperature approaches that of an ideal solution. While configurational entropy is thereby maximized it is not large enough to stabilize $L1_2$ relative to Co, CoAl, and Co_3W. Vibrational entropy is found to be substantially more important in stabilizing $L1_2$. Vibrational entropy is predicted to be larger in the fcc phases (fcc Co and $L1_2$) than in B2 CoAl and the hcp phases (hcp Co and $D0_{19}$ Co_3W). The very negative formation energy of B2 CoAl, which favors this phase at low temperature, translates into stiff Co-Al bonds. As a result, B2 CoAl has the lowest vibrational entropy of all the phases considered in this work and its free energy decreases least with increasing temperature. Our study demonstrates that the inclusion of thermal expansion as modeled within the quasi-harmonic approximation is essential to

render $L1_2$ thermodynamically stable at elevated temperature. A recent study by Saal et al [63], for example, showed that vibrational free energies calculated at constant volume are insufficient to stabilize $L1_2$.

The $L1_2$ phase that emerges at high temperature is predicted to be W rich (relative to Al). This is in large part due to the very negative formation energy of CoAl at zero Kelvin. Vibrational and configurational entropy favors slightly higher Al concentration as their inclusion causes the minimum of ΔG_{stab} to shift to more Al rich concentrations with increasing temperature. The shift though is small and the B sublattice of $L1_2$ remains net rich in W at all temperature, which is consistent with experimentally-observed compositions.

In evaluating the vibrational free energy of $L1_2$ $Co_3(Al_{1-x}W_x)$ as a function of x, the vibrational free energies of $L1_2$ Co_3Al and Co_3W were linearly interpolated. While an approximation, it becomes more accurate when the dependence of the vibrational free energy on the arrangement of Al and W is weak. A linear approximation should be reasonable in this system since configurational disorder in $L1_2$ $Co_3Al_{1-x}W_x$ occurs over the B sites, which are relatively far apart and are shielded from each other by the majority Co sublattice. This is further supported by the calculations of Saal et al [63] who showed that the vibrational free energy at constant volume for two different configurations at the same concentration in $L1_2$ $Co_3Al_{1-x}W_x$ differ only by 3 meV/atom, indicating that the vibrational free energy is relatively insensitive to the Al-W arrangement. Hence a more rigorous coupling between configurational and vibrational excitations using for example a coarse graining scheme [70] is not necessary.

The calculated 873 K temperature above which $L1_2$ is predicted to become stable is below temperatures where $L1_2$ is experimentally observed. Due to a variety of approximations in our treatment, it is expected that this predicted transition temperature is a lower bound. Neglected in our initial study are the entropic contributions from configu-

rational disorder of dissolved Al and W in fcc Co. Entropic contributions from magnetic disorder in fcc Co have been neglected. Entropy arising from spin-spiral excitations have been shown to strongly influence the hcp/fcc transition temperature for example [71]. The inclusion of both of these effects would stabilize elemental Co relative to the other phases and thereby increase the temperature at which $L1_2$ Co_3(Al,W) becomes thermodynamically stable.

It has been shown that vibrational entropy is critical in order to thermodynamically stabilize the $L1_2$ phase in the Co-Al-W ternary. Having identified a compositional range in which this structure is most stable, it becomes evident as to how to increase the stability of $L1_2$ through further alloying. Additional components should favor $L1_2$ formation and competing phases that have a low vibrational entropy so as not to destabilize $L1_2$ at elevated temperature. It is expected that higher order alloying additions, such as Ni, Ta, and Ti, will further stabilize $L1_2$ in Co rich alloys.

3.4 Ordering on Lattices

A necessary first step in conducting a full ternary thermodynamic assessment of the Co-Al-W system is to consider the 0 K phase diagram. Using VASP, the formation energies of several ternary compounds were calculated via DFT. The Inorganic Crystal Structure Database (ICSD) was used to identify several possible parent crystal structures which were then decorated with Al, Co, and W atoms [72].

There are several notable points on the 0 K Co-Al-W phase diagram. All formation energies were taken relative to the three constituent elements in their ground state. There is a complete absence of ternary intermetallic structures at 0 K. Several ternary topologically closed-packed (TCP) and Laves phases had their formation energies calculated but were not found of the global convex hull. Several three-phase regions are present in

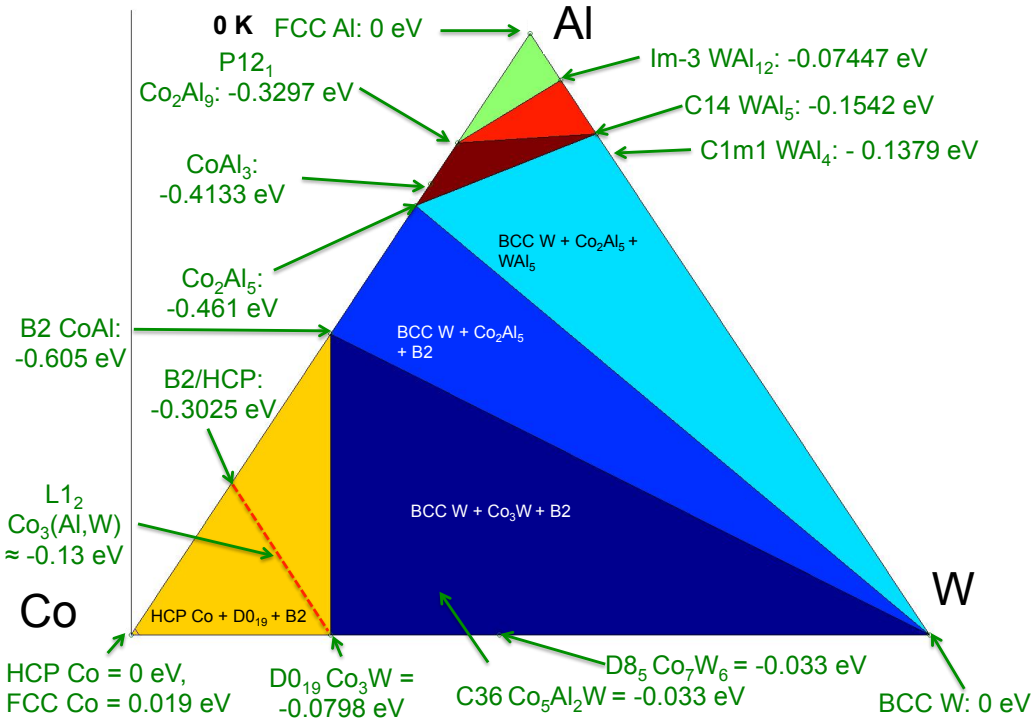

Figure 3.7: Phase diagram of the Co-Al-W at 0 K. The red dashed line indicates the 75 at% pseudobinary line from the previous study. Other notable phases are indicated by the green arrows.

the phase diagram, but of most interest is the HCP Co + $D0_{19}$ Co_3W + B2 CoAl phase field for Co-rich composition. As mentioned in the pseudobinary analysis, this three-phase region is more stable than any calculated individual $L1_2$ orderings along the red dashed line. Several other ternary $L1_2$ orderings were considered in this later analysis, as prior research had shown that Co antisite defects on the minority B sublattice have a stabilizing effect [63]. For the ternary $L1_2$ configurations considered in our analysis, no such stabilizing effect was found as Co-rich compositions off of the pseudobinary were higher in relative energy than those along the pseudobinary itself. The major driver of the stability of the three-phase region is again the very low formation energy of the B2 CoAl compound.

Although no ternary $L1_2$ phases are observed at 0 K, an important next step is

to consider the FCC ground states in isolation to see if there are any orderings that are particularly thermodynamically competitive with the three-phase mixture. These orderings may also become stabilized by finite temperature effects so identifying them accurately is important. A comparison plot showing the FCC and global convex hulls is shown in Figure 3.8(a). As seen in this plot, there are no FCC configurations that lie on the global convex hull, with the exception of elemental Al. There are, however, a number of ternary configurations that adopt the $L1_2$ ordering that are on the FCC convex hull, as shown in Figure 3.8(b). As before, these configurations lie on the 75 at% pseudobinary line and are 10s of meV/atom off of the global convex hull.

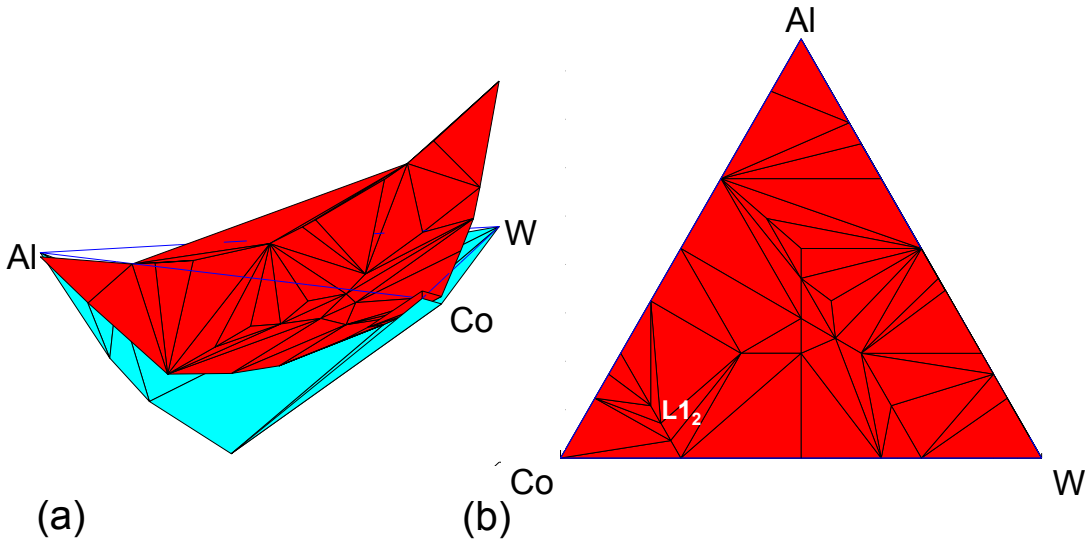

Figure 3.8: (a) Comparison of the Co-Al-W FCC ground state convex hull in red to the global ground state convex hull in cyan. (b) The ground states at vertices in the FCC parent crystal structure at 0 K, including $L1_2$ configurations along the 75 at.% pseudobinary line.

The three FCC configurations that reside on the FCC convex hull are shown in Figure 3.9. These configurations do not show a strong bias toward either Al or W on the B sublattice, but are rather clustered around the equimolar Co_3(Al,W) composition. The configurations denoted 30 and 34 in Figure 3.9 are relatively similar to one another,

consisting of alternating (100) planes. In these alternating planes, a plane that is entirely Al or W is succeeded by another plane consisting of atoms in a 2:1 ratio of the minority species to the majority species. The final configuration, denoted 4 in Figure 3.9, is equimolar on the B sublattice. Notably there appears to be no strong preference for a certain type of nearest neighbor bonding on the B sublattice. W is a relatively large atom and so it might be expected that stable configurations would seek to minimize the number of W-W nearest neighbors on the B sublattice but that is not found in the configurations shown below. Nearest neighbors on the B sublattice are second nearest neighbors on the overall FCC lattice, allowing for Co to effectively shield atoms from one another on the minority B sublattice.

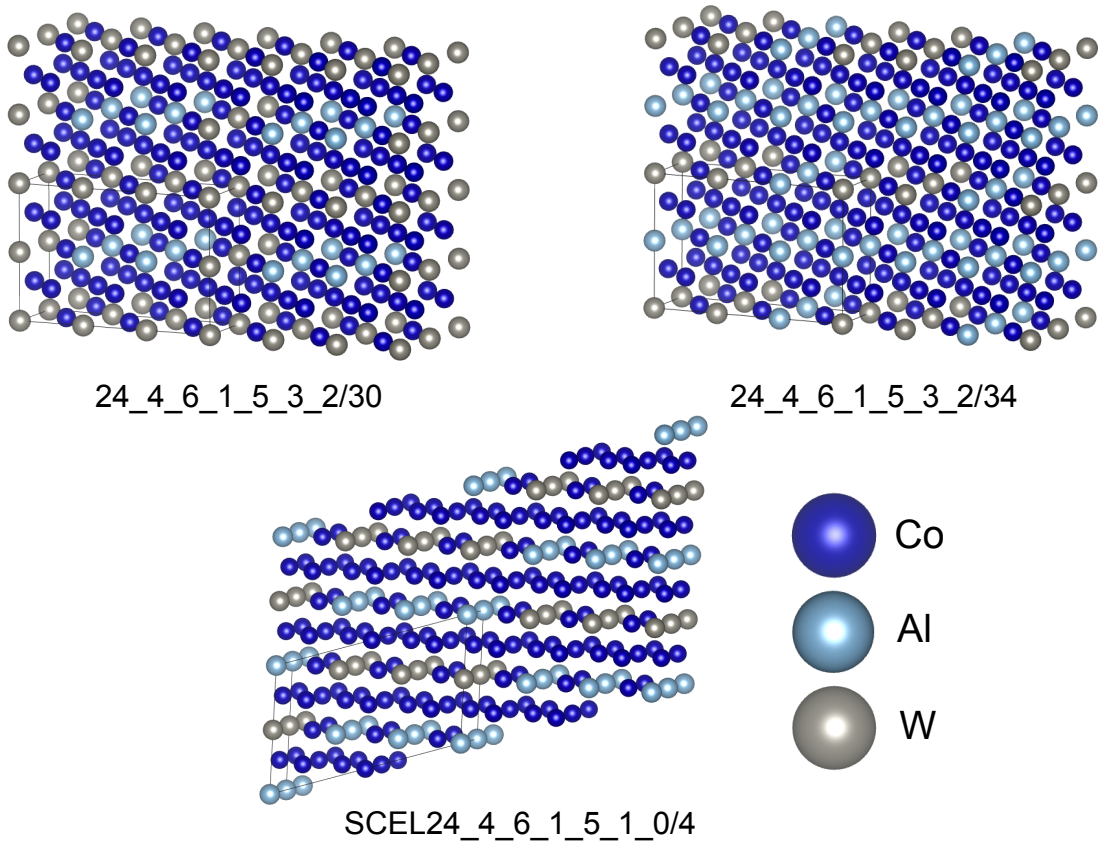

Figure 3.9: The three FCC ground states that reside on the FCC convex hull. All configurations are 24 atoms large. Images generated using VESTA and species type is indicated.

3.5 Fitting Cluster Expansion

The first step in fitting the three ternary cluster expansions was to use the components of the Hencky strain to identify configurations which significantly deviate from their starting parent crystal structure. One such transformation pathway is the Bain strain pathway from FCC to BCC. As configurations that are of multiple different crystal structures are undesirable in fitting a cluster expansion, a filter of the original configurations must be conducted and only the desired configurations used. An example plot used to filter the FCC configurations is shown in Figure 3.10. Strain transformations from BCC to FCC can also be mapped onto e_2-e_3 space if the BCC crystal is taken as reference. The pathways are the same as the Bain strain paths for FCC but in the opposite direction. Just as with FCC to BCC, there are three equivalent paths related to one another by 120° rotations in e_2-e_3 space. Configurations that do not deviate strongly from their starting configuration as measured by the second and third component of the Hencky strain pass the filter and are used in the subsequent cluster expansion.

In this work, all relaxed configurations were compared to ideal FCC, BCC, and HCP parent crystal structures. The vast majority of these orderings will not stay perfectly FCC, BCC, or HCP as they will not possess perfect cubic and hexagonal symmetry after relaxation. Nonetheless, these structures will be considered as belonging to the parent crystal structure they most closely map to.

Although three cluster expansions were fit, the fitting of the ternary FCC cluster expansion will be the primary focus of this work. A comparison between the actual DFT formation energies and the formation energies predicted from the cluster expansion along the Co-Al binary axis is shown in Figure 3.11. In this figure, the original DFT formation energies are denoted with open red circles while the corresponding cluster expansion (CLEX) energies are denoted by smaller, filled-in blue circles. The FCC cluster expansion

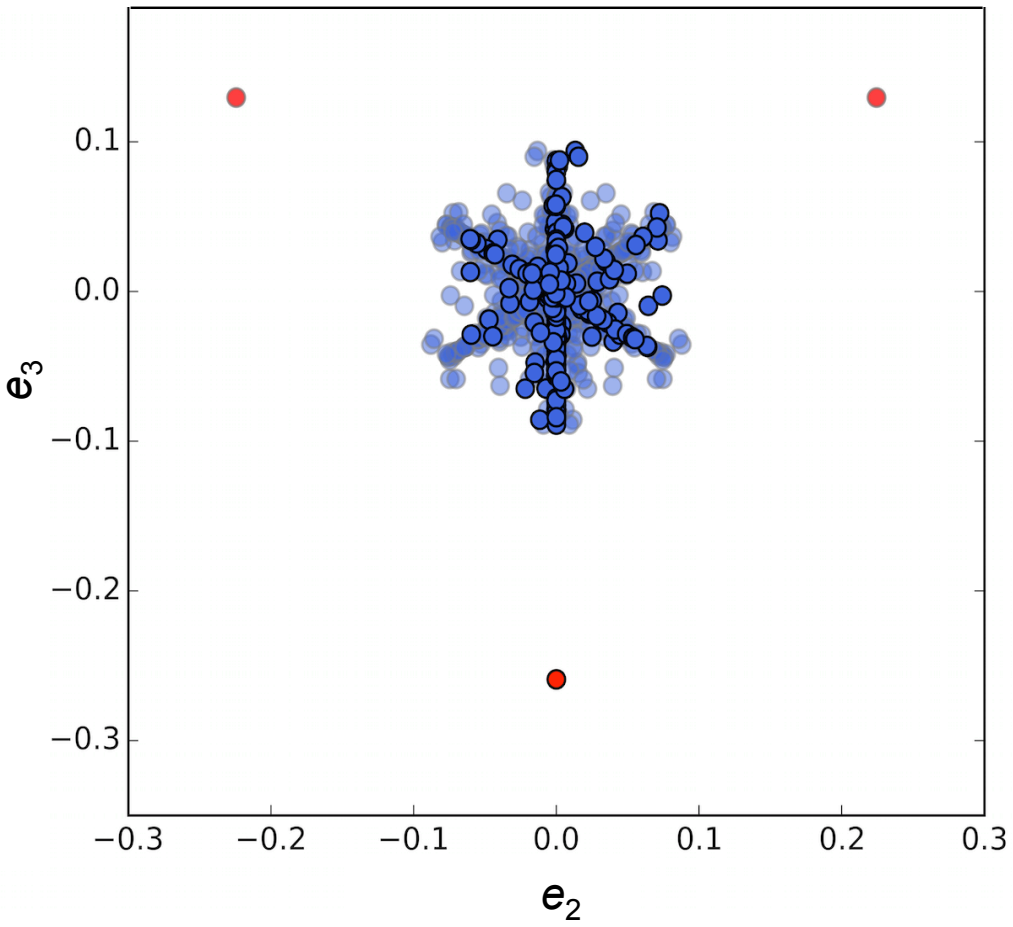

Figure 3.10: The 699 original FCC configurations that did not deviate by more then 0.1 in either e_2 or e_3 are shown in blue. These configurations were used in the subsequent cluster expansion. The three red points correspond to the full Bain strain pathway in which an original FCC structure would transform completely to BCC.

was fit to at total of 699 formation energies using the same genetic algorithm [48] as used for the pseudobinary fit. The final cross-validation score was 13.8 meV/atom, although it is apparent in Figure 3.11 that the fit is better in the Co-rich part of composition space. This is partially due to the relatively few configurations that can be used for the FCC fit in the composition space around CoAl. Due to the large formation energy of the BCC B2 CoAl ordering, it is energetically favorable for FCC configurations to transform to BCC via the Bain pathway. This is especially apparent at the equimolar CoAl composition, where only four configurations that were originally FCC relax to a configuration that

maps most closely to FCC. The configurations comprising the cluster-expanded FCC convex hull are indicated by gold stars in Figure 3.11, and there is strong agreement between the DFT and CLEX hull in the Co-rich part of the composition range shown here.

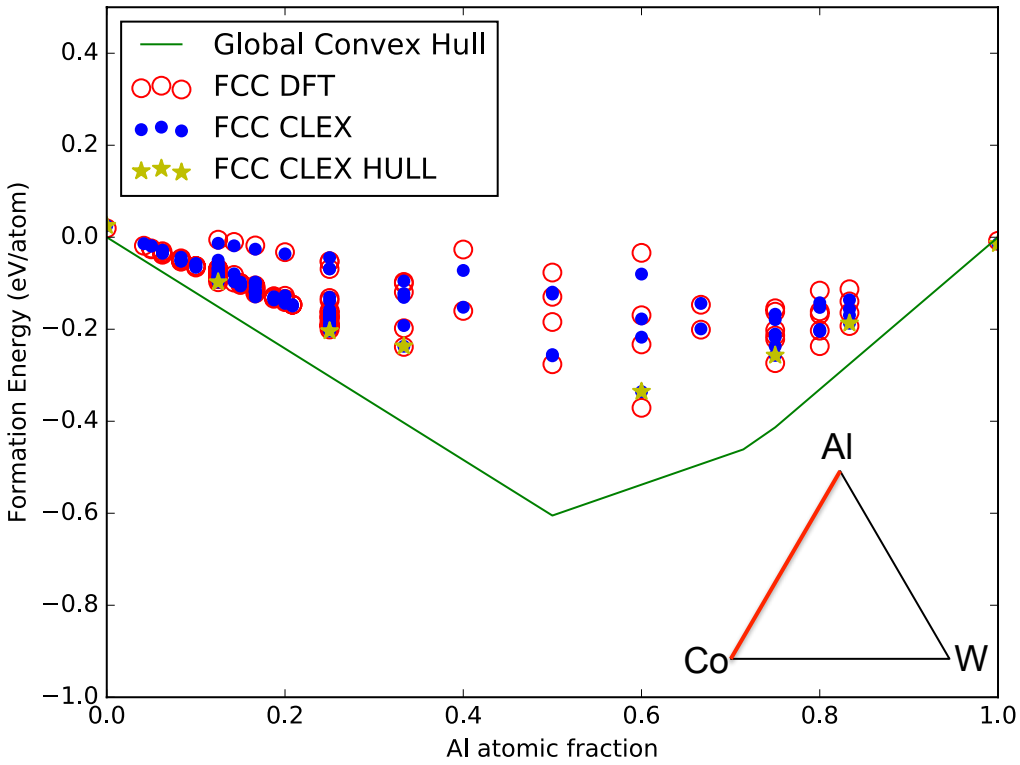

Figure 3.11: The DFT and cluster expansion (CLEX) predicted formation energies of the FCC configurations along the Co-Al binary.

A comparison between the DFT formation energies and those predicted by the cluster expansion along the Co-W binary axis is shown in Figure 3.12. There are more configurations to fit to in the middle of this composition range than along the Co-Al binary and once again, there is strong agreement between the actual and predicted energies near elemental Co in the region of interest. Of note here is that the energy of $L1_2$ Co_3W is very near the energy of $D0_{19}$ Co_3W that resides on the convex hull. This once again

suggests that W-rich $L1_2$ compositions will be more energetically competitive with the three-phase ground state than Al-rich compositions.

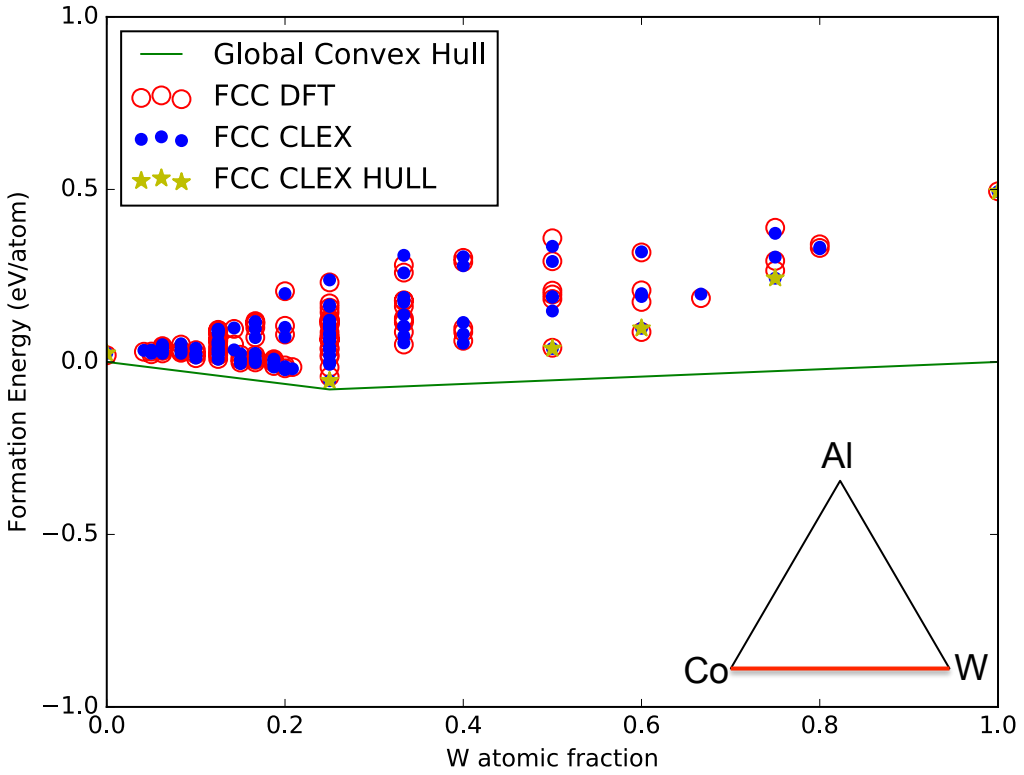

Figure 3.12: The DFT and cluster expansion (CLEX) predicted formation energies of the FCC configurations along the Co-W binary.

It is also important to consider the fit of the configurations along the 75 at% Co pseudobinary line, both as a check with the prior work and to determine which configurations lie on the FCC convex hull. A plot of the 75 at% Co pseudobinary for the ternary FCC cluster expansion is shown in Figure 3.13. This figure is directly comparable to Figure 3.2(a), and there is strong agreement between the two. The ternary cluster expansion is more coarse in composition space than the pseudobinary cluster expansion. Because of this, an additional 233 configurations were added to the ternary FCC cluster expansion centered in the compositional region where $L1_2$ Co_3(Al,W) is experimentally observed.

These configurations allowed for the inclusion of Co antisite defects on the B sublattice. Unlike the calculations performed by Saal and Wolverton [63], it was not observed that these antisite defects have a stabilizing effect as these configurations are further away from the three-phase ground state convex hull. This may be due to differences in calculation technique, as smaller supercells were used in this work and the stability energy was measured relative to the three-phase ground state rather than as an absolute value. They were nonetheless included in the final FCC cluster expansion.

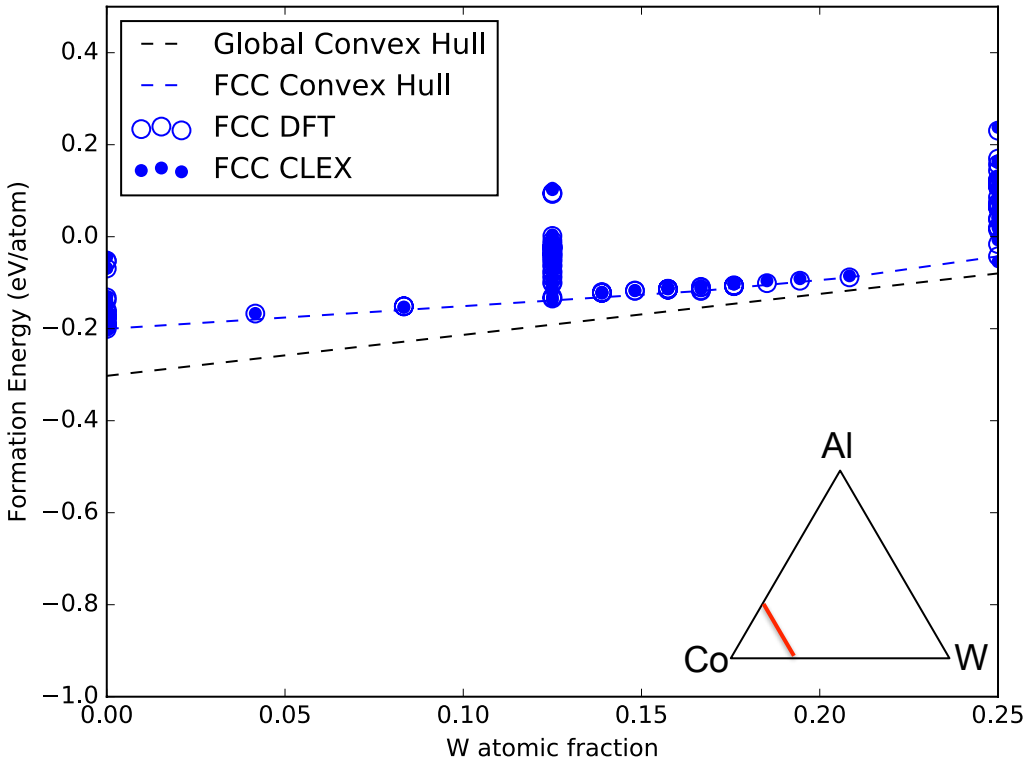

Figure 3.13: The DFT and cluster expansion (CLEX) predicted formation energies of the FCC configurations along the 75 at% pseudobinary.

As the BCC cluster expansion is similarly coarse in composition space, an additional 169 configurations near the B2 CoAl composition were added before the final fit. These configurations were rich in Co relative to B2 CoAl, as seen in Figure 3.14, comprising

orderings with Co antisite defects on the Al sublattice. While these configurations do not reside on the convex hull, they were included in order to capture effects of solid solubility in the B2 phase. It has been shown that these antisite defects are responsible for Ni solubility in the Ni-Al system and it is expected that the Co-Al system exhibits analogous behavior [66, 28].

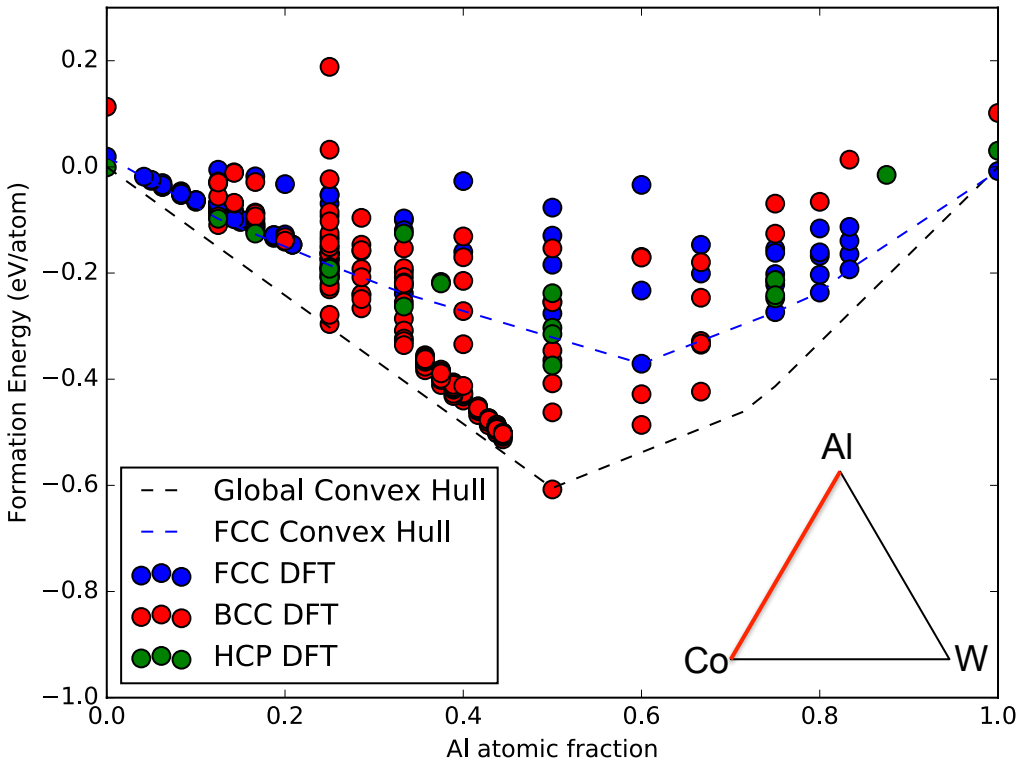

Figure 3.14: DFT formation energies used to fit the three cluster expansions for all three parent crystal structures along the Co-Al binary. The large number of red BCC configurations near the B2 CoAl composition represent orderings in which Co antisite defects are present.

3.6 Monte Carlo and Gibbs Free Energies

As with the pseudobinary cluster expansion, Monte Carlo simulations can be used to investigate thermodynamics at finite temperature, although this is now complicated by the need for multiple chemical potential terms. In this analysis, the Grand Canonical ensemble continues to be used, holding constant chemical potential, volume, and temperature while allowing their conjugate terms to vary. Very large 8 x 8 x 8 supercells were used for the FCC cluster expansion Monte Carlo simulations and were allowed to completely equilibrate given their input parameters. From the results of these Monte Carlo simulations, a series of integrations can be performed to find Gibbs free energy surfaces of the parent crystal structures as a function of temperature. The derivation for this Gibbs free energy follows. It is first convenient to use the thermodynamic beta rather than temperature:

$$\beta = \frac{1}{k_B T} \tag{3.6}$$

Where k_B is the Boltzmann constant and T is the temperature in Kelvin. A characteristic potential can then be defined as:

$$\phi = U - TS - \sum_N \mu_N N_N \tag{3.7}$$

In this equation, U is the internal energy, S is the entropy, μ_N is the chemical potential of a given species, and N_N is the number of atoms of a given species. This equation can be multiplied by β and integrated with respect to β for a given Monte Carlo heating or cooling run:

$$\int_{\beta_1}^{\beta_2} d(\phi\beta) = \int_{\beta_1}^{\beta_2} (\bar{U} - x_{Al}\tilde{\mu}_{Al} - x_W\tilde{\mu}_W) d\beta \tag{3.8}$$

The $\bar{U}$ term is a normalized internal energy, the x_N terms are compositions, and the $\tilde{\mu}_N$ terms are equivalent to $\mu_N - \mu_{Co}$. The entire integrand on the right side can be termed the potential energy, which is given as output in the CASM code. This allows for us to determine the characteristic potential, ϕ, as a function of temperature:

$$\phi(T_2) = \frac{\int_{\beta_1}^{\beta_2} < potential\ energy > d\beta + \phi(T_1)\beta_1}{\beta_2} \tag{3.9}$$

The $\phi(T_1)\beta_1$ term is a reference characteristic potential and is taken as the 0 K formation energy for heating runs or a reference state that corresponds to a completely disordered lattice for cooling runs. From here, it is straightforward to obtain an expression for the Gibbs free energy, G, as a function of temperature:

$$G(T_2) = \phi(T_2) + \sum_N \mu_N N_N \tag{3.10}$$

Having performed the necessary integration, Gibbs free energy surfaces can be generated for each of the three parent crystal structures. The high temperature (3400 K) Gibbs free energy surface for the FCC Monte Carlo results is shown in Figure 3.15. While experimentally this temperature would result in a complete liquid, it is nonetheless useful to start Monte Carlo cooling runs at this artificially high temperature as it results in complete disorder on the FCC lattice. Gaps in the FCC free energy surface at 3400 K are due to tiling errors in the Monte Carlo runs, as the actual surface at this temperature is continuous. This analysis again focuses on the Co-rich region and so the Al-rich and W-rich portions of composition space are neglected, though the surface is concave up as is expected.

As the simulations cool from this disordered elevated temperature, the Gibbs free energy surface loses its continuity as it discretizes into different ordered domains. The structures that appear are ordered variants on the parent crystal structure in question.

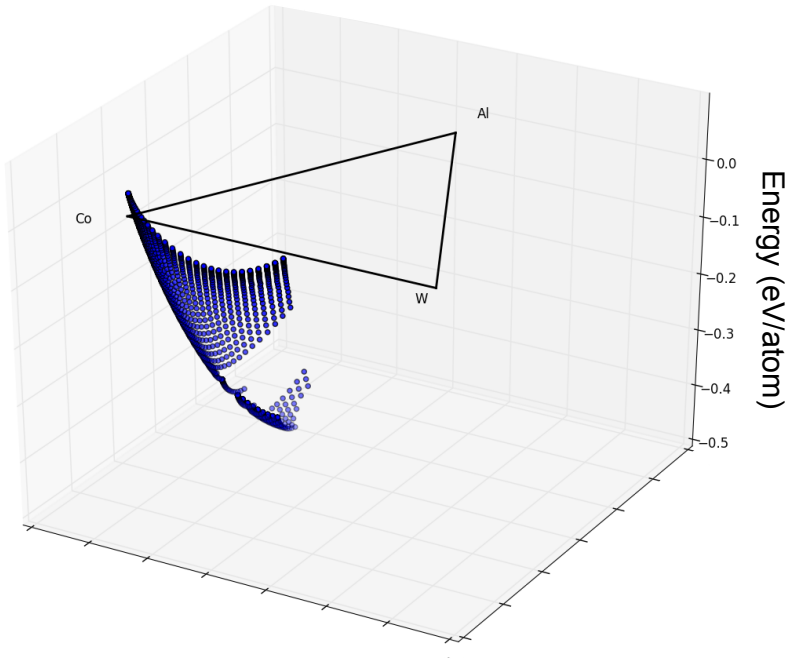

Figure 3.15: Gibbs free energy surface of the FCC crystal structure at 3400 K.

In this analysis, the stability of the $L1_2$ precipitate phase is of most concern at elevated temperature. As the structures cool, it is found that an ordered $L1_2$ phase does indeed appear, as is shown at 1200 K in Figure 3.16. This Co_3W $L1_2$ ordering has some solubility on the B sublattice, closely following the 75 at% pseudobinary line away from the Co-W binary axis.

Before phase diagrams are constructed, the other two parent crystal structure cluster expansions and their resulting Gibbs free energy surfaces must also be considered. At elevated temperature, both the BCC and HCP Gibbs free energy surfaces are continuous, corresponding to a lattice that is completely disordered. This is similar to the FCC Gibbs

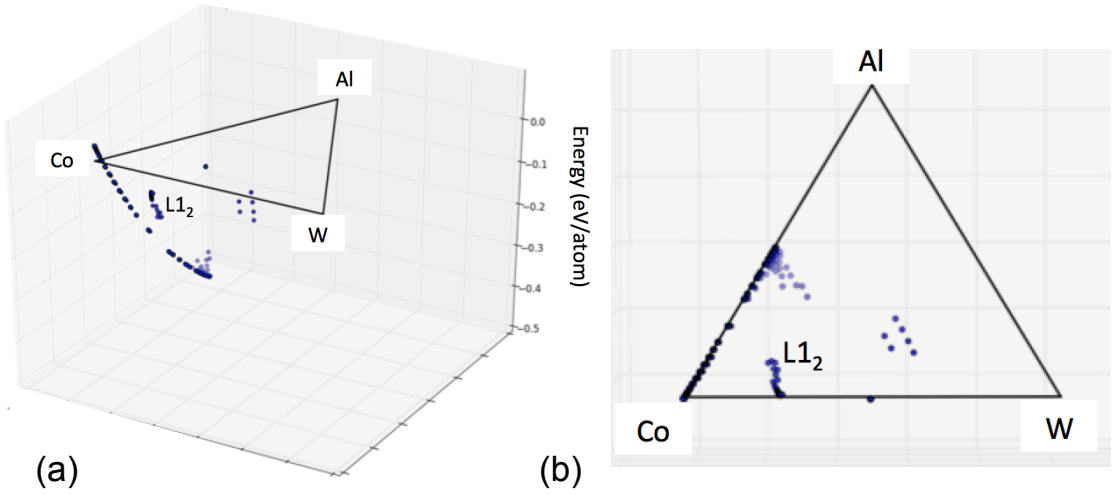

Figure 3.16: Gibbs free energy surfaces of the FCC crystal structure at 1200 K showing different ordered domains. Regularly arrayed W-rich points correspond to a disordered solid solution.

free energy surface seen in Figure 3.15. The Gibbs free energy plots at 1200 K for both the BCC and HCP structures are shown in Figure 3.17. In Figure 3.17(a) it is clear that relatively little solid solubility is observed in the B2 phase, which is somewhat surprising given what is observed experimentally. Nevertheless, the B2 structure is very energetically stable even at elevated temperature, as the vertex B2 point is at a global minimum for the entire Co-Al-W system. The Co_3W $D0_{19}$ structure is also apparent in Figure 3.17(b) and is very thermodynamically competitive with the $L1_2$ structure. This is intuitive as the structures only differ in their stacking sequence.

3.7 Phonon Effects

As with the pseudobinary analysis, it is important to consider the effects of vibrational free energy on the Co-Al-W system and incorporate that into the total Gibbs free energy expression. A plot of the free energy surface for FCC Co including vibrational effects is shown in Figure 3.18. This plot incorporates both the effects of temperature and volume

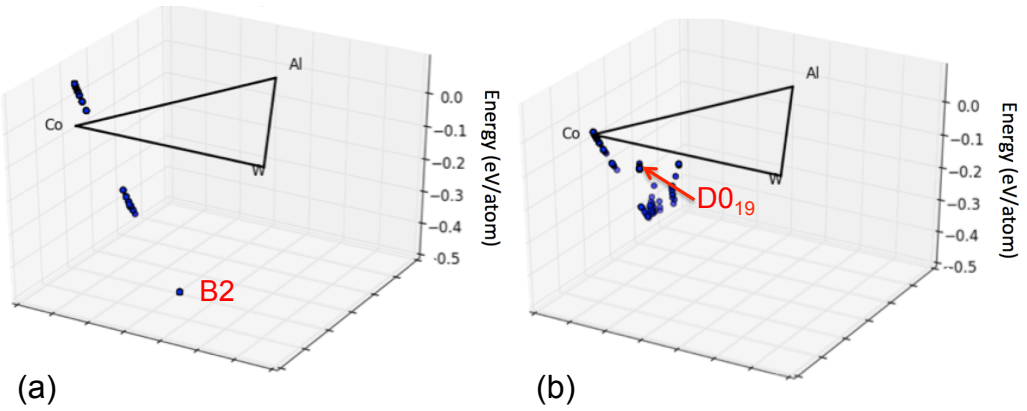

Figure 3.17: Gibbs free energy surfaces of the (a) BCC and (b) HCP crystal structures at 1200 K showing different ordered domains.

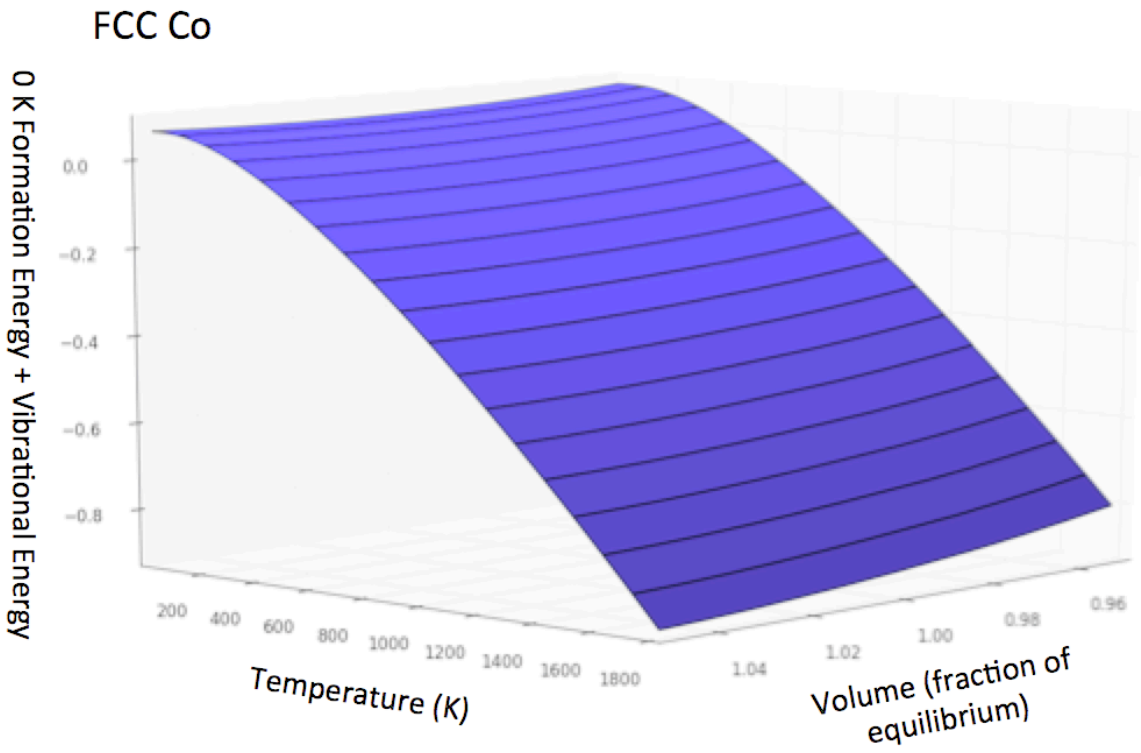

Figure 3.18: Free energy of FCC Co as a function of temperature and unit cell volume including the effects of vibrational free energy.

using the quasiharmonic approximation. The minimum free energy path as a function of temperature represents the vibrational free energy term used in generating subsequent

phase diagrams. As before, a planar interpolation was used for all FCC configurations using elemental Co, $L1_2$ Co_3Al, and $L1_2$ Co_3Al was used.

3.8 1200 K Ternary Phase Diagram

In order to construct a phase diagram at a temperature of interest, it is a useful exercise to layer each energetic term in order to determine the effect on the overall phase fields. 1200 K was chosen as a temperature of interest as it is close to the 900 °C temperature that the bulk of past research on the thermodynamics of the Co-Al-W system has been conducted. For each phase diagram, a convex hull construction is used on the combined FCC, BCC, and HCP Gibbs free energy surfaces, analogous to the common tangent construction used on Gibbs free energy curves in binary systems.

As a first step, the 1200 K Co-Al-W phase diagram can be considered without the effects of vibrational free energy. This applies a convex hull to the FCC Gibbs free energy surface shown in Figure 3.15 along with the BCC and HCP Gibbs free energy surfaces at 1200 K. This phase diagram is shown in Figure 3.19. The Co-rich portion of this diagram is considered most closely as it is where the experimental γ-γ' phase field is located. However, consistent with the pseudobinary results, an $L1_2$ phase field is not observed in this phase diagram without vibrational effects. Instead, for the region of interest there exists a three-phase field of elemental FCC Co, $D0_{19}$ Co_3W, and B2 CoAl. Somewhat surprisingly, relatively little solubility in the FCC Co and B2 CoAl phase fields is observed. From experiment, it is expected that the elemental Co phase field extend approximately 10 at% along the Co-Al binary axis and approximately 5 at% along the Co-W binary axis. As is apparent in Figure 3.19, only Al solid solubility in the FCC Co phase field is observed, and not to the degree observed experimentally. B2 CoAl observes similar limited solid solubility, although over 100 configurations containing Co antisite

defects were included in the underlying cluster expansion. This may be attributed to the very strong bonding that occurs in CoAl, effectively serving as a sharp vertex in the convex hull. It may also be due to the granularity of compositional space in these models, as increasing the resolution of the chemical potential space may better resolve solid solubility effects. In this phase diagram, $D0_{19}$ is essentially a line compound, which agrees with experiment.

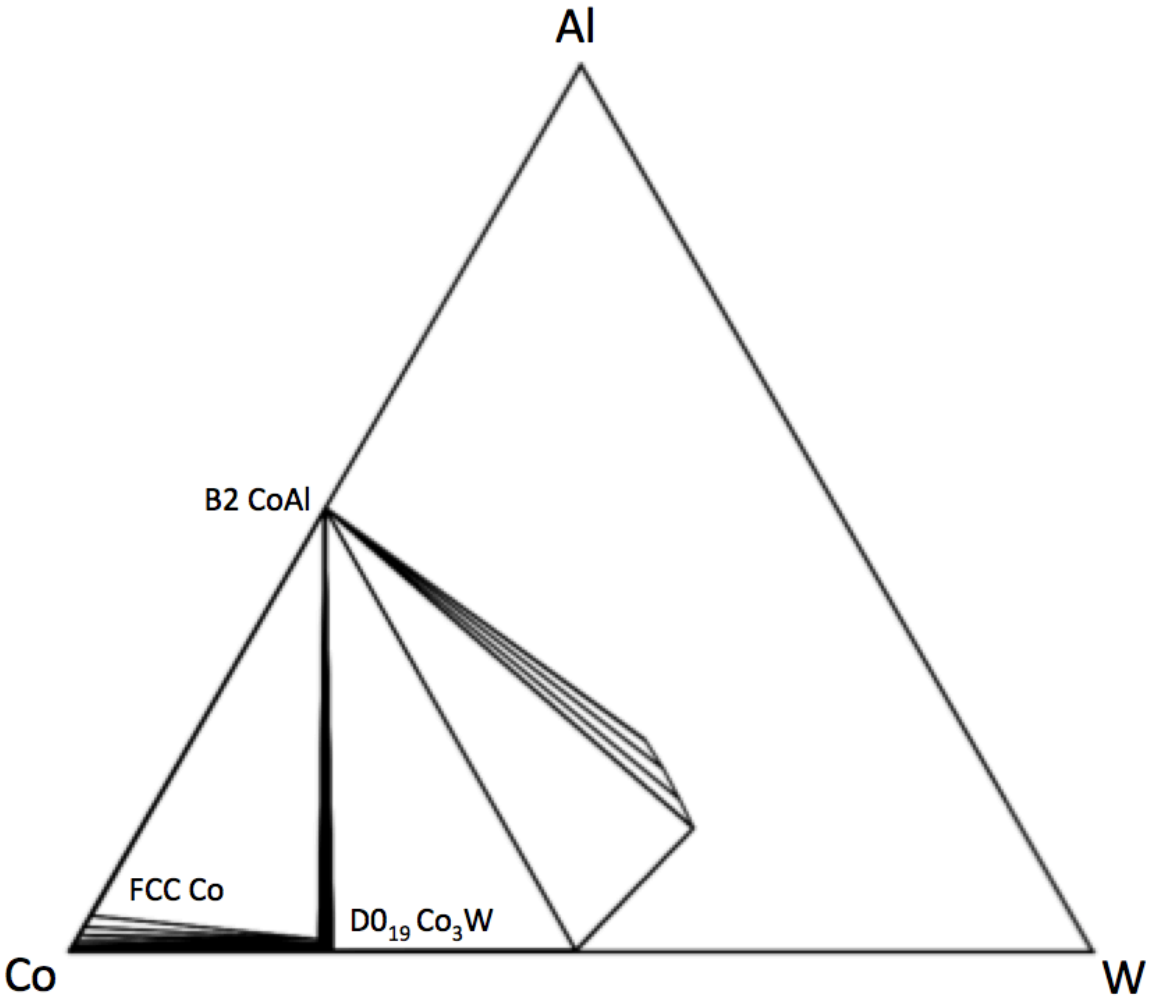

Figure 3.19: Phase diagram of the Co-Al-W system at 1200 K without the effects of vibrational free energy.

The next step in our layered analysis is to add in the effects of phonons on the overall Co-Al-W system. As before, a linear interpolation is used for the vibrational free energy

term on points that were not explicitly calculated. A phase diagram incorporating the effects of vibrational free energy on the system is shown in Figure 3.20. In this figure, the points comprising the Gibbs free energy surfaces have been overlaid as red circles onto the phase diagram delineated by the thin black lines. As is apparent in Figure 3.20, there are a number of $L1_2$ configurations extending away from the Co-W binary axis. However, these configurations do not pierce through the convex hull at 1200 K. While this would seem to contradict our earlier pseudobinary analysis, it should be noted that these configurations actually traverse a compositional path that is slightly poor in Co relative to the 75 at% pseudobinary line. The results are therefore not directly comparable and the pseudobinary line points need to be included in this analysis in order to draw full conclusions regarding the stability of the $L1_2$ phase.

To this end, points from our earlier pseudobinary analysis have been added to the full ternary cluster expansion. The resulting phase diagram is shown in Figure 3.21. In including these points, a very small γ' $L1_2$ phase field exists at $Co_3(Al_{0.2},W_{0.8})$ with a stability energy on the order of 10 meV/atom. This is consistent with what was observed in the pseudobinary analysis. It should be noted that the problems with solid solubility persist with the inclusion of vibrations. It is possible that the linear interpolation is too coarse to accurately capture the behavior at the interpolated points.

3.9 Summary

In this chapter, the cluster expansion formalism has been used to evaluate the thermodynamics of the Co-Al-W ternary system. Starting from 0 K formation energy calculations using DFT, the gap to high temperature thermodynamic properties has been bridged using Monte Carlo simulations and statistical mechanics. Our analysis began with evaluating the stability of the $L1_2$ precipitate phase along the 75 at% Co pseu-

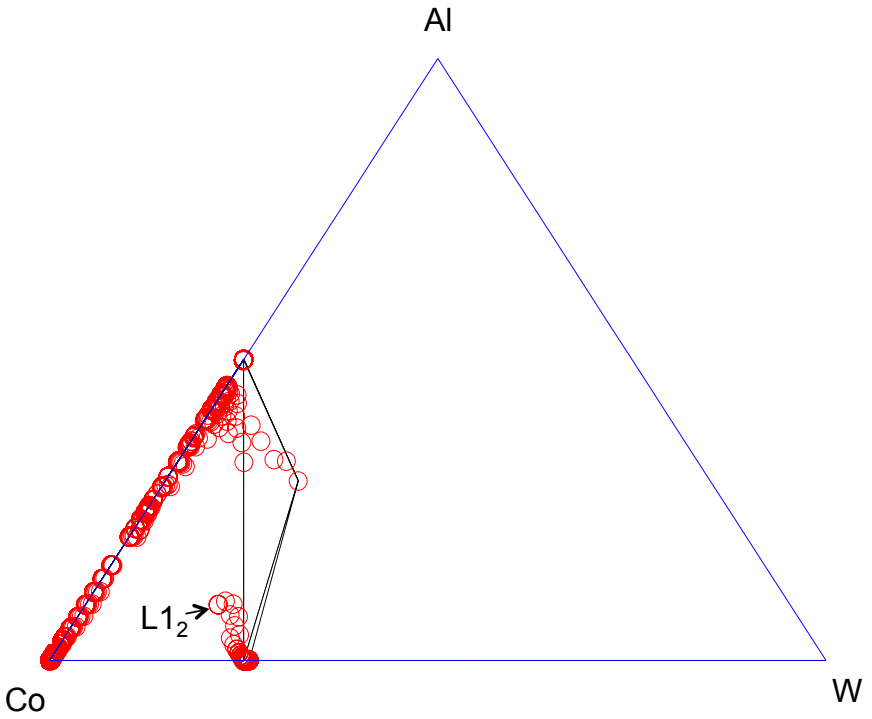

Figure 3.20: Phase diagram of the Co-Al-W system at 1200 K including the effects of vibrational free energy. Red circles indicate points on the free energy surfaces for the FCC, BCC, and HCP crystal structures.

dobinary line, where it was shown that vibrational free energy considerations have the strongest stabilizing effect on this compound. The $L1_2$ phase was found to be stable relative to a three-phase mixture of elemental Co, B2 CoAl, and $D0_{19}$ Co_3W at 600 °C. This initial work was extended to a full ternary analysis in order to incorporate the effects of solid solubility where it was found that a narrow $L1_2$ phase field exists at 1200 K.

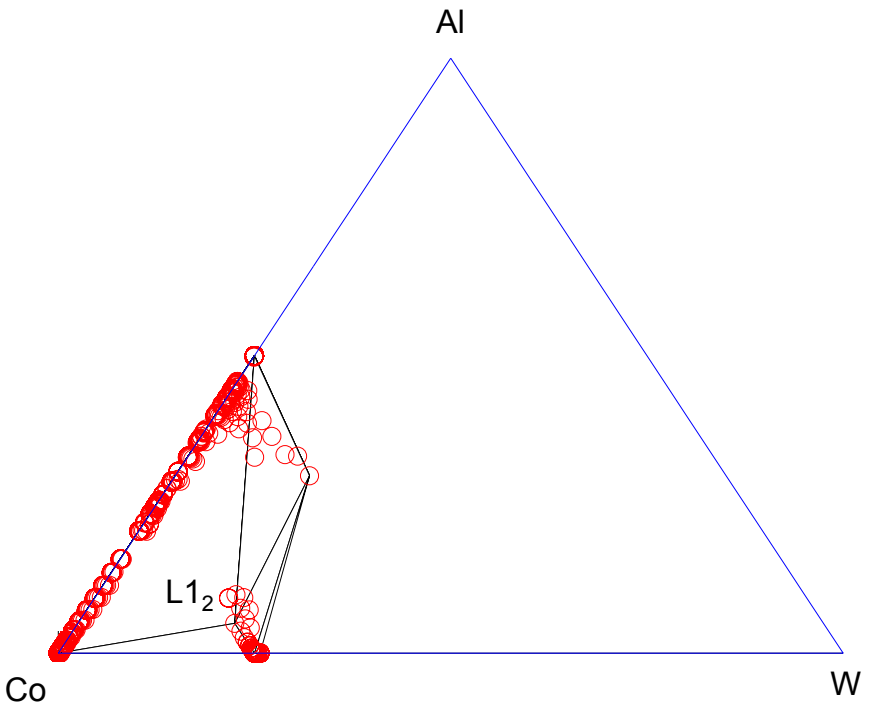

Figure 3.21: Phase diagram of the Co-Al-W system at 1200 K including the effects of vibrational free energy with past pseudobinary points. Red circles indicate points on the free energy surfaces for the FCC, BCC, and HCP crystal structures, as well as B sublattice W-rich pseudobinary points.

Chapter 4

Experimental Alloying

4.1 Introduction

In this chapter, first-principles DFT methods are combined with an experimental approach to characterize the creep behavior of quinary Co-base $L1_2$-containing superalloys at elevated temperature conditions. Temperature-dependent SISF energies have been modeled, combining 0 K formation energies with vibrational free energy calculations to assess deformation mechanisms at finite temperature. Two different Co-Al-W alloys, containing the maximum possible amount of DFT-identified d-block alloying additions, were identified and cast as single crystals via the Bridgman process. Creep tests have been performed at two primary testing conditions, one at 900 °C and the other at 982 °C. Transmission scanning electron microscopy (TSEM) was performed at 30 kV in a scanning electron microscope to rapidly characterize the defect substructures. The role of composition and temperature-dependent fault energies in the deformation process is addressed. Results in this chapter have substantially appeared in Rhein, Callahan, Murray, et al. [73].

4.2 Motivation

The 0 K normalized energies for both Co_3X SISFs and APBs are shown in Table 4.1. The ΔE_{SISF} and ΔE_{APB} are taken as the difference between the sheared and unsheared supercell structure. At 0 K, the energy for formation of APB defects is universally higher than for the formation of SISFs, indicating that at lower temperature we expect it to be relatively easier to shear the lattice into a locally hcp stacking sequence than to create an APB. This is intuitive, as large d-block alloying additions do not preferentially occupy nearest-neighbor lattice sites as they are required to in an APB defect.

The temperature-dependent normalized SISF energies calculated via DFT are shown in Figure 4.1. Normalized energies are used so the relative effect of each d-block alloying addition can be assessed. In the case of Co_3Nb and Co_3Ta, the normalized SISF energy increases with increasing temperature. Having significant quantities of Nb and Ta within the γ' precipitates will therefore make SISF formation more difficult with increasing temperature, suggesting that precipitates will become more difficult to shear and/or other deformation mechanisms such as APB formation may become relatively more favorable at higher operating temperatures. While the relative SISF energy of Co_3Ti decreases slightly with increasing temperature, it is still the most positive of the three alloying additions across the temperature range of interest, suggesting that its presence will make deformation via SISF formation more difficult as well. Physically, this suggests that in the case of Co3Ti, Co_3Nb and Co_3Ta that phonons will serve to stabilize the $L1_2$ structure. The SISF energies of the other structures considered, including Co_3Cr, Co_3Mo, and Co_3V were found to be universally negative and therefore these elements were not considered in the experimental portion of this work.

Quinary alloys containing significant amounts of Nb, Ta, and Ti are expected to have improved γ' thermomechanical stability as they will be more resistant to shear.

Vibrational effects serve to make it relatively more difficult for the Co_3Ta and Co_3Nb structures to shear from $L1_2$ to a local $D0_{19}$ structure. This information, combined with past studies, motivates the inclusion of Ta, Ti, and Nb in our experimental quinary alloys [74, 32].

Table 4.1: 0 K Normalized Formation Energies

Compound	$\Delta E_{SISF}/E_{L1_2}$	$\Delta E_{APB}/E_{L1_2}$
Co_3Ta	0.001	0.035
Co_3Ti	0.004	0.021
Co_3Nb	-0.001	0.003

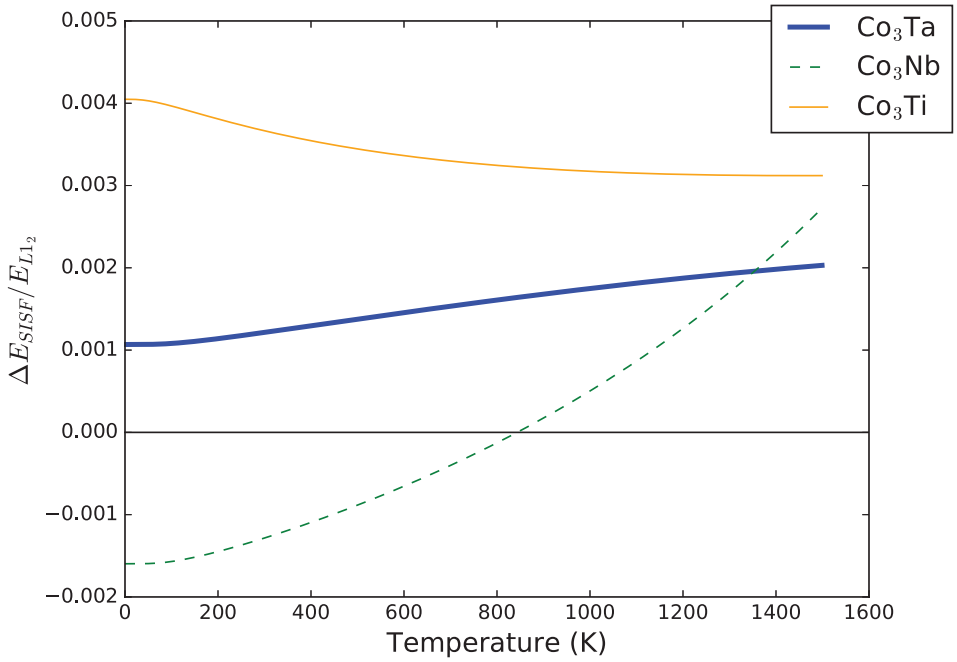

Figure 4.1: Normalized SISF energy calculated via DFT as a function of temperature for Co_3X structures, where X = Ta, Nb, Ti

4.3 Microstructures and Creep Behavior

After single crystal casting with a withdrawal rate of 200 mm/hr, a dendritic microstructure was observed in both the TaNb and TiNb compositions. The TaNb bars had an average deviation of 12° and the TiNb bars had an average deviation of 13° from <001>. The primary dendrite arm spacing was determine to be 230 and 360 μm for the TaNb and TiNb samples, respectively. EPMA revealed that, consistent with past observations of Co-base superalloys, there was very little elemental segregation during solidification [13]. EPMA line scans along the dendritic arm as seen in Figure 4.2 show relatively flat profiles, with a maximum standard deviation of 0.45 at% for any species within the TiNb specimen and 0.39 at% for the TaNb specimen. Upon heat treatment, small amounts of retained interdendritic phases were found in the TaNb sample while a two phase $\gamma - \gamma$' microstructure was observed in the TiNb alloy. The γ' area fractions in the TaNb and TiNb specimens were measured via backscattered electron microscopy as 68% and 83%, respectively. These measurements were obtained by applying the Yen threshold along with a despeckle filter in ImageJ on several micrographs containing over 1000 γ' precipitates [75, 76, 77]. Representative micrographs obtained via backscattered electron microscopy for the two specimens after heat treatment are shown in Figure 4.3. The average γ' cube edge lengths were measure as 124 and 235 nm for TaNb and TiNb, respectively. Differential thermal analysis measurements indicated that both alloy compositions had γ' solvus temperatures on the order of 1100 °C.

The creep curves of all conducted tests are shown in Figure 4.4. At 900 °C and 275 MPa, the observed minimum strain rate in both samples after the initial transient period was approximately 1×10^9 s^{-1} . At 982 °C and 248 MPa, the observed minimum strain rate after the initial transient period was on the order of 1×10^7 s^{-1} in both samples. The creep performance of the two compositions relative to established alloys is shown as

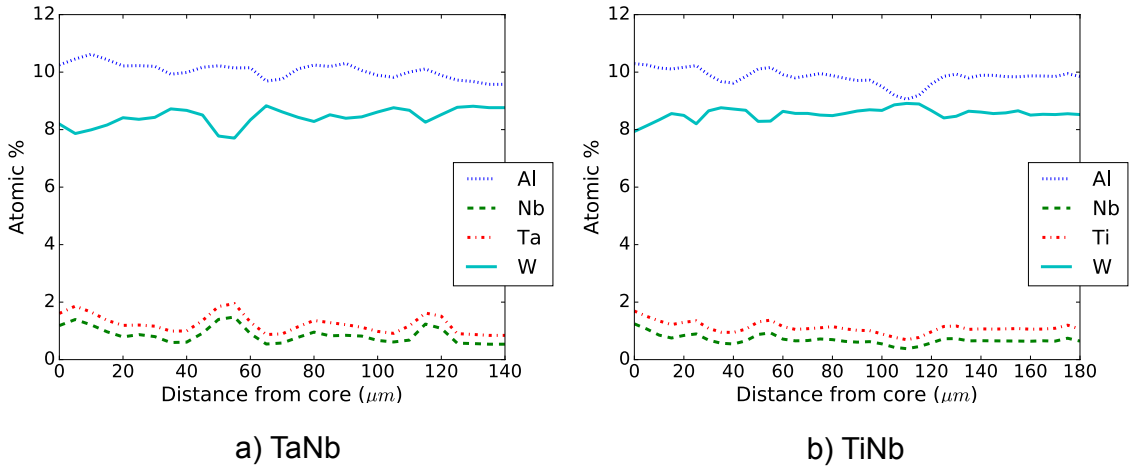

Figure 4.2: EPMA scans of the as-cast alloy solute compositions as a function of distance from dendritic core.

a Larson-Miller plot in Figure 4.5 [78, 79, 80, 81]. The overall creep performance until failure is comparable to first-generation Ni-base superalloys such as CMSX-2, consistent with previously measured Co-base superalloy creep performance [21].

4.4 Post-crept microscopy

TSEM micrographs of the post-crept TaNb microstructures are shown in Figure 4.6. At both sets of testing conditions, rafting was observed parallel to the loading direction, indicating a positive γ-γ' misfit consistent with past observations in Co-base superalloys [21, 82]. Notably, the dominant deformation mechanism responsible for precipitate shearing appears to be different between the two testing conditions. At the lower temperature and higher stress 900 °C and 275 MPa condition, precipitate shearing appears to be dominated by the formation of SISFs. In Figure 4.6(a), (c), and (e) there are a number of SISFs visible. As the amount of creep strain increases, the density of observed SISFs tends to increase, as demonstrated by Figures 4.6(a) and (c). Stacking faults are not observed at the higher temperature and lower stress 982 °C/248 MPa testing condition,

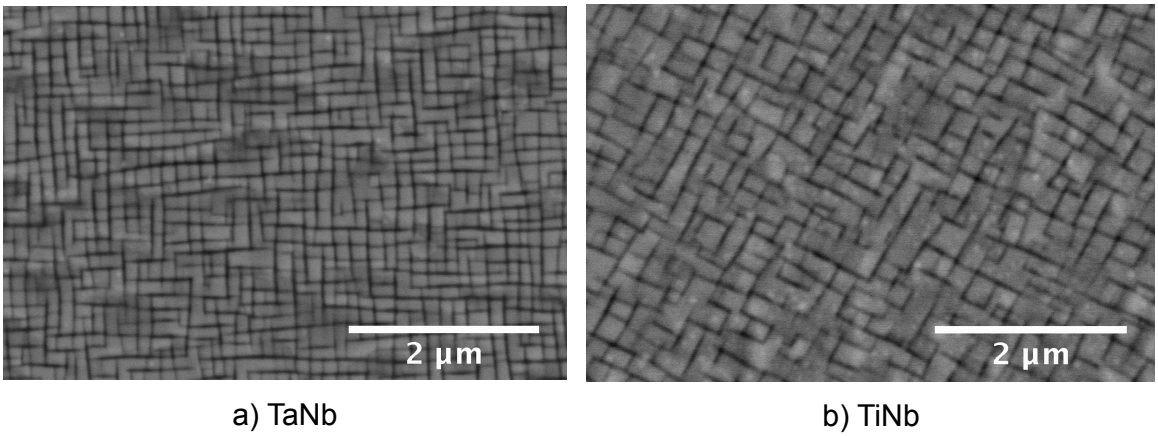

Figure 4.3: Backscattered electron micrographs of the heat treated alloys

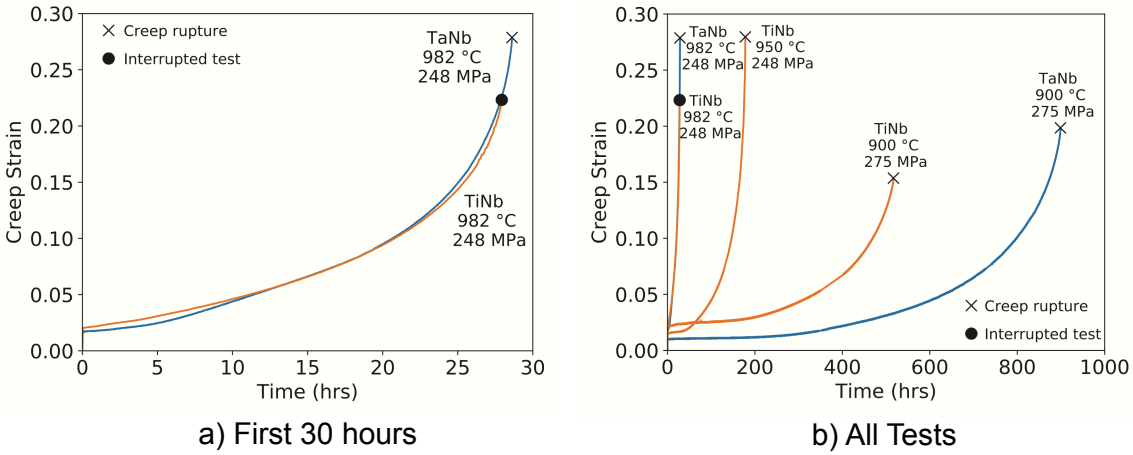

Figure 4.4: Creep curves for the TaNb and TiNb compositions during a) the first 30 hours of testing and b) for all testing conditions.

as seen in Figure 4.6(b), (d), and (f) where the dominant creep deformation mechanism appears to be mediated by an APB-forming mechanism.

Micrographs of the post-crept TiNb microstructures are shown in Figure 4.7. A similar transition in the dominant deformation mechanism responsible for precipitate shearing was observed between the two testing conditions. Stacking faults are observed in the lower temperature and higher stress 900 °C/275 MPa testing condition, as seen in Figure 4.7(a), (c), and (e). At the higher temperature and lower stress 982 °C/248 MPa

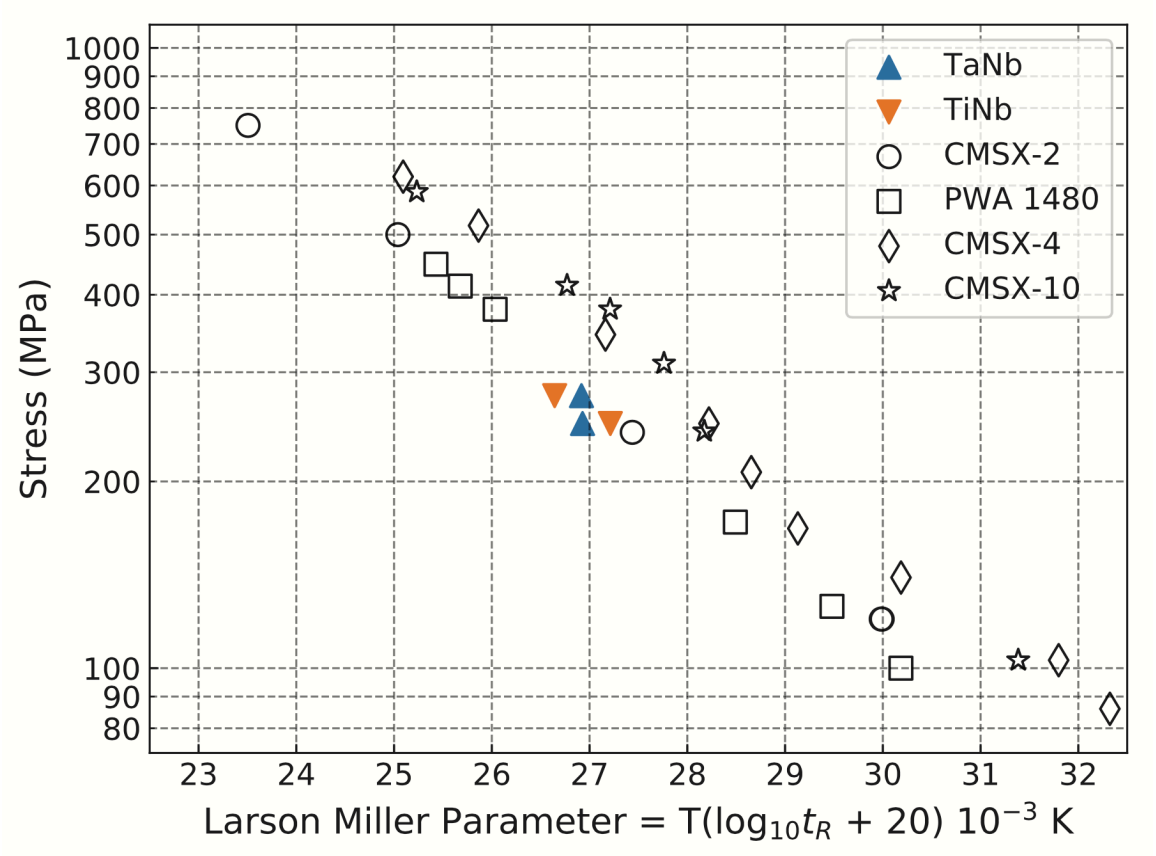

Figure 4.5: The Larson Miller Parameter for TaNb and TiNb compared to 1st-, 2nd-, and 3rd-generation Ni-base superalloys

testing condition, the SISFs are completely absent and the shearing of the precipitates only occurs by APB-mediated mechanisms. At the lower temperature, some faults exist as isolated loops within the γ' precipitates and are bounded by APBs (Figure 4.7(e)). Interestingly, Figure 4.7(b) shows stacking faults present post-rupture at the 950 °C/248 MPa testing condition, yet stacking faults were not observed in near-rupture specimens in the 982 °C/248 MPa testing condition in Figures 4.7(d) and (f). This seems to indicate that a cross-over in the dominant deformation mechanism occurs between 950 °C and 982 °C at this applied stress level.

Previous studies have shown that there is a compositional dependence on the dominant creep deformation mechanism in CoNi-base superalloys that transitions from SISF

shearing to APB-mediated shearing with increasing Ni content [83, 84]. The micrographs in Figure 4.6 suggest that in Co-base superalloys there is an additional thermomechanical dependence on the dominant deformation mechanism. With increasing temperature from 900 °C to 982 °C, it is apparent that APBs become more energetically favorable than SISFs.

In our past stuides of CoNi-base alloys, at the 900 °C/275 MPa testing condition we have examined the formation mechanisms individual SISFs bounded on both sides by APBs within the γ' precipitates [85]. Unlike the SISF formation observed in Ni-base superalloys, the $\frac{a}{6}\langle 112\rangle$ partial dislocation is not permanently pinned at the γ-γ' interface and instead shears through the precipitate phase as a trailing partial dislocation to the leading $\frac{a}{3}\langle 112\rangle$ partial:

$$\frac{a}{2}\langle 011\rangle + \frac{a}{2}\langle 101\rangle \rightarrow \frac{a}{2}\langle 112\rangle \rightarrow \frac{a}{3}\langle 112\rangle + SISF + \frac{a}{6}\langle 112\rangle + APB \tag{4.1}$$

In this reaction, the resulting leading $\frac{a}{3}\langle 112\rangle$ partial shears across the γ' precipitate and leaves an SISF in its wake. Once the trailing partial enters the γ' precipitate, it begins to transform the SISF into an APB. If the trailing partial is effectively pinned at the γ-γ' interface, no APB formation is expected. The leading partial shears through the entire precipitate, while the trailing partial begins to form a SISF loop embedded in the APB. While this looping process is occurring, the trailing partial also migrates toward the more energetically favorable $\{100\}$ planes, reducing the energy of the overall configuration. The trailing partial eventually closes by reaction with itself, leaving behind a complete loop surrounded by an APB with an embedded SISF. The fault configuration can extend over multiple precipitates, as has been shown in CoNi compositions [85].

These embedded SISF loops are the result of a force balance between the force that promotes expansion of the loop, F_E, and the force that promotes contraction of the loop,

F_C, as seen in Figure 4.8. The expansion force, F_E is the difference in energy between the APB and SISF configurations while the contraction force, F_C is the sum of the dislocation line tension and the resolved shear stress. When the loop is stable, these forces are in equilibrium:

$$F_C = F_E \tag{4.2}$$

$$Gb^2/R + \tau_r b = \gamma_{APB} - \gamma_{SISF} \tag{4.3}$$

In this expression, G is the shear modulus, b is the magnitude of the Burgers vector along the (111) APB slip plane, R is the critical radius of curvature of the SISF loop, and τ_r is the resolved shear stress. γ_{APB} and γ_{SISF} represent the energies of the APB and SISF, respectively. If we consider the 900 °C testing condition and take G=60 GPa, τ_r=129 MPa, R=60 nm, and b=0.145 nm, we can obtain a finite temperature value for the energy of the APB if the energy of the SISF is known [86]. Based on the above force balance, we expect the APB energies to be approximately 40 mJ/m^2 higher than the SISF energies at 900 °C in both of our compositions. As the formation energies of the Co_3X APBs are approximately 270 mJ/m^2 larger than the SISF formation energies at 0 K, this represents a significant decrease in the relative energy of APBs at elevated temperature. The ability to quantitatively assess the fault energy and temperature dependence of these shearing mechanisms provides a new path for the design of alloys with improved properties at high temperatures, where they are used in service.

In the alloys studied here there is appears to be a transition from the APB/SISF/APB shearing mechanism to shearing mechanisms that reveal APBs or APB-coupled superdislocations post-deformation as the temperature increases from 900 °C to 982 °C and beyond (Figures 4.6 and 4.7). At 0 K from DFT, we have found that the {111} APB energy exceeds that of SISF formation for Co_3Ta, Co_3Ti, and Co_3Nb. Several factors likely

contribute to the presence of isolated APBs at the elevated temperature condition. As temperature increases, SISF formation becomes increasingly difficult due to vibrational effects, as shown in Figure 4.1. The stability of the APB/SISF/APB structure observed at lower temperature is the result of a balance between the expansion and shrinkage forces on the dislocation loop surrounding the SISF. At high temperature, there is an increase in the driving force that acts toward shrinking the SISF arising from the relative decrease in APB energy.

There is increased diffusion at elevated temperature, which is a possible explanation for the presence of very few stacking faults at high temperature in these specimens. The presence of only APB-coupled dislocations at the elevated temperature condition may be the result of annihilation of previously-existing SISFs, or an indication that pairs of undissociated a/2<110> dislocations enter at the γ-γ' interface. We also expect segregation plays a strong role in decreasing the relative energy of APB formation. Past work has shown that heavy refractory elements, such as W and Ta, strongly partition to the γ' phase and SISFs [52, 87]. Because of this segregation, the local free energies near the faults are affected, driving the SISF and APB energies closer together. We expect our alloys, containing significant quantities of refractory additions, to exhibit similar segregation behavior, further lowering the relative energy of APB formation [88]. Further detailed TEM studies as a function of strain and temperature above 950 °C would be useful for further elucidation of the operative mechanisms.

Finally, it is interesting to note that the TaNb alloy displayed slightly lower minimum creep rates compared to the TiNb alloy for the two conditions investigated. The DFT calculations (Figure 4.1) suggest that the fault energies of these two alloys should be similar. The difference is also unlikely due to the volume fraction of precipitates, as the TiNb alloy had a slightly higher fraction. The lower creep rates may be due to the slower diffusion of Ta in the $L1_2$ phase, which would be expected due to size considerations;

diffusion data for these new systems would be useful in further guiding compositional design.

4.5 Summary

We have combined first-principles and an experimental approach to characterize the mechanical behavior of higher-order Co-base superalloys. The limits of solubility of Ti, Ta, and Nb in quinary Co-base $L1_2$ containing alloys have been examined experimentally and creep properties at 900 and 982 °C have been characterized. We have observed differences in deformation mechanism during creep between the two temperatures as well as with composition. At low temperature, deformation is dominated by the formation of SISFs while at the high temperature condition shearing of precipitates is dominated by the motion of APB-coupled dislocations through the precipitate. This has been shown to be consistent with first-principles DFT calculations, which demonstrate that SISF energy generally increases with increasing temperature.

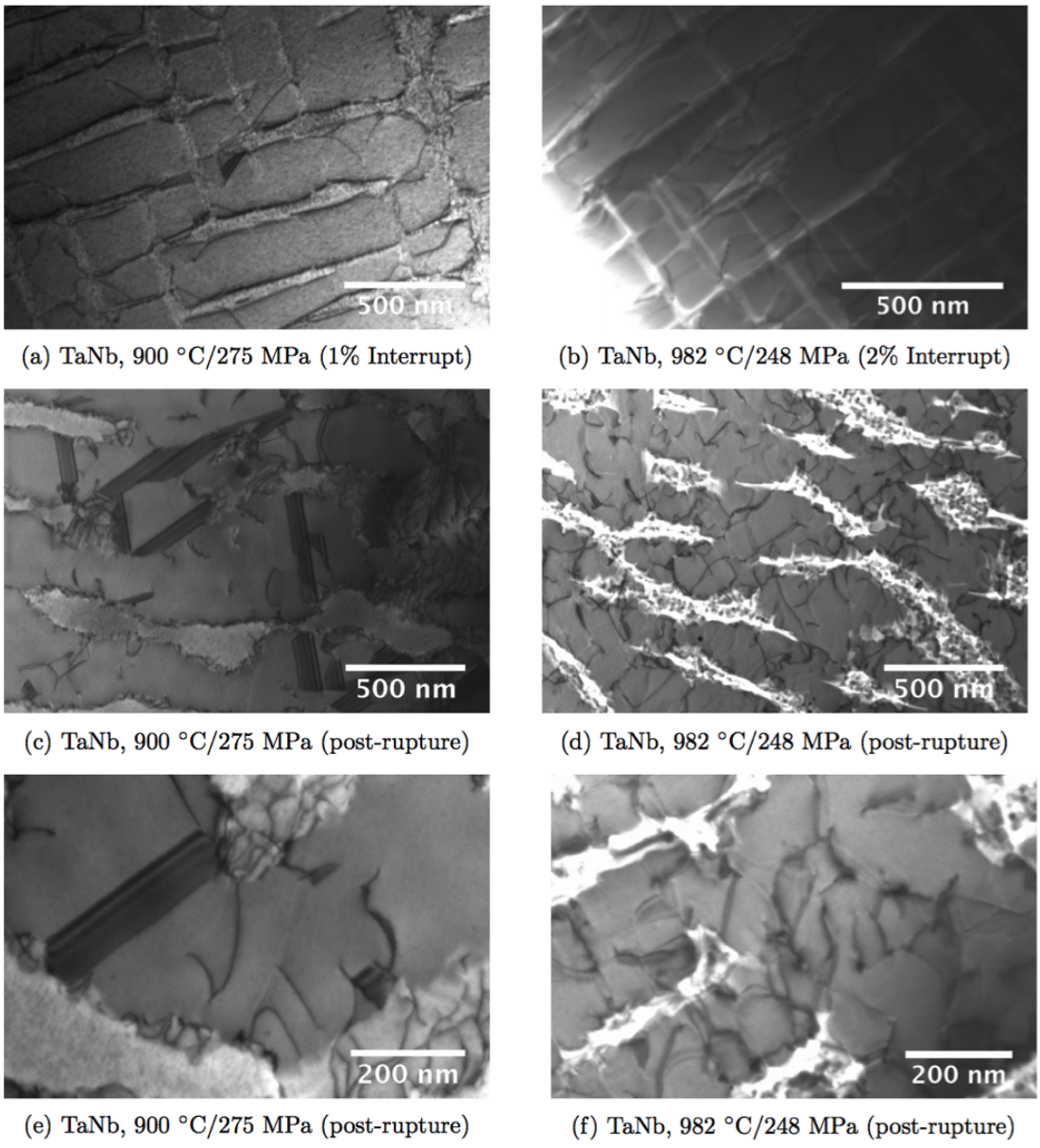

(a) TaNb, 900 °C/275 MPa (1% Interrupt)

(b) TaNb, 982 °C/248 MPa (2% Interrupt)

(c) TaNb, 900 °C/275 MPa (post-rupture)

(d) TaNb, 982 °C/248 MPa (post-rupture)

(e) TaNb, 900 °C/275 MPa (post-rupture)

(f) TaNb, 982 °C/248 MPa (post-rupture)

Figure 4.6: Bright field TSEM images of the TaNb microstructures after creep testing at (a, c, e) 900 °C and (b, d, f) 982 °C. Micrographs were acquired in both the (a, b) interrupted and (c-f) post-ruptured conditions.

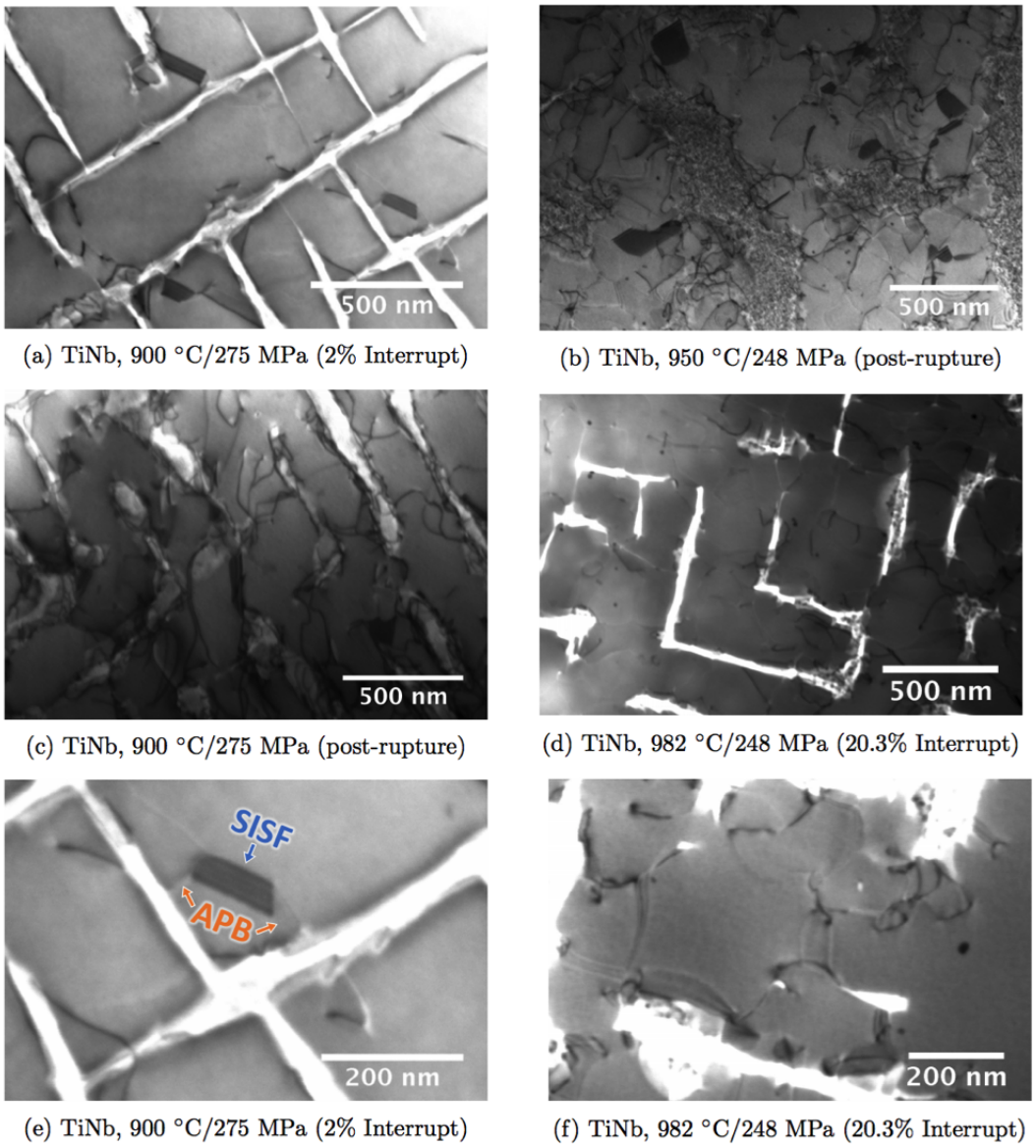

(a) TiNb, 900 °C/275 MPa (2% Interrupt)

(b) TiNb, 950 °C/248 MPa (post-rupture)

(c) TiNb, 900 °C/275 MPa (post-rupture)

(d) TiNb, 982 °C/248 MPa (20.3% Interrupt)

(e) TiNb, 900 °C/275 MPa (2% Interrupt)

(f) TiNb, 982 °C/248 MPa (20.3% Interrupt)

Figure 4.7: Bright field TSEM images of the TiNb microstructures after creep testing at (a, c, e) 900 °C, (b) 950 °C, and (d,f) 982 °C. Micrographs were acquired in both the (a, e) interrupted and (b,c,d,f) post-ruptured conditions.

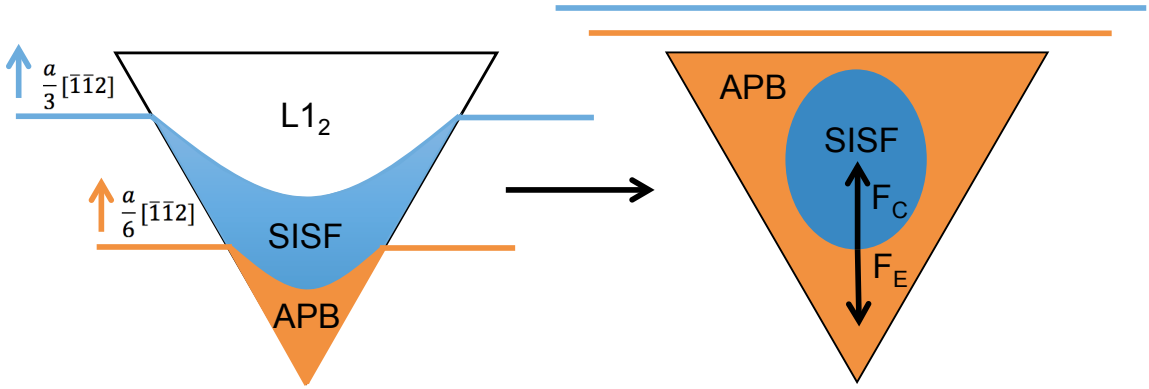

Figure 4.8: A schematic of the dislocation processes that produce the observed SISF loops embedded by an APB along the (111) plane. Expansive and contractive forces are indicated.

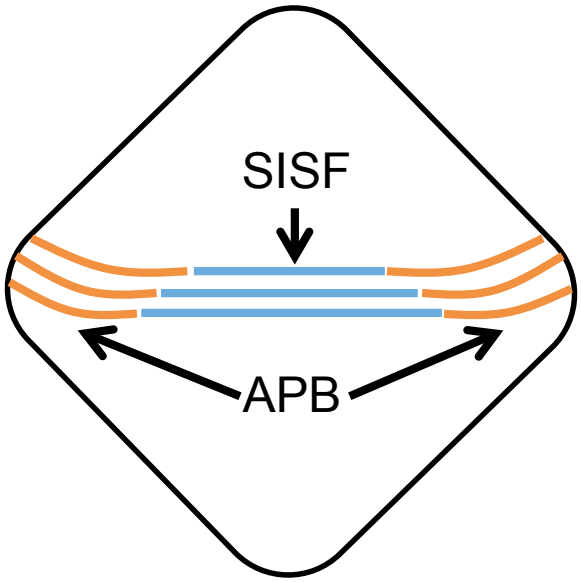

Figure 4.9: A schematic of the edge-on sheared precipitate, showing a SISF bounded by two APBs.

Chapter 5

$L1_2$ Faulting in Co- and CoNi-base alloys

5.1 Motivation

The addition of Ni to Co-base superalloys has been shown to widen the γ' phase field [89]. As composition changes from Co-base to Ni-base and the stability of the γ' phase increases, the mode of γ' shearing during creep changes significantly. In Ni-base superalloys, γ' shearing at temperatures greater than 850 °C is typically accommodated by pairs of a/2<110> type dislocations, resulting in the formation of an antiphase boundary (APB). In contrast, creep experiments performed on Co-base superalloys have shown that deformation in the γ' phase is accommodated by the formation of superlattice intrinsic or extrinsic stacking faults (SISFs or SESFs) [84]. At intermediate CoNi- compositions, a wide variety of deformation mechanisms are observed, including a/2<110>type APBs, APB-SISF-APB ribbons, and isolated SISF islands surrounded by APBs [83, 85]. These differences in deformation mechanism raise interesting questions for alloy design, as optimizing creep properties for a given composition is dependent on a variable deformation

mechanism. A better understanding of the energetics of these complex deformation mechanisms, starting from first principles, is required in order to increase the high-temperature strength of the γ' phase and improve alloy creep performance. The results in this chapter have been obtained in collaboration with the groups of Yunzhi Wang and Michael Mills at Ohio State University.

5.2 Gamma Surfaces

A generalized gamma surface (GSF) is a useful tool in determining the energetics of solid deformation. The GSF is defined as the excess of energy of the interface on a single side of the interface as it is translated relative to the lattice on the other side of the interface [90, 91]. Considering the (111) slip plane, the GSF is calculated by rigidly translating the atomic coordinates of the (111) plane on one side of the interface and then relaxing the positions of the atoms in the normal direction to slip plane to an energetic minimum. The excess energy from equilibrium can be measured at several distinct rigid translations to obtain an energy surface along the slip plane, including the energies of SISF and APB configurations in the case of the $L1_2$ phase.

The GSF energy surface at 0 K was determined for pure $L1_2$ Co_3Al and Co_3W structures from first-principles using DFT. The VASP package was employed for all calculations and the PBE generalized gradient approximation was used along with the PAW pseudopotential. In the calculation, 12 sequential (111) layers were generated for each supercell. Structures initially relaxed and then subsequent calculations were performed in which the topmost {111} plane was sheared along the <112> and <110> directions. The resultant formation energy was taken relative to the unsheared structure and fit using a polynomial to generate the GSF surface.

To simulate the GSF surface for mid-range compositions between Co_3Al and Co_3W,

an average of the two surfaces was generated. This assumes ideal mixing on the $L1_2$ B sublattice, which has been demonstrated using first-principles methods for the Co_3(Al,W) system [64]. Because of the symmetry breaking when the topmost (111) plane is sheared, it is not tractable to perform finite temperature vibrational calculations on these structures. In order to apply these calculations at finite temperature, the entire surface was scaled such that the APB energy matches the values determined by experimental TEM characterization. The average GSF at 0 K is shown in Figure 5.1. Fault energies from experiment are shown in Table 5.1.

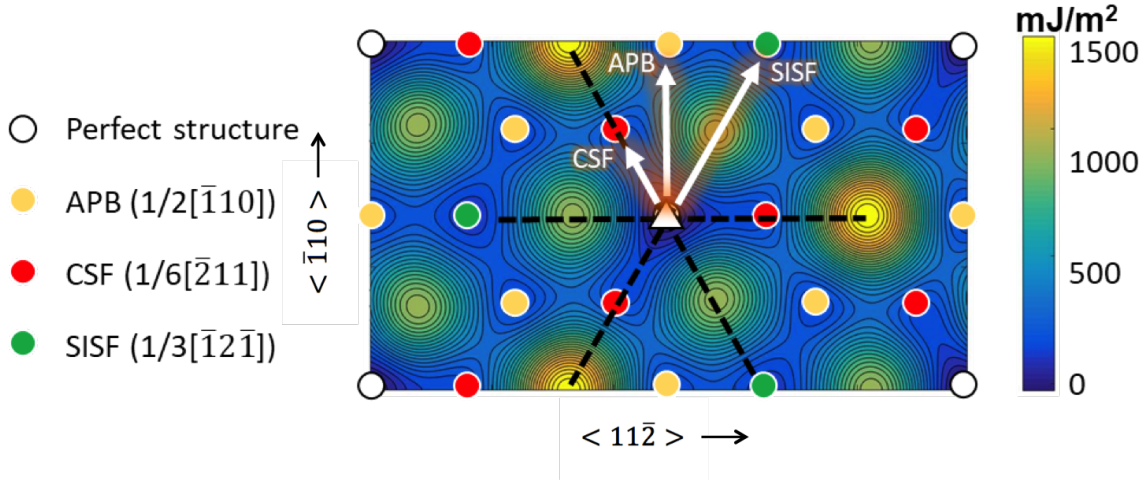

Figure 5.1: GSF energy surface for $Co_3(Al_{0.5},W_{0.5})$ at 0 K. Characteristic 3-fold rotational symmetry about the origin and mirror planes are indicated using black dashed lines.

Table 5.1: Fault Energies at 900 °C from experiment

	Co-based superalloys	CoNi-based superalloys
E_{APB} (mJ/m^2)	160	100
E_{SISF} (mJ/m^2)	130	80
E_{APB}/ E_{SISF}	1.23	1.25

5.3 Faulting behavior and Phase Field Modeling

In order to be useful in subsequent phase field calculations, a treatment of dislocation loops and their effect on the overall free energy of the system needs to be developed. For dislocation-based phase field models, dislocation loops are typically characterized by a set of non-conserved order parameters, η_p(r) [92, 93]. In this treatment, p represents the slip systems in question and r is a spatial coordinate, For an FCC crystal with 3-fold symmetry, displacement caused by dislocation glide can be expressed as:

$$\mathbf{b} = \eta_\mathbf{1}\mathbf{b_1} + \eta_\mathbf{2}\mathbf{b_2} + \eta_\mathbf{3}\mathbf{b_3} \tag{5.1}$$

In this expression for FCC crystals, b_1=a/2[10$\bar{1}$], b_2=a/2[$\bar{1}$10], and b_3=a/2[0$\bar{1}$1] while η_p corresponds to the magnitude of the inelastic displacement along the corresponding Burgers vector. Time evolution of these order parameters, η_p, is governed by a time-dependent Ginzburg-Landau equation:

$$\frac{\partial \eta_p}{\partial \tau} = -L_p \frac{\delta F}{\delta \eta_p} \tag{5.2}$$

In this expression, τ is a dimensionless time parameter, L is a mobility coefficient, and F represents the total free energy of the system. This total free energy is comprised of three components, a baseline crystalline energy $E^{crystal}$, a gradient energy E^{grad}, and an elastic energy E^{elast}:

$$F = E^{crystal} + E^{grad} + E^{elast} \tag{5.3}$$

Using this method, precipitate and dislocation local interactions control the dominant deformation mechanism without any additional assumptions. Dislocation dissociations and reactions are determined by the GSF surface. The GSF surfaces used in the phase

field simulations are shown in Figure 5.2 and are scaled with temperature using a Fourier series.

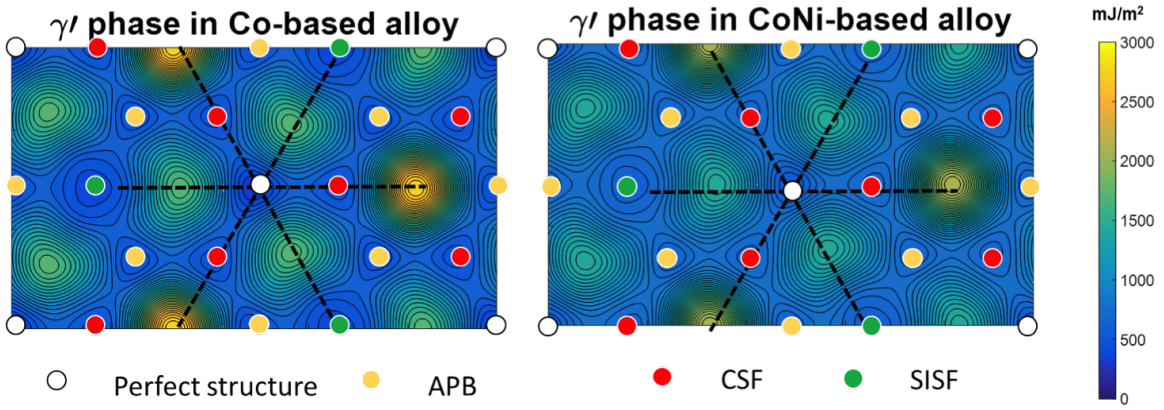

Figure 5.2: GSF energy surfaces for Co- and CoNi-base $L1_2$ phase used in the phase field simulations.

Two dislocation configurations, a single AB a/2<110> and a pair of AB+AC a/2<112> dislocations, were considered. For reference, a Thompson Tetrahedron indicating possible dislocations along the (111) plane is shown in Figure 5.3. Two different kinds of precipitate shapes were also considered, one spherical and the other cuboidal. On {111} planes, the spherical precipitates have a circular shape while the cuboidal precipitates have a triangular or hexagonal shape. A stress of 345 MPa was applied along the direction of the total Burgers vector in order to comport with past experiments [85]. The precipitates considered are 170 nm in diameter for the spherical particle, 204 nm in edge length for the triangular cross section, and 85 nm in edge length for the hexagonal cross section of the cuboidal particle.

The interaction of a single AB a/2<110> dislocation is shown in Figure 5.4. In the Co-base superalloy, the APB energy is relatively high in the $L1_2$ phase, causing the dislocation to loop around the precipitate without shearing. In the CoNi-base superalloy, the APB energy is considerably lower (Table 5.1). This results in the shear of the $L1_2$ phase, leaving behind an APB of the a/2<110> type.

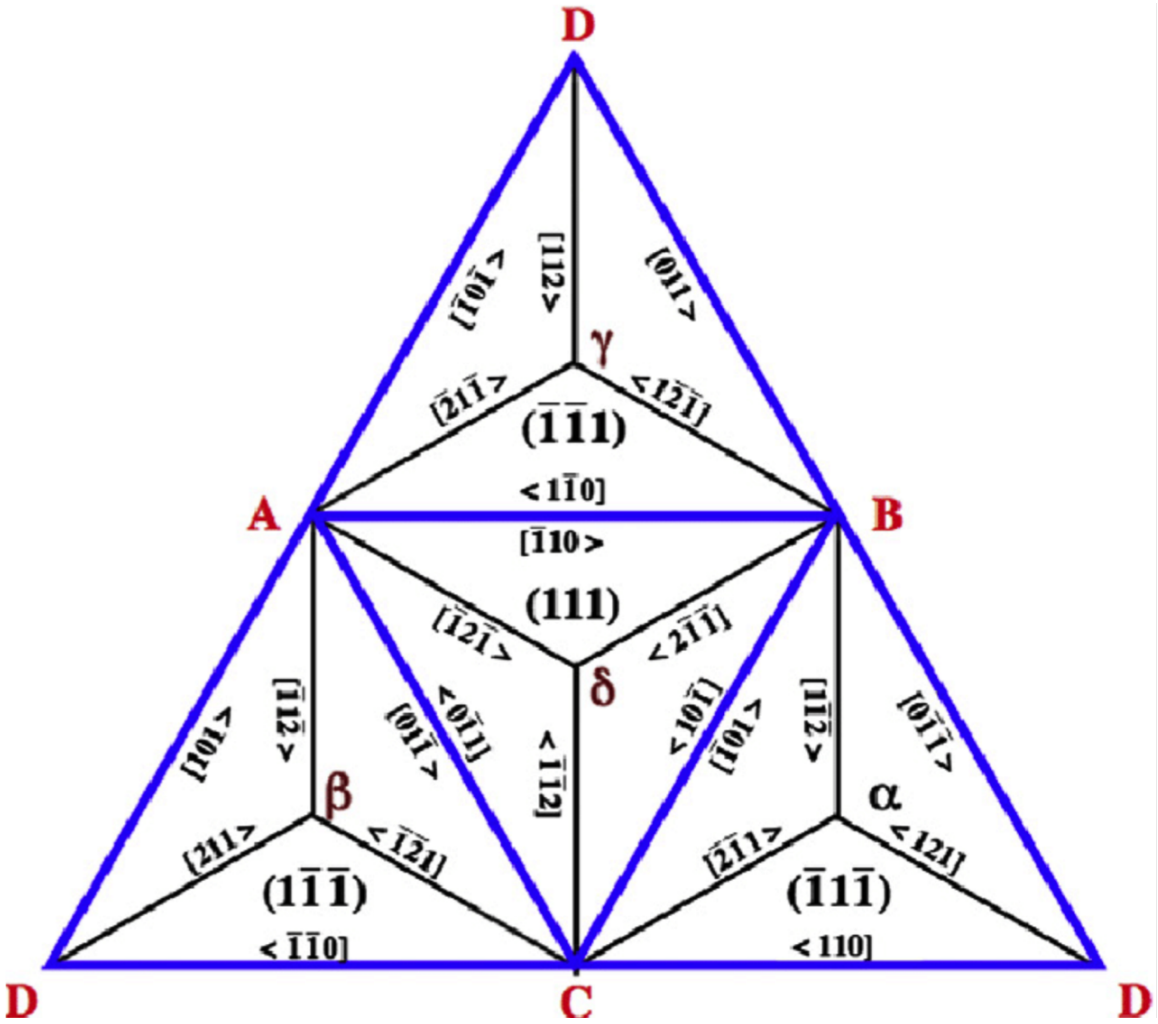

Figure 5.3: Reference Thompson Tetrahedron indicating possible dislocations and partials along the (111) plane. Reproduced from [94].

Figure 5.5 shows the interaction of a pair of AB+AC type dislocations (total Burgers vector a/2<112>) with a spherical $L1_2$ precipitate. In the case of the Co-base superalloy, the leading AB type dislocation stops at the interface between the matrix and precipitate until the trailing AC type dislocation pushes the leading dislocation into the $L1_2$ precipitate (Frame 2). At this point, an a/2<110>type dislocation is formed (Frame 3). Following this, the leading partial δC of the trailing AC type dislocation shears into the γ' precipitate while the trailing partial Aδ is pinned at the γ-γ' interface. This results in

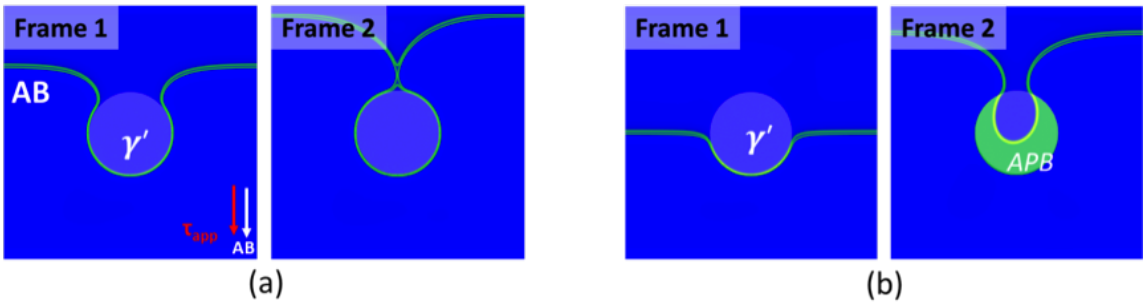

Figure 5.4: a/2[$\bar{1}$10] dislocation interacting with a spherical $L1_2$ precipitate in the (a) Co-base and (b) CoNi-base compositions.

the formation of an SISF within the precipitate (Frame 4).

For the CoNi-base composition, the leading AB dislocation is also arrested at the γ-γ' interface until the arrival of the trailing AC dislocation (Frame 1). The leading partial then cuts into the γ' precipitate, creating an APB of the a/2<110>type. Unlike the Co-base case, the trailing partial is not pinned at the interface and also shears through the precipitate. During this shearing event, an SISF exists between the two partials until both of them exit the precipitate, leaving behind an APB of the a/2<112>type within the precipitate in their wake. These deformation pathways are summarized in Figure 5.6.

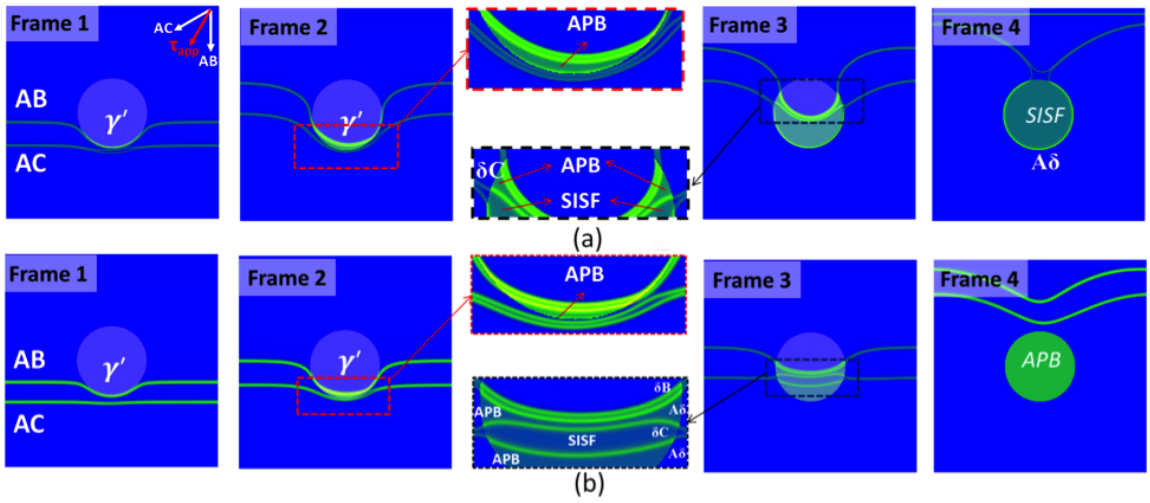

Figure 5.5: Interaction of a spherical $L1_2$ precipitate with a pair of AB+AC type dislocations in the (a) Co-base and (b) CoNi-base compositions.

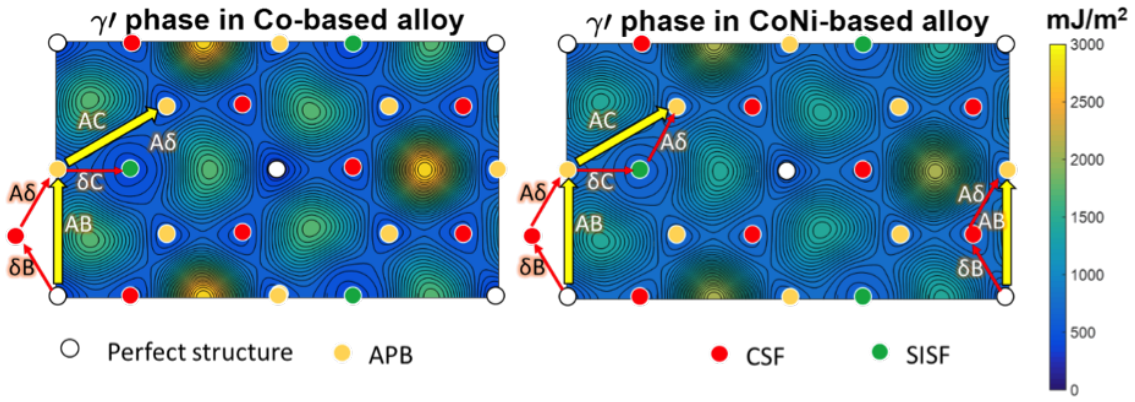

Figure 5.6: Deformation pathways inferred from the spherical precipitate phase field simulations.

In the spherical simulations, SISF formation is observed in the Co-base compositions while SISF ribbon formation is observed for the CoNi-base alloys, which is consistent with past experimental observations [83, 85]. Local curvature can also have an effect on the dominant deformation mechanism, and so phase field simulations in which the same set of AB-AC dislocations interact with a triangular and hexagonal cross-section were conducted, corresponding to cuboidal precipitates in three dimensions. The interaction of a single AB type dislocation with a triangular γ' precipitate cross-section is shown in Figure 5.7. Unlike the interaction with a spherical precipitate, the singular AB dislocation shears the precipitate resulting in the formation of an APB in both the Co- and CoNi-base cases. The interaction of a pair of AB + AC dislocations with both the triangular and hexagonal γ' precipitate cross-sections is shown in Figure 5.8. In all cases, an SISF ribbon is observed as both superpartial dislocations shear through the precipitate together, leaving behind an a/2<112>type APB. As there are key differences between these interactions and the interactions with the spherical particle, local curvature plays a role in determining the dominant deformation mechanism.

These simulations take in two independent variables, local curvature of the γ-γ' interface and fault energies. However, these two parameters alone cannot explain the

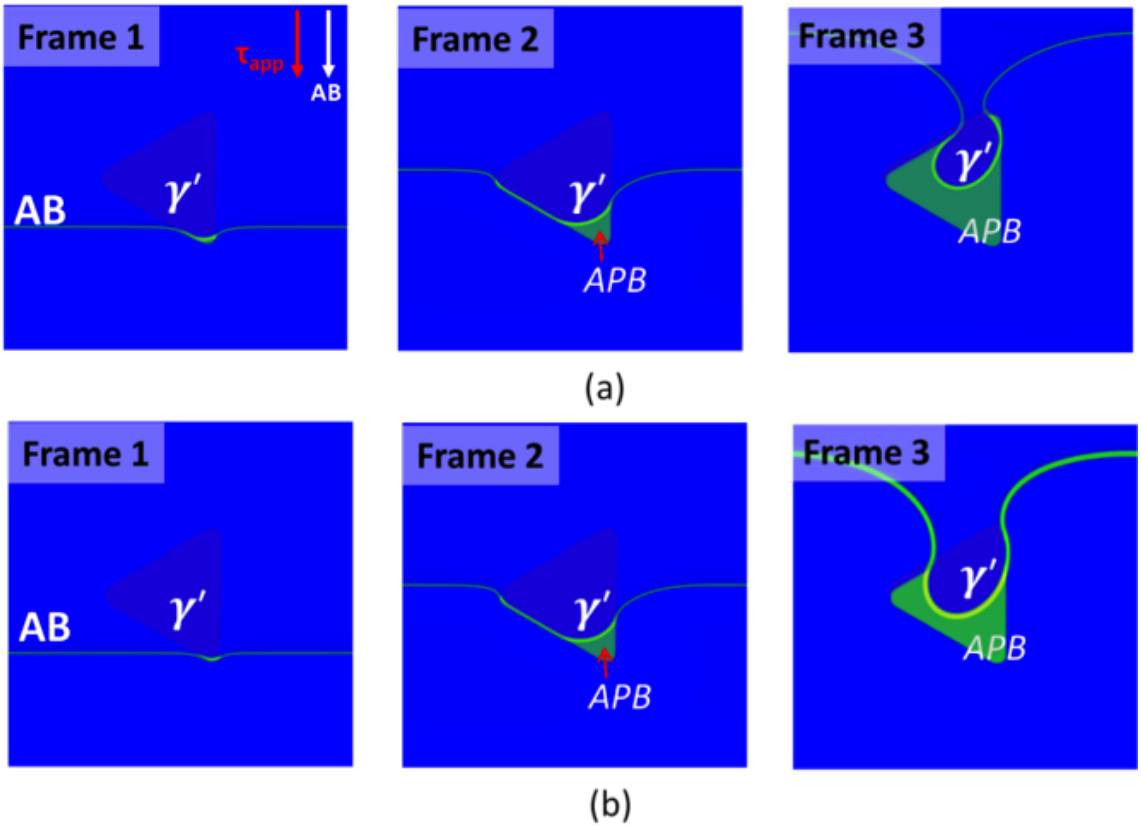

Figure 5.7: Interaction of an AB type dislocation with a cuboidal γ' precipitate with a triangular (111) cross section in a) Co-base superalloys and b) CoNi-base superalloys.

difference in deformation mechanism observed between the Co-base (SISF shearing) and CoNi-base (SISF ribbon formation) cases. Past work has asserted that a lower SISF formation energy will result in increased SISF formation as it is energetically easier for this fault to form [95]. This does not adequately explain the results in Figure 5.5, though. In isolation, SISF formation energy may dominate, but APB formation energy may also decrease with lower SISF formation energy. Although the SISF energy is lower in the CoNi composition, the APB energy is also lower, making the formation of an APB more favorable than in the Co-base case. It has also been hypothesized that the ratio of formation energy, E_{APB}/E_{SISF}, may be the controlling variable of observed deformation mechanism. This too does not adequately explain the behavior observed in Figure 5.5,

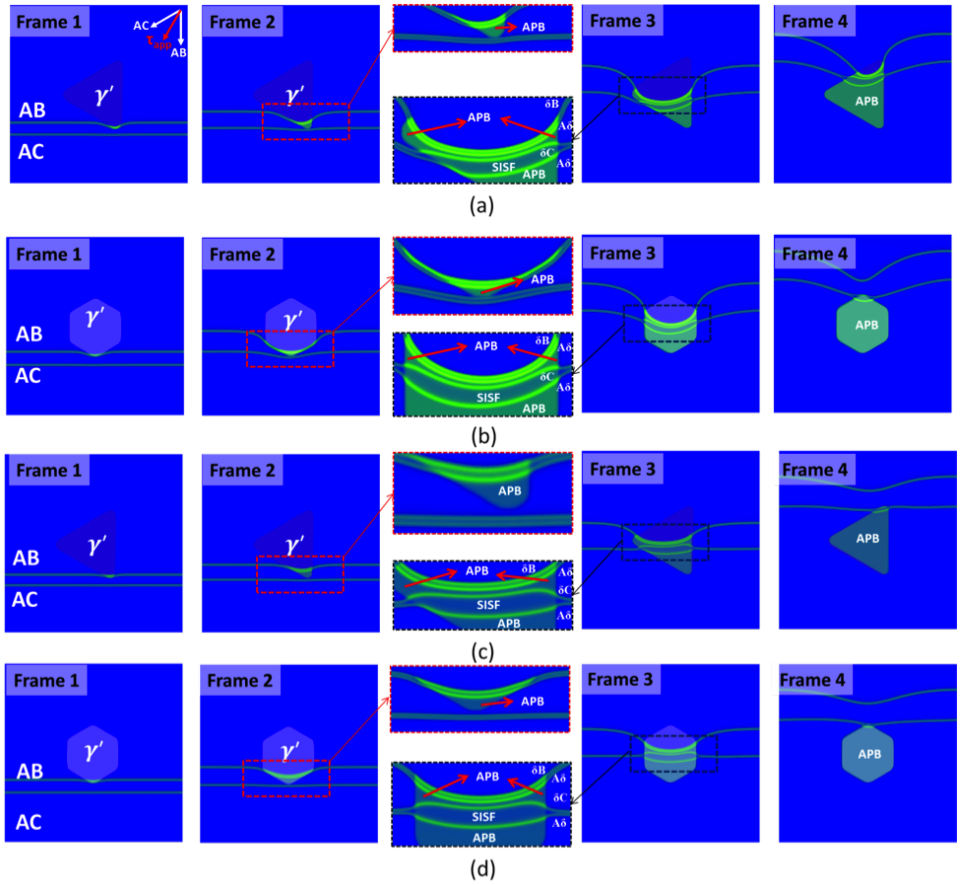

Figure 5.8: Interaction of a pair of AB +AC type dislocations with a cuboidal γ' precipitate along the 111. (a) Interaction with a Co-base triangular cross-section (b) Interaction with a Co-base hexagonal cross-section (c) Interaction with a CoNi-base triangular cross-section (d) Interaction with a CoNi-base hexagonal cross-section.

as the E_{APB}/E_{SISF} ratio is relatively comparable in the two compositions. Other factors may determine these observed differences in the phase field models.

Beyond the fault energy and local curvature, the details of the GSF energy landscape significantly affect the dominant deformation pathway. To study this effect, the GSF surface was scaled by a factor of k while all the fault energies were held constant. This corrects for some of the uncertainties in the *ab initio* calculations, allowing a more accurate representation of the energy landscape at finite temperature. Simulation results with two scaled energy surfaces (k=0.923 and k=1.08) for the AB+AC dislocation group

are shown in Figure 5.9, along with the unscaled case for comparative purposes. For the spherical particle, the γ' deformation mechanism changes from complete looping, to SISF shearing, to SISF ribbon formation as the scaling factor decreases. The local energy maxima on the GSF surface along the minimum energy path (MEP) constitute the dislocation line tension in the phase field model. A nearly linear relationship was found between the scaling factor k and the dislocation line tension by performing a series of phase field simulations with an AB dislocation loop of a given radius stabilized by applied stress, APB energy, and dislocation line tension. By scaling the GSF surface of the γ' phase, the dislocation line tension in the γ' phase is changed (the GSF of the γ phase is meanwhile kept constant). Because of this linear scaling, the effective difference in dislocation line tension between the two phases is increased with increasing k. This line tension difference contributes to the total critical resolved shear stress (CRSS) for dislocations to cut into the γ' phase. In these phase simulations, both the fault energy difference and the dislocation line tension difference are larger in the Co-base composition than in the CoNi-base composition. This suggests that the CRSS for the trailing partial Aδ in the AC partial dislocation is larger in the Co-base case. This may in part explain why SISFs are observed in Co-base superalloys while an SISF ribbon configuration is observed for the CoNi case. Co-base compositions are also elastically stiffer, which may also account for the observed SISFs.

5.4 Segregation Effects on Phase Field Model

Besides scaling the specific fault energies, it is also possible to scale the entire MEP by adjusting the Fourier coefficients used in fitting the GSF surface. This becomes useful in situations not easily handled by atomistic calculations, such as when there is significant elemental segregation or with multicomponent alloys. Segregation has recently

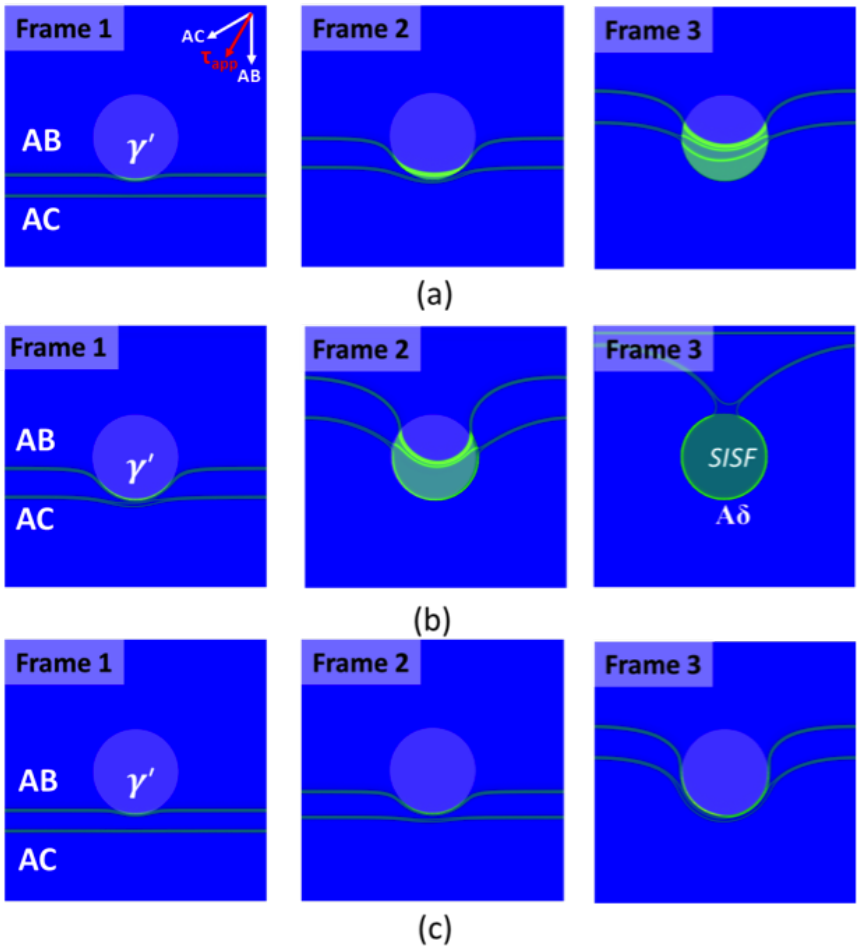

Figure 5.9: Interaction of an AB+AC dislocation group with a spherical γ' precipitate where (a) k = 0.923, (b) k = 1.00, and (c) k = 1.08. As k increases, the deformation pathway changes from an SISF ribbon, to SISF shearing, to complete looping.

been observed in Ni- [96, 97], Co- [98, 52], and CoNi-base [56] superalloys. The driving force for this segregation is a reduction in the overall SISF energy and has an impact on the dominant deformation pathway. Energies for the CoNi-base SISF and APB energies before and after segregation are shown in Table 5.2. Additional phase field simulations were conducted in which the GSF was scaled to match the dislocation line tension of the AB dislocation in the γ' phase. The interaction of an AB+AC dislocation group with a γ' precipitate in this segregated energy case is shown in Figure 5.10. Compared with prior phase field simulations, the width of the SISF region is larger. There is also

an intermediate APB/SISF/APB configuration in which an SISF island is surrounded by an APB region. This configuration has been observed in experiment in CoNi-base superalloys [85]. These simulations suggest that segregation may play a role in facilitating the formation of this fault configuration.

This APB/SISF/APB configuration is not stable, as any SISF island larger than the equilibrium size determined by the balance of the APB energy, SISF energy, dislocation line tension, and applied stress will expand and any SISF island smaller than this equilibrium size will shrink and annihilate. In the simulations in Figure 5.10, the SISF island eventually disappears, leaving behind an a/2<112> type APB in the precipitate. For this APB/SISF/APB configuration to be stable on the (111) plane, an additional force term needs to be present. If a friction stress term is included in the phase field simulations, it is possible to stabilize the APB/SISF/APB configuration. Figure 5.11 the results of such a phase field simulation in which a friction stress of 200 MPa is applied. This simulation assumes that an AB type dislocation has already sheared through the γ' precipitate and an AC type dislocation has looped around it. The loop of the leading partial δC of AC then shrinks so APB area is partially replaced by SISF area. Subsequently, the trailing partial Aδ cuts into the γ' particle from the corners due to the high local curvature. A stable SISF island embedded in an APB region results due to the balance of the dislocation line tension, SISF energy, APB energy, applied stress, and the friction stress. This friction stress could arise from lattice friction or a drag force associated with dislocation-solute interactions.

Table 5.2: Fault Energies in the CoNi composition before and after segregation

	Co-based superalloys	CoNi-based superalloys
E_{APB} (mJ/m^2)	100	60
E_{SISF} (mJ/m^2)	80	20
E_{APB}/ E_{SISF}	1.25	3

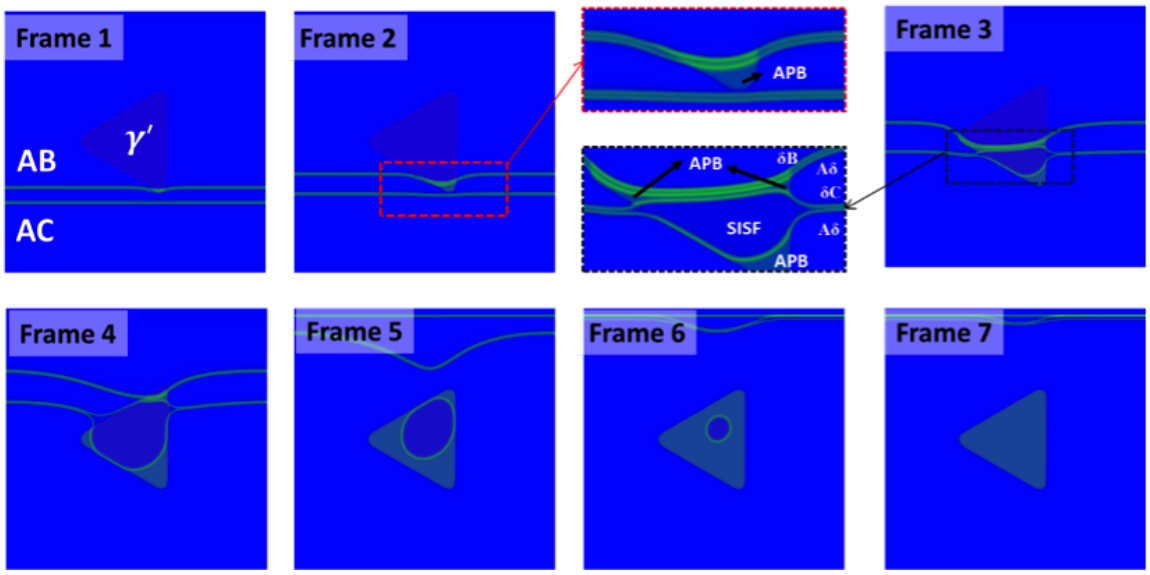

Figure 5.10: Interaction of an AB+AC dislocation group with a <111> cross section of a cuboidal γ' precipitate using the segregated energies in Table 5.2.

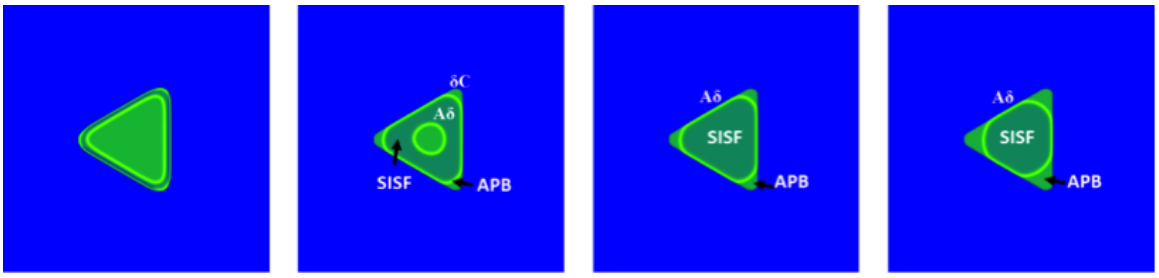

Figure 5.11: Stabilization of the APB/SISF/APB configuration in the CoNi-base superalloy with a friction stress term.

5.5 Segregation in Co_3(Al,W) Superalloys: Experimental Observations and Thermodynamic Driving Forces

Solute segregation at defects, faults, and interfaces has a significant effect on materials properties. Although this phenomenon has been well characterized in a number of metallic alloy systems that exhibit faulting behavior, it has not been until recently that it has been incorporated in material design. A full thermodynamic framework is available

to analyze the driving forces behind solute segregation to faults [56, 53, 54, 55, 23]. As these faults can be only a few atomic layers in thickness, it is experimentally difficult to determine the changes in local composition. In the following section, two independent experimental methods for determining segregation will be presented along with a new underlying thermodynamic framework from first-principles. Until recently, such a thermodynamic assessment has not been possible and the results presented here represent the first time such calculations have been performed.

A thorough understanding of the driving forces behind solute segregation at defects is complicated by a number of factors, including difficulties in experimentally measuring segregation, a lack of accurate thermodynamic properties, and few model materials systems that are easily examined both experimentally and via simulation. The Co-Al-W system is particularly well-suited for quantitative analysis of segregation at stacking faults. When small amounts of Ta are incorporated into the baseline ternary, a third Co_3W $D0_{19}$ phase forms during high temperature annealing in addition to the γ and γ' phases. This phase is ordered and hexagonally close-packed. When subjected to high-temperature creep, SISFs readily form in the γ' phase. Locally, these SISFs share the same crystal structure as the equilibrium $D0_{19}$ phase, allowing for direct comparison in composition of the nanoscale SISFs and the bulk Co_3W phase. Because the work presented here deals with single crystals, the nanoscale SISFs and the equilibrium $D0_{19}$ phase exist in the same thermodynamic reservoir and experience the same chemical potential and local stress states. In addition to this, the γ' $L1_2$ phase, the $D0_{19}$ phase, and the SISF compositions are all about 75 at% Co which allows for treatment of all these co-existing phases as pseudobinary compounds. This makes first-principles thermodynamic calculations considerably easier.

STEM analysis of the postcrept Co-2Ta specimen revealed SISFs on all four {111} planes. The SISFs form as a result of glide of Shockley superpartial dislocations with

b = a/3<112> [99]. The superpartial dislocations themselves form from the reaction of two matrix dislocations of type b = a/2<101> and a/2<011>:

$$\frac{a}{2}\langle 101\rangle + \frac{a}{2}\langle 011\rangle \rightarrow \frac{a}{3}\langle 112\rangle + SISF + \frac{a}{6}\langle 112\rangle \tag{5.4}$$

TEM samples were extracted from the bulk via focused ion beam and scanning electron microscope (FIB-SEM) so that the specimen normal was parallel to the [110] direction. An overview of the region of interest is shown in Figure 5.12.

High-resolution STEM high-angle annular dark-field (HAADF) imaging revealed a $D0_{19}$ lath coherently embedded within a γ' precipitate. This is shown in both Figure 5.12b) and Figure 5.13a). A SISF within the γ' phase was located parallel to the lath, as shown in Figure 5.13a). Fourier transforms of the STEM images revealed superlattice reflections consistent with a $D0_{19}$ structure for both the Co_3W lath and the SISF.

Energy-dispersive x-ray spectroscopy (EDS) line scans were taken across the image in Fig 5.13a) revealed an enrichment in W and Ta and a decrease in Co and Al in both the lath and fault. This agreed with vertically integrated line scans of the HAADF image, which also had an increase in image intensity for both the Co_3W lath and the SISF relative to the γ' phase. This is expected in the HAADF image if an area is enriched in relatively heavier elements, as image intensity has been shown to scale as the average Z to the 1.7-2 power [100].

Evidence of Al depletion at planar phases was clearly observed in the atom probe tomography (APT) reconstructed Al atom map shown in Figure 5.13b). However, only slight variations in Co, W, and Ta were readily apparent in the atom maps. The 1-dimensional line profiles across the normal of the planar phases revealed segregation of W and Ta to the planar phases and a depletion of Co and Al. The profile used a fix bin width of 0.15 nm and the moving average of two consecutive bins was used in order to

reduce scatter. This averaging did not change the total integrated excess W + Ta signal across the fault by more than 1 at%. The observed segregation behavior between the two phases observed from APT is in agreement with the high-resolution EDS results. The maximum W + Ta composition found in the faulted region was determined to be 18.9 and 21 at% via the STEM EDS and APT analyses, respectively.

Determining compositions via TEM EDS analysis can be influenced by thermally scattered electrons whose contributions are affected by a number of factors, including atomic species present, sample thickness, and crystal orientation [101, 102]. Because of these effects, the signal from each element is delocalized, as shown in Figure 5.13a). However, even when additional calculations are performed in which beam delocalization is accounted for, there is only a small change in total solute concentration from 18.9 to 19.5 at% within the SISF. Most current work has focused on delocalization effects within oxide materials and so how much delocalization affects the EDS signal in metallic specimens is not as well understood. Similar issues exist with APT measurements, although simulations have shown that these delocalization artifacts should not significantly degrade composition measurements [103]. The results here demonstrate a size dependence on the equilibrium composition within the faults and nanophases.

Without the high-resolution STEM information on the local structure, the type of defects in the APT speciment could not be determined. The thicker middle planar phase in the APT reconstruction exhibited similar segregation behavior to the Co_3W lath from the STEM EDS analysis but was of considerably smaller thickness. Because of this difference in thickness, it is unclear whether this phase is a thin Co_3W or instead a superlattice extrinsic stacking fault that is five atomic layers of the $D0_{24}$ structure. This $D0_{24}$ structure has been shown to exhibit similar segregation characteristics to SISFs [104]. The differences in composition between the SISF and Co_3W-like phase in the APT results reveals that, despite exhibiting an identical parent crystal structure, the

equilibrium concentration of W+Ta solute at the SISFs is significantly less than the concentration in the equilibrated Co_3W-type phase. These differences in composition cannot be due to differences in the chemical reservoir as both exist in the identical stress state and possess the same thermodynamic boundary conditions. The close agreement between the STEM and APT profiles further suggests that these results are not strongly influenced by technique artifacts. Therefore first principles modeling was pursued in order to examine the physical origins of the tendency for segregation and the driving forces for the transformation from $L1_2$ to $D0_{19}$.

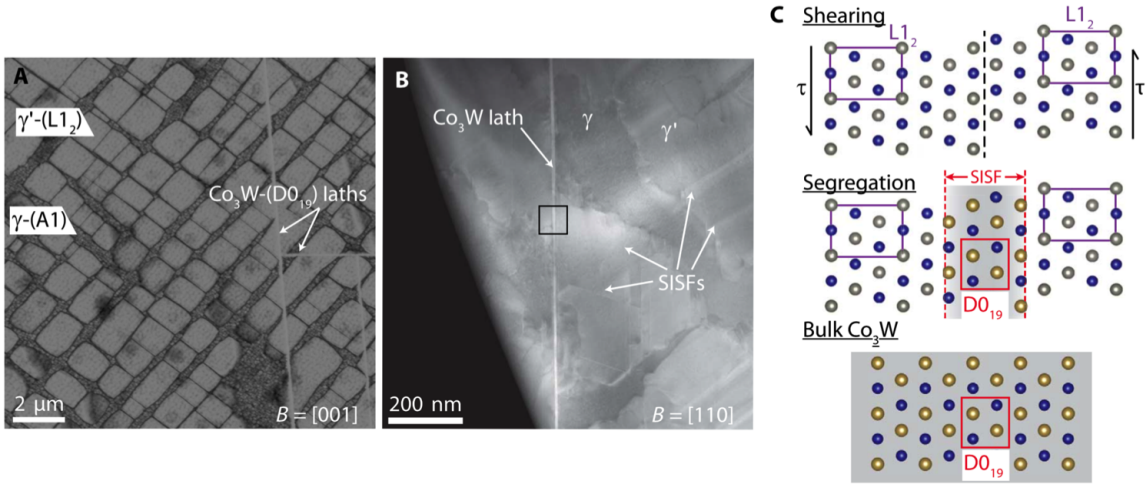

Figure 5.12: a) SEM image of the precipitate and matrix microstructure with Co_3W laths. b) STEM image of the deformed microstructure with a Co_3W lath crossing a γ' precipitate. c) Schematic of the shearing sequence that results in the formation of an SISF in a γ' precipitate. The γ' precipitates first shear and then segregation can occur which draws the composition of the precipitate closer to that of the $D0_{19}$ lath.

5.6 Modeling of Segregation in Co_3(Al,W) Superalloys

Multiphase equilibrium in materials is determined by the equality of chemical potentials of the mobile species. This equilibrium criterion is equivalent to the common tangent

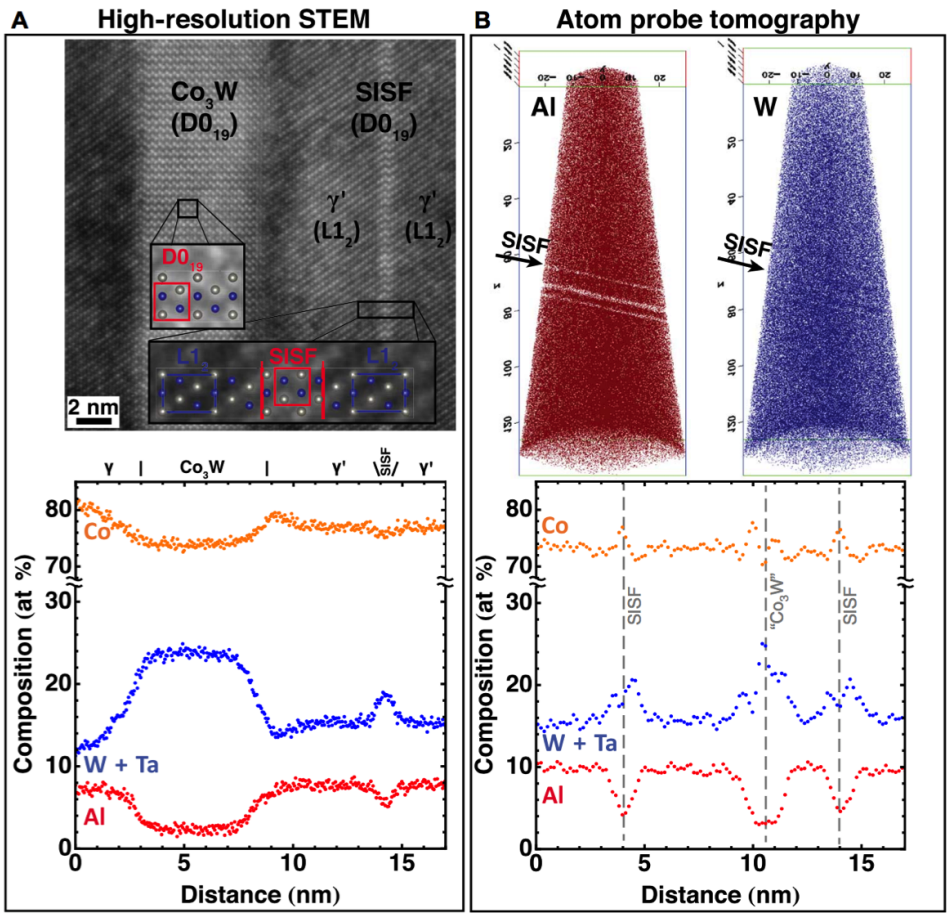

Figure 5.13: a) High-resolution HAADF image from the black box region in Figure 5.12b). An SISF is located adjacent to a Co_3W $D0_{19}$ lath. Vertically integrated EDS line scans across this region reveal differences in composition. b) APT reconstructions where a SISF intersects the APT tip on a {111} plane.

construction in which a hyperplane is simultaneously tangent to the free energies of all equilibrium phases to determine atomic fraction. Unlike bulk equilibrium, the segregation at stacking faults is determined by the Suzuki criterion, which requires an equality of chemical potential differences. This criterion arises from the constraint that segregation occurs at the expense of the atoms within the fault while the thickness is fixed. As the Co concentration within the γ' phase and Co_3W phases are very close to 75 at %, we can effectively model the equilibrium criteria along the Co_3Al-Co_3W composition axis. This

allows the Suzuki segregation criterion to reduce to:

$$(\frac{\partial g^{\gamma'}(c_W^{\chi})}{\partial c_W^{\chi}})|_{c_{\gamma'},N} = (\frac{\partial g^{\chi}(c_W^{\chi})}{\partial c_W^{\chi}})|_{c_{\chi},N} \tag{5.5}$$

In this expression, g^i represents the free energy of a given phase, either γ' or χ (SISF/Co_3W). Here c_W^i is the W concentration in the relevant phase and c_i is the equilibrium concentration of the γ' or χ phase. Because both the SISF and Co_3W exhibit a $D0_{19}$ crystal structure, we have used the bulk free energies to predict segregation at the stacking fault. The derivatives are taken while Co concentration is kept constant. In this fashion, for a known composition of γ', the slope of the Gibbs free energy curve can be determined and matched to the equivalent slope on the χ-Co_3W/SISF free energy curve located at the SISF equilibrium composition.

To calculate the bulk free energies of the two phases at finite temperature along the pseudobinary, a first-principles approach was used in which a cluster expansion was parameterized by 0 K DFT energies. The training set for this cluster expansion consisted of several DFT calculations performed using VASP [37, 105, 38, 67, 39]. This cluster expansion was subjected to grand canonical Monte Carlo simulations in order to calculate the effects of configurational entropy on the system. Vibrational free energy terms were incorporated into the overall free energy expression using the quasiharmonic approximation. The cluster expansion, Monte Carlo simulations, and vibrational calculations were all performed using the CASM code [106, 46, 45, 47].

The calculated free energies for the $L1_2$ and $D0_{19}$ phases are shown in Figure 5.14. The $L1_2$ phase exhibits a complete solid solution of W and Al across the entire composition range on the minority B sublattice while $D0_{19}$ is found to phase-separate. At low W compositions, although the $L1_2$ free energy is lower than that of the $D0_{19}$ phase it is still not globally stable. At high W concentration, Figure 5.14 shows that a two-phase

region exists between the $L1_2$ and $D0_{19}$ phases, determined by the common tangent construction. It is also apparent that this common tangent construction suggests there is very little solid solubility in the Co_3W phase and that, while in equilibrium with the $L1_2$ phase, the Co_3W phase is very nearly stoichiometric and can be approximated as a line compound. This approximation is consistent with the experimentally-observed composition of the 35-atomic-layer thick $D0_{19}$ laths coherently embedded within the $L1_2$ precipitates, suggesting that bulk thermodynamics are still operative when the thickness of the specimen is only 35 atomic layers thick.

Application of the Suzuki criterion in which the slopes of the free energy are set equal yields a somewhat different compositional result. This is shown in Figure 5.14b), in which a tangent to the $D0_{19}$ free energy is found with an equivalent slope to the $L1_2$ free energy curve at its experimental bulk concentration of $Co_{0.75}Al_{0.11}W_{0.14}$. Using this Suzuki criterion and the bulk $D0_{19}$ free energy, the predicted W concentration in the SISF is found to be 24 at %. This is considerably higher than what was observed experimentally, suggesting a breakdown in bulk thermodynamics for phases that are only a few atomic layers thick.

In order to account for the broken symmetries due to the nanoscale thickness of the SISF, an explicit statistical mechanics study of a periodic 32-atom $L1_2$ supercell containing a SISF was conducted, as shown in Figure 5.15a). An additional cluster expansion Hamiltonian was parameterized from first principles on the B sublattice sites and was subjected to similar grand canonical Monte Carlo simulations as before in order to predict the equilibrium concentrations of the SISF embedded within the $L1_2$ phase.

Figure 5.15b) shows the calculated sublattice site composition of the SISF as a function of the average $L1_2$ composition at 900 °C. The dashed line indicates that an average $L1_2$ composition of $Co_{0.75}Al_{0.11}W_{0.14}$ will result in an SISF composition that is predicted to be 21 at% W. This value, while smaller that what is predicted from the bulk $D0_{19}$ free

energy, is in agreement with the experimentally measured segregation along the SISF.

It is well known that thermodynamic properties can change significantly as a material is scaled from bulk to nanometer dimensions. However, it has proven difficult to quantify these changes experimentally because of the lack of control of particle shape and size as well as the thermodynamic boundary conditions. The unique nature of the coherent multiphase equilibrium in the Co-Al-W ternary system allows for the simultaneous existence of bulk $D0_{19}$ precipitates that arise from decomposition reactions and thin 4-atom thick SISF plates of $D0_{19}$ that arise from plastic deformation of the specimen. These two structures form in the vicinity of and parallel to one another, ensuring that they both exist in the same thermodynamic reservoir and under similar mechanical boundary conditions. Emerging imaging and spectroscopy approaches were combined with first-principles computations in order to assess the thermodynamic driving forces and changes in segregation as a function of size. Both the experimental and computational results show conclusively that the equilibrium composition of the bulk Co_3W phase is not equal to the equilibrium composition of the SISFs and that the SISF equilibrium composition is more accurately modeled using direct atomistic simulations than via the context of the Suzuki equilibrium criterion.

The difference in equilibrium composition between the SISF and the thicker $D0_{19}$ plates is not surprising considering that the SISF is only 4 atomic layers thick. This finite thickness means that second nearest neighbor interactions on the B sublattice between the atoms in the SISF layer and in the bulk $L1_2$ matrix are possibly relevant. Indeed, in the cluster expansion of the $L1_2$ + $D0_{19}$ supercells, 3 of the 11 non-singlet clusters are between $L1_2$ and $D0_{19}$ portions of the supercell. These interactions are not possible in the bulk phases and it is therefore possible to rationalize why there is a lower concentration of W within the SISF by inspecting the bulk free energies of $L1_2$ and $D0_{19}$. As atoms within the SISF sample not only the hexagonally-close packed environment of the $D0_{19}$

structure but also the cubic environment of the $L1_2$ phase via second nearest-neighbor interactions, the W concentration in the SISF is a compromise between the high value of bulk $D0_{19}$ and the lower $L1_2$ value.

Even small amounts of segregation of W and Ta can significantly lower the SISF energy within the γ' phase [104]. This reduction in SISF energy locally assists the dislocation shearing process, as there is a direct linear relationship between SISF energy and the critical shear stress for the γ' phase [107]. Compression tests conducted at 900 °C at a strain rate of 10^{-4} s^{-1} revealed segregation at the SISFs, suggesting that the process of segregation occurs quickly at these length scales and that diffusion is not the rate-limiting step for plastic deformation. Instead, the SISF energy quickly decreases and allows the leading dislocation to shear the γ' phase under a lower applied stress.

This decrease in required shear stress is not necessarily detrimental to overall high-temperature creep strength because of the formation of very stable coherent boundaries, which have been shown to provide strength in other materials systems [108]. Segregation serves to increase the susceptibility of SISF formation and could serve to increase the strength of alloys during high-temperature creep.

5.7 Summary

Using GSF surfaces generated from first-principles calculations, phase field models have been used to determine deformation mechanisms in γ' precipitates of Co- and CoNi-base superalloys. Both single AB a/2<110> dislocations and pairs of AB+AC a/2<112> dislocations were considered as they interacted with a γ' particle. In the Co-base composition, the single AB type dislocation is found to loop the γ' precipitate due to the relatively high APB energy. The AB+AC dislocation configuration shears the γ' precipitate by creating an SISF. In the CoNi-base composition, the AB dislocation shears the

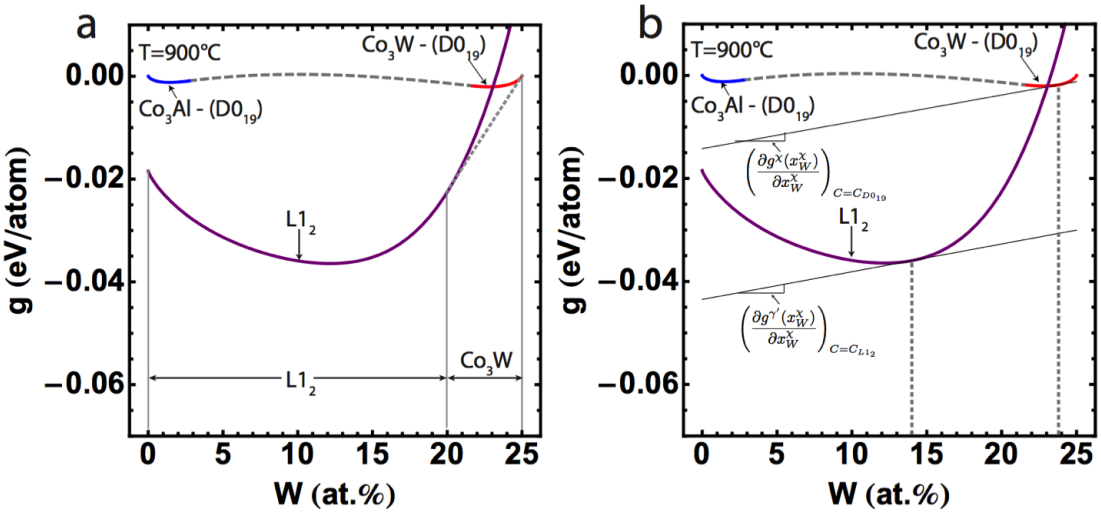

Figure 5.14: First-principles free energy curves of the $L1_2$ and $D0_{19}$ phases. a) Gibbs free energies at 900 °C in which the $L1_2$ phase is found to be stable between 0 and 20 at% W and the $D0_{19}$ phase is found to be stable from 20 to 25 at% W. b) Gibbs free energies at 900 °C in which the Suzuki criterion is satisfied. Equilibrium concentrations are found to be Co-11Al-14W at% for the $L1_2$ and Co-1Al-24W at% for the $D0_{19}$ phase.

precipitate and creates an APB due to the relatively low APB energy while the AB+AC dislocation configuration creates an SISF ribbon with an APB of the a/2<112> type. These results are consistent with TEM observations. Several factors, including stacking fault energy, local curvature, and the minimum energy path maxima, influence the deformation pathways and resultant microstructures. Segregation in CoNi-base superalloys may alter the GSF energy landscape in significant ways, yielding an APB/SISF/APB configuration that is stabilized by friction forces.

High-resolution STEM HAADF imaging, EDS maps, and APT have shown solute segregation in the vicinity of SISFs. This solute segregation was found to be consistent with a change in composition from the host γ' phase toward the thermodynamically stable Co_3W bulk phase, although the equilibrium composition of the nanoscale SISFs was not observed to be identical to the bulk phase. First-principles calculations, consisting of ground state formation energies, Monte Carlo simulations, and finite temperature

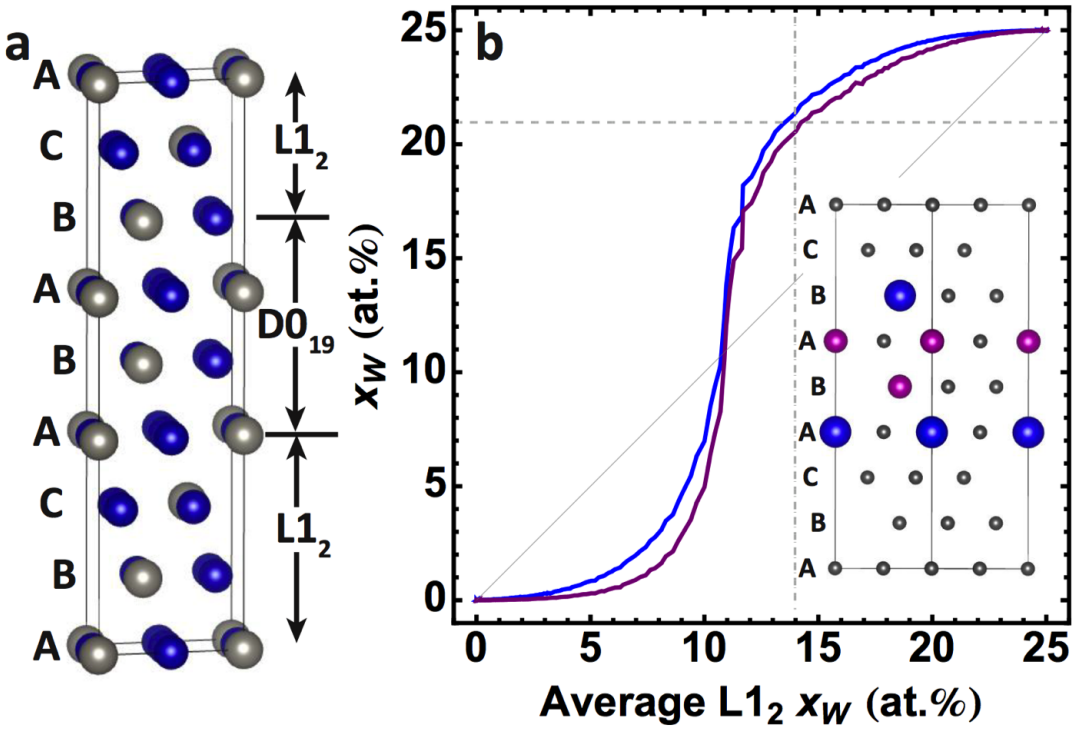

Figure 5.15: Direct atomistic simulation of the equilibrium stacking fault composition. a) $L1_2$ supercell with embedded $D0_{19}$ layer b) (Inset) Average concentration for each sublattice site (colored) as a function of the average $L1_2$ composition determined from the $L1_2$ layers in the 32-atom supercell. For W-rich compositions, the average composition within the SISF is higher, as shown by the dashed gray line at approximately 14 at% W.

phonon energies qualitatively predict a change in composition toward the bulk Co_3W phase but do not reproduce the experimental observations quantitatively. An explicit treatment of a coherently-embedded SISF within the $L1_2$ matrix instead results in better conformity between model and experiment. These experiments, combined with the first-principles modeling, conclusively demonstrate the breakdown of bulk thermodynamics at the nanoscale level despite the identical chemical and mechanical environment surrounding the nanoscale and bulk phases considered.

Chapter 6

Oxidation in Co-base Superalloys

6.1 Introduction

In this chapter, oxidation behavior is investigated for three cast novel Co-base γ-γ' alloys and a subset of alloys produced by combinatorial ion plasma deposition in order to explore the effect of Ni:Co ratio and Al content. Oxidation was performed at 1100 °C for 1 h in flowing dry air and the resulting oxide scale was characterized via luminescence spectroscopy and scanning electron microscopy (SEM) with energy dispersive spectroscopy (EDS). First-principles thermodynamic modeling of Co-Ni-W-Al-Cr-Ta-O compositions was conducted in order to assess whether or not an α-Al_2O_3 scale would form. The results in this chapter are largely drawn from Stewart, Rhein, et al. [109].

6.2 Motivation

If Co-base superalloys are to be competitive with Ni-base superalloys, they must not only exhibit comparable mechanical behavior but also must possess a certain level of intrinsic oxidation resistance due to the challenging environments experienced in service.

While modern superalloys typically include a thermal barrier coating that mitigates the need for intrinsic oxidation resistance, in practical applications these coating layers can be lost or damaged, exposing the underlying substrate to an aggressive environment within the gas turbine [110]. Optimally, a substrate will readily form a continuous α-Al_2O_3 scale that acts as a thermodynamically stable oxygen diffusion barrier. Additionally, α-Al_2O_3 scales are non-volatile in high temperature water vapor, unlike the chromia scales that form in earlier generations of Co-base superalloys [111, 112]. In assessing the effects of higher order alloying additions in the Co-Al-W system, there are often trade-offs between γ' stability and ease of α-Al_2O_3 scale formation. For example, prior studies have shown that the addition of B and Cr improve oxidation [113, 114] while depressing the γ' solvus temperature [113, 21]. Another study has also shown that photostimulated luminescence spectroscopy is an effective rapid screening technique for the presence of α-Al_2O_3 in these alloys [115]. Other research has shown that the α-Al_2O_3 layer obeys a parabolic growth rate law and nucleates from the γ matrix channels [116].

Past research has shown that an external Al_2O_3 scale can form in Co-base γ-γ' alloys [113, 114, 16, 117]. This scale is typically non-continuous and overlaid by 10-100 μm of non-protective oxides. The growth of these oxides is often accompanied by changes in composition of the underlying substrate, which can yield deleterious phases such as Co_3W. Some amount of non-protective oxide is locally acceptable, although the oxidation rate should proceed slowly. Of the alloys reported in the literature, one of the most oxidation resistant γ-γ' Co-base alloys is Co-7Al-7W-10Cr (at.%), which forms approximately 1.3 μm of oxide scale after 196 h of cyclic oxidation at 800 °C [113]. Co-base alloys should also preferably form a continuous oxide layer in short times on the order of an hour so as to minimize the growth of overlying oxides and excessive Al depletion beneath the alumina scale.

First principles thermodynamic modeling can be used to investigate stable oxide

phases. This has been combined with a combinatorial synthesis approach has been undertaken in order to broadly explore multidimensional compositional space in order to assess α-Al_2O_3 formation. The feasibility of developing Co-base superalloys with a desirable combination of oxidation and γ' stability at 1100 °C has been assessed.

6.3 Oxidation Alloy Composition

An initial set of three exploratory Co-base alloys were investigated (Table 6.1). These alloys contain large amounts (>7 at%) of Cr for oxidation resistance. These alloys also contain a large amount of Ni and Ta to expand the γ' phase field and improve precipitate stability. These alloys also contained trace amounts of C, B, Y and Mo and have solvus temperatures in excess of 1000 °C. Co-1 is a baseline alloy and Co-2 and Co-3 have only small variations, mainly in the inclusion of trace amounts of Y and Y+Mo, respectively. All of these alloys were vacuum induction melted and then solution heat treated at 1200 °C for 4 h and aged at 950 °C for 50 h. Buttons from these ingots were machined prior to oxidation.

A set of three combinatorial libraries were also fabricated via ion plasma deposition (IPD) in order to systematically determine the effects of composition on oxidation behavior in Co-base γ-γ' alloys. Each library consisted of a triangular array of 78 buttons arranged beneath three cathode sources at the corners. The compositions of the five cathodes used in Table 6.2. All of the cathode sources contained the baseline Co, Al, W elements as well as Cr for oxidation resistance and Ta for improving γ' stability. Cathodes 1 and 2 were used in all three combinatorial libraries so as to create compositions with widely varying Ni:Co ratios. The work here concentrates on the library formed by Cathodes 1, 2, and 5, which provides a varying concentration in Al in order to determine the effects on α-Al_2O_3 formation.

In order to minimize interdiffusion with the deposited alloy, compositions were deposited on buttons with composition roughly corresponding to Cathode 1. Each button was approximately 12.7 mm in diameter and 2.5 mm in height. The centers of these buttons were separated by approximately 20 mm from their nearest neighbors and the cathodes were centered above corners of the library. The composition of each button varies systematically between the cathode sources depending on its position in the array. These compositions were created in order to represent a range of potential structural alloys and not bond coats for thermal barrier coatings.

Coating thickness on each button was targeted to be 150 μm, enough to mimic bulk alloy behavior accurately. All combinatorial buttons were solution heat treated at 1200 °C, well above the highest estimated γ' solvus temperature. Specimens were allowed to age during the oxidation treatment. All samples were oxidized at 1100 °C in flowing dry air. Samples were inserted into the pre-heated hot zone of the tube furnace, held for a prescribed time, and then withdrawn over the course of 2 minutes. Both the exploratory and combinatorial buttons were oxidized for one hour.

Table 6.1: Compositions of Three Exploratory Co-base Alloys

	Co (at%)	Ni (at%)	W (at%)	Al (at%)	Cr (at%)	Ta (at%)
Co-1	43.61	27.41	5.60	8.82	12.37	1.88
Co-2	42.84	30.08	5.44	8.64	8.97	3.68
Co-3	42.37	32.00	5.56	8.55	7.60	2.55

Table 6.2: Compositions of Cathodes used in Combinatorial Libraries

	Co (at%)	Ni (at%)	W (at%)	Al (at%)	Cr (at%)	Ta (at%)
Substrate	79.7	0.0	6.7	8.9	3.3	1.5
Cathode 1	77.1	0.0	5.9	12.2	3.4	1.4
Cathode 2	33.5	35.4	11.8	14.4	3.4	1.5
Cathode 3	30.0	29.3	6.0	11.8	21.5	1.4
Cathode 4	40.9	40.4	0.0	13.8	3.5	1.4
Cathode 5	33.4	34.6	6.5	20.7	3.4	1.4

6.4 Ternary Co-base Superalloy Oxidation

The baseline thermodynamic stability of binary and ternary intermetallics in the Co-Al-W and Ni-Al-W systems were determined using density functional theory (DFT). Calculations were performed using the plane-wave pseudopotential-based Vienna *ab initio* simulation package (VASP) [36, 67]. The Perdew, Burke, and Ernzerhof (PBE) general gradient approximation was used for the exchange and correlational functional [67, 39, 37]. Oxide energies were also calculated in a similar manner and compared to the values in the Materials Project database [118]. The original oxide formation energies, g, were modified to obtain a new characteristic potential, ϕ dependent on chemical potential:

$$\phi = g - \mu_O N_O \tag{6.1}$$

In this expression, μ_O is the oxygen chemical potential and N_O is the number of oxygen atoms in the chemical formula. As oxygen activity and chemical potential are proportional to one another, chemical potential can be used as a stand-in for activity in determining the sequence of thermodynamically-favorable oxides that will form on a given substrate. This can be done by systematically varying the oxygen chemical potential and then minimizing the characteristic potential, ϕ. This can be easily visualized for less complex systems such as Co-Al-W but the same approach can be used in predicting oxide sequence in higher-order systems such as the Co-Ni-W-Al-Cr-Ta investigated here experimentally.

In the ternary Co-Al-W system, a minimum characteristic potential convex hull can be generated, as seen in red in Figures 6.1 and 6.2. Example chemical potential values were chosen for clarity and correspond to the outermost oxide layers in this ternary sytstem. In these figures, a representative γ-γ' phase field is indicated by the black circle. The stable phases compromising the characteristic potential convex hull at low

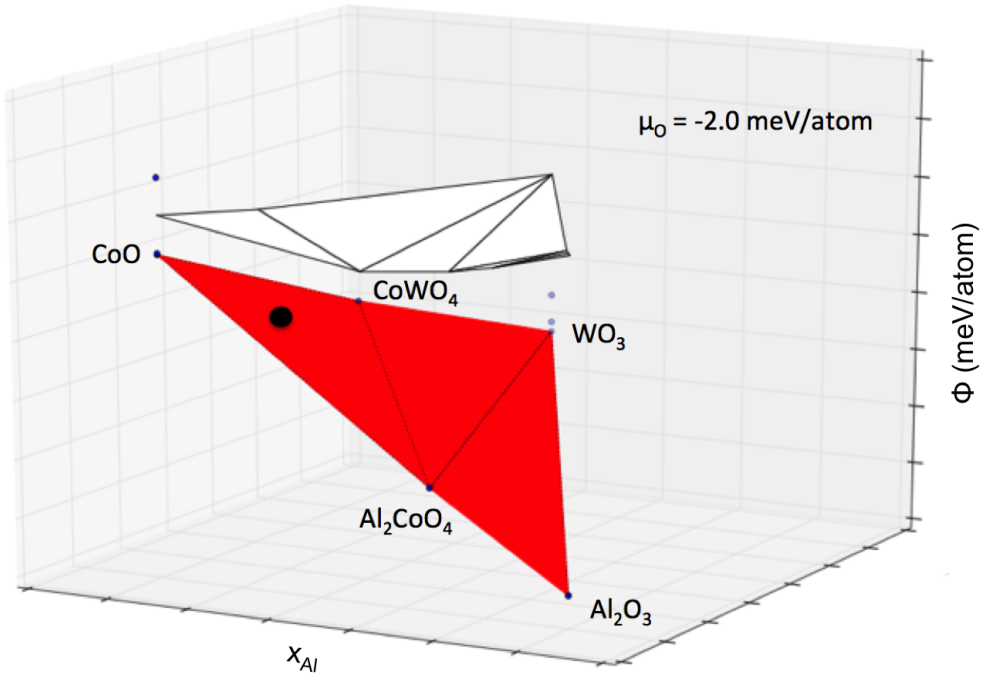

Figure 6.1: Stable convex hull of characteristic potential ϕ at example chemical potential of μ_O=-2.0 meV/atom. Two-phase γ-γ' composition indicated by black point. Stable oxides form the corners of this region.

oxygen chemical potential is indicated by the white convex hull. As can be seen in both figures, at the labeled chemical potentials, only oxides compromise the stable phases and there are no other intermetallic phases. Intuitively, oxide phases with more oxygen in their chemical formula exist at higher oxygen chemical potential. The two values of oxygen chemical potential selected in Figures 6.1 and 6.2 correspond to the values that stably form the outermost predicted Co oxide layers in the Co-Al-W, CoO and Co_3O_4.

The sequence of most predicted stable oxides in the Co-Al-W system is shown in Figure 6.3. Due to the relatively stable baseline formation energy of Al_2O_3, it is the oxide expected to be in equilibrium with the substrate. The next most stable oxide is the

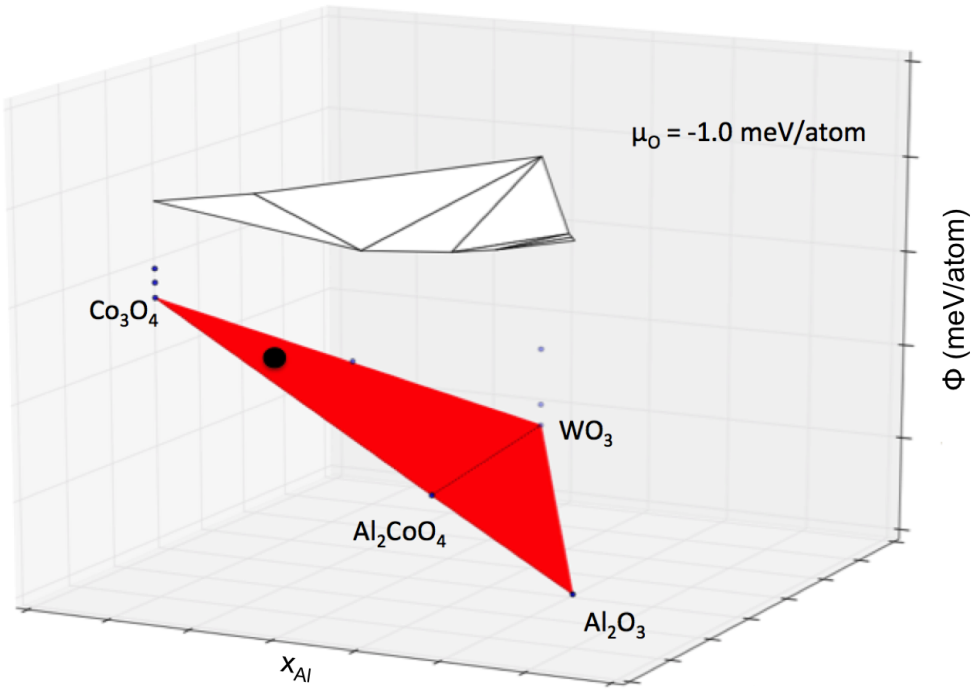

Figure 6.2: Stable convex hull of characteristic potential ϕ at example chemical potential of μ_O=-1.0 meV/atom. Two-phase γ-γ' composition indicated by black point. Stable oxides form the corners of this region.

Al_2CoO_4 spinel, followed by a tungsten oxide phase and cobalt tungstate. Two cobalt oxides, CoO and Co_3O_4 are present in the outer stable layers and, beyond that, a small amount of WO_3 is stable in the outermost layer thermodynamically.

There are a number of caveats to this analysis. While these are the thermodynamically-favored layers expected to be in equilibrium with one another, this does not incorporate finite temperature effects. As such, oxide phases presented in this analysis have no solid solubility, which may have an impact on the layering sequence. More significantly, this analysis does not incorporate the effects of kinetics, which plays an important role in the developing oxide layers. W in particular is a slowly-diffusing species, which may kineti-

cally suppress the formation of the outermost WO_3 phase. Listing thermodynamically-favorable oxide layers also does not address the continuity or phase fraction of each layer. As a uniform Al_2O_3 layer is desirable, it is necessary to do experimental validation in order to determine the morphology of this layer.

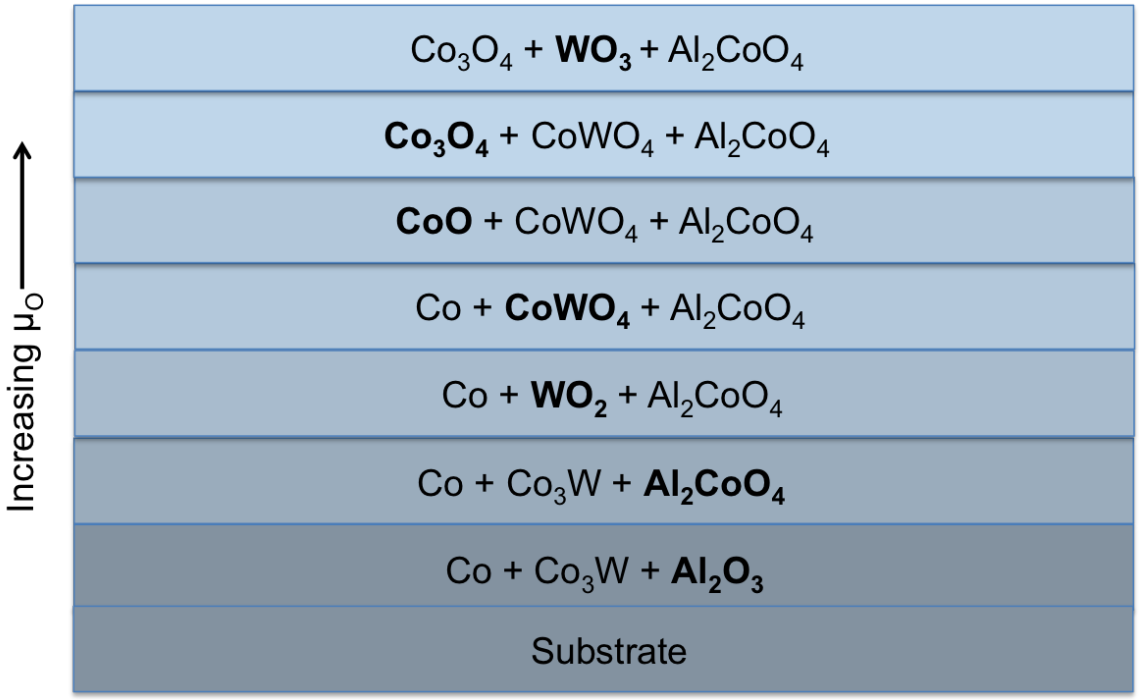

Figure 6.3: Sequence of most stable oxides predicted from a γ-γ' substrate in the Co-Al-W system. Boldface indicates phases that arise sequentially.

6.5 Exploratory Co-base Superalloy Oxidation

The oxide layer sequence of the three exploratory cast alloys in Table 6.1 are significantly more complicated due to the complex chemistry of the underlying substrate. Luminesce spectroscopy conducted on these three exploratory alloys at multiple different points indicated that, unlike many Ni-base superalloys, there is not a characteristic α-Al_2O_3 doublet except very weakly in the Co-3 sample. Multiple measurements were made because the scale on the three alloys spalled to varying degrees, most likely upon cooling

from the oxidation temperature. Backscattered electron images of the three exploratory Co-base alloys after oxidation in dry air for 1 h at 1100 °C are shown in Figure 6.4. A René N5 sample was also oxidized under identical conditions for comparative purposes. Of the samples analyzed in cross section, only the René N5 comparative sample formed a continuous α-Al_2O_3 layer after 1 h. The cast Co-base exploratory alloys exhibit discrete alumina particles within the metal matrix, forming an internal oxidation zone, or IOZ. As can be seen in Figure 6.4, the depth of this IOZ layer varies significantly between the samples, with Co-1 having the thinnest layer at approximately 3 μm. Segmentation of the IOZ of Co-1 via ImageJ analysis revealed that the area fraction of alumina was approximately 47%. In alloy Co-3, the IOZ consists of discrete alumina particles both within the alloy towards the substrate interior and particles enveloped within an inward-growing oxide later closer to the exterior of the sample. Spallation was frequently observed in this layer, exposing the underlying surface and potentially giving rise to the occasionally observed α-Al_2O_3 doublet in spectroscopy.

Chemical analysis of the oxide phases via EDS reveals that the outermost layers in Co-2 and Co-3 consist of Ni and Co and are likely a solid solution (Co,Ni)O as CoO and NiO are completely miscible at the test temperature [119]. Under this outermost (Co,Ni)O layer, Co-1 appears to contain a Co-Cr-Al-O layer accompanied by an underlying W/Ta-rich scale and IOZ consisting of discrete alumina particles within the metal matrix. The layers beneath the (Co,Ni)O in the Co-2 appear to be W/Ta-rich oxides interspersed with Co-Cr-Al-O, Cr_2O_3, and alumina particles within the matrix. The only notable difference between the layers in Co-2 and Co-3 appears to be that the IOZ in the Co-3 sample has an upper portion with an inward-growing W/Ta-rich oxide, while the bottom portion of IOZ is inside the metal.

In addition to this one-hour oxidation, small samples of Co-1 were further oxidized at 3 min, 10 min, and 1 hour at 1100 °C for comparative purposes. Representative mi-

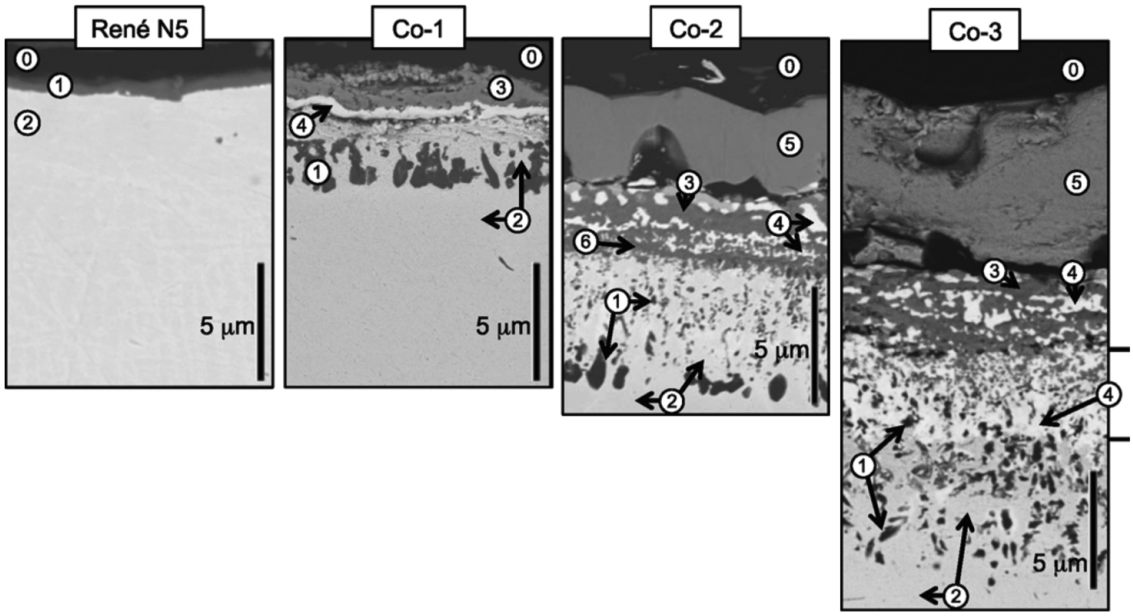

Figure 6.4: Backscattered electron images of René N5 and the three exploratory Co-base superalloys after oxidation in dry air for 1 h at 1100 °C. Layers are: (0) the mounting epoxy; (1) Al_2O_3 present as either a continuous scale or discrete particles; (2) the alloy; (3) Co-Cr-Al-rich oxide; (4) W/Ta-rich oxides present as a continuous external layer in Co-1 and as discrete particles in Co-2 and Co-3; (5) (Co,Ni)O; (6) Cr_2O_3

crographs of this oxidation are shown in Figure 6.5. In this oxidation series, discrete alumina particles first nucleate individually within the metal matrix, and small amounts of non-protective Co-base oxide layers already form after as little as 3 minutes of oxidation. These layers further develop over time, as the alumina particles coarsen while the IOZ grows deeper into the alloy. A W/Ta-rich oxide later develops by 10 minutes of oxidation and, while these layers coarsen further, no additional oxide phases were observed after one hour of oxidation.

A comparison can be made between what is observed experimentally in the 1 hour oxidized Co-specimens and what is predicted from a first-principles approach. Assuming no solid solubility and perfect equilibrium, the expected layering sequence of oxides in the Co-1 exploratory composition based on thermodynamics alone is shown in Figure

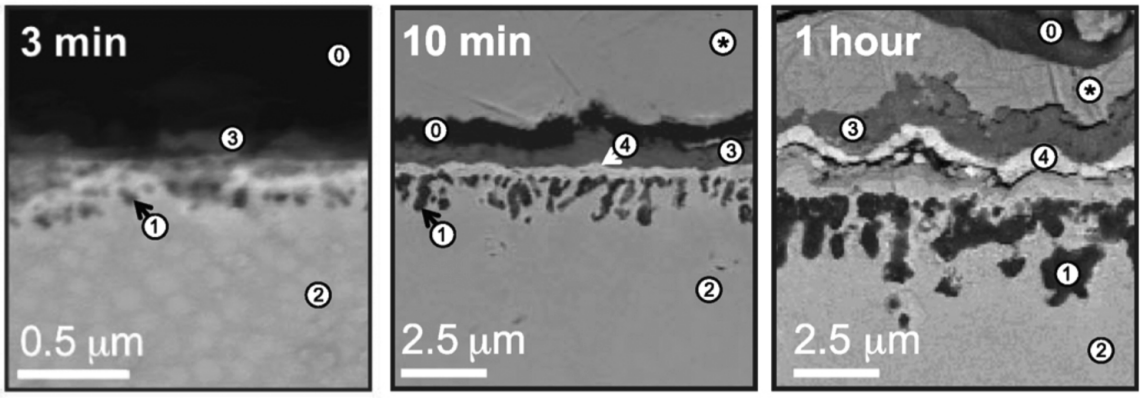

Figure 6.5: Backscattered electron images showing oxide scale evolution of the exploratory Co-1 composition between 3 minutes and 1 hour. EDS reveals the following layers: (*) Ni plating; (0) the mounting epoxy; (1) Al_2O_3 particles observed to nucleate within the substrate; (2) the alloy substrate; (3) non-protective Co-containing oxide; (4) W/Ta-rich oxide scale

6.6. As was the case in the ternary system, an Al_2O_3 layer is predicted to be stable and in contact with the substrate, which is also observed experimentally after 1 hour. The layer above the Al_2O_3 is found via EDS to be rich in Ta, which is likely the $AlTaO_4$ layer predicted from first-principles. The non-protective Co-rich oxides present after 1 hour also contain some trace amounts of Cr and may be either the spinel $CoCr_2O_4$ oxide phase or one of the multiple Co-rich phases shown in Figure 6.6.

It is apparent from Figures 6.5 and 6.6 that there are many more oxides predicted via DFT for the exploratory Co-1 alloy than there are observed experimentally after 1 hour in air at 1100 °C. There are a number of potential reasons for this discrepancy. Perhaps of most concern is that 1 hour of oxidation time may not be adequate in order to fully achieve thermodynamic equilibrium. This may explain why, unlike the other exploratory alloys, no external CoO or Co_3O_4 scale forms experimentally after 1 hour. There is also significant volatilization of Cr_2O_3 under these experimental conditions. As Cr_2O_3 is the nearest Cr-containing layer to the underlying substrate, if large amounts of Cr_2O_3 transform into gaseous CrO_3 it may prevent all additional Cr-containing oxide

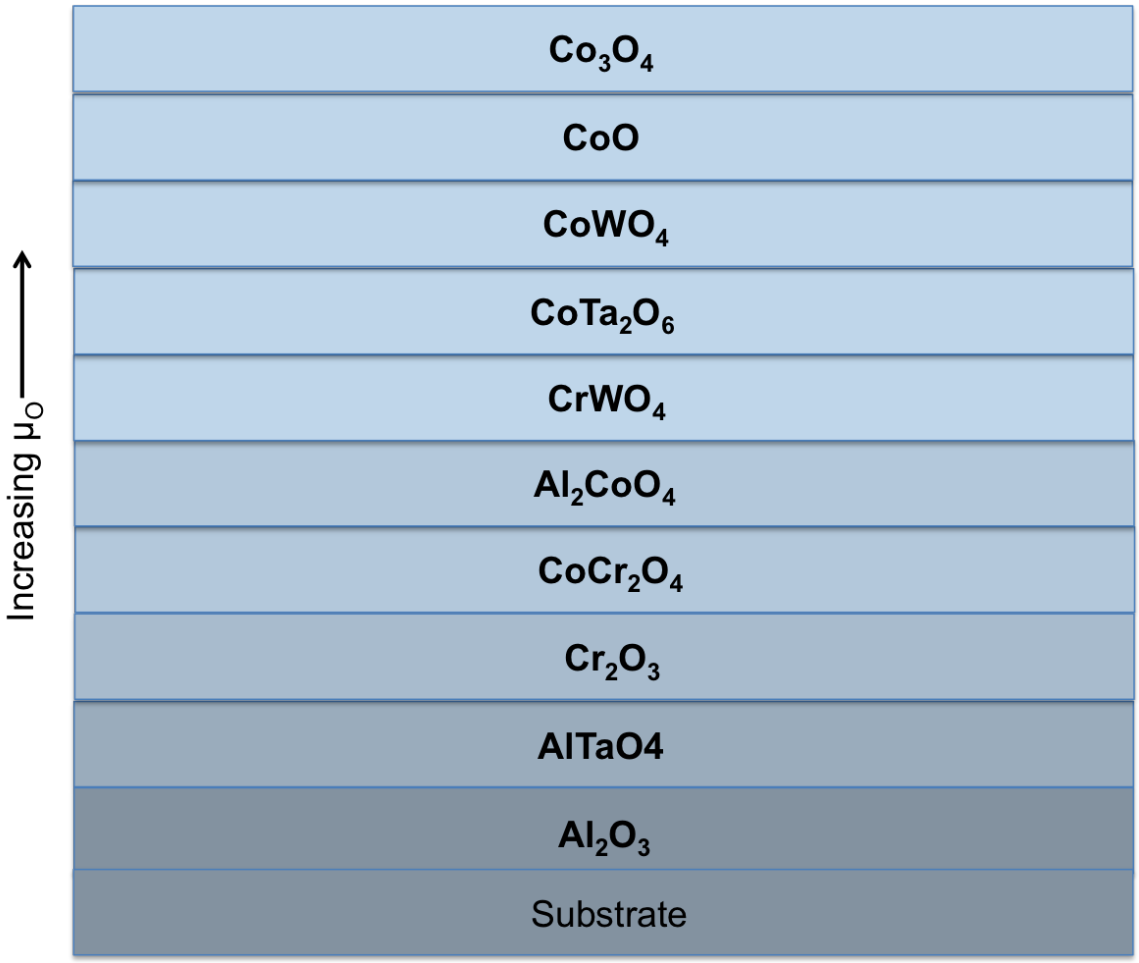

Figure 6.6: Predicted oxide layers in thermodynamic equilibrium at 0 K in the Co-1, Co-2, and Co-3 exploratory alloys.

layers from forming, significantly reducing the number of expected oxide layers.

In the Co-2 and Co-3 exploratory compositions, DFT predicts that the same layering sequence of oxides will form on the substrate as in Co-1 (Figure 6.6). While they contain less Cr in the substrate than the Co-1 composition, a number of Cr-containing oxide layers are present experimentally in Co-2 and Co-3 that are not present in Co-1 (Figure 6.4). In addition, there are external (Co,Ni)O and $(Co,Ni)_3O_4$ scales that are not present in the Co-1 exploratory alloy from EDS. There is therefore much closer agreement between first-principles and experiment. It is possible that these outermost (Co,Ni)O and $(Co,Ni)_3O_4$

oxide scales are quick to form in the Co-2 and Co-3 composition and prevent exposure of Cr to the air. This in turn limits the volatilization of Cr to the environment and allows a much more complex oxide scale to form, as seen in Figure 6.4. In particular, the increased amount of Ta within the Co-2 and Co-3 compositions may be correlated to the more complex set of Ta-containing oxides observed, including $AlTaO_4$ and $CoTa_2O_6$. Outside of the spinel phases, which may be kinetically suppressed, there is otherwise excellent agreement between experiment and first-principles expectations of the Co-2 and Co-3 exploratory compositions.

6.6 Combinatorial Co-base Superalloy Oxidation

Following IPD synthesis, resulting buttons were about 115 μm in thickness after deposition. These as-deposited coatings contained some porosity among a relatively compositionally-heterogeneous splat-like microstructure. Approximately 100 μm of coating thickness remained after solution heat treatment and removal of material during polishing of the button surfaces. The average grain size of the heat treated coatings was approximately 7 μm. The compositions of the combinatorial buttons as measured via EDS (Table 6.3) vary from those calculated from the cathode sources. However, the resulting combinatorial samples do explore an adequate compositional range for the desired oxidation studies, as seen in Figure 6.7.

Luminescence spectroscopy of oxidized buttons along the boundaries of the combinatorial library reveals some samples both with and without the characteristic α-Al_2O_3 doublet signal. This is shown in Figure 6.8, in which samples that exhibited the α-Al_2O_3 doublet signal are green and those that do not are red. Of the tested buttons, there appears to be a large compositional region where samples display the α-Al_2O_3 doublet. This region encompasses regions higher in Al as well as in Ni:Co ratio, originating at

the boundary between Cathodes 2 and 5. Near compositions closer to Cathode 1, the characteristic doublet is not present.

Table 6.3: Compositions of Select Unoxidized Combinatorial Buttons after Solution Heat Treatment and Polishing

Button	Co (at%)	Ni (at%)	W (at%)	Al (at%)	Cr (at%)	Ta (at%)
3-1B	65.8	11.2	9.4	7.7	2.3	3.6
3-1D	60.0	16.2	9.7	8.6	1.7	3.9
3-1E	55.0	20.1	9.6	9.9	1.8	3.6
3-1F	51.1	23.3	9.7	10.5	1.7	3.7
3-1H	41.7	31.9	10.1	11.3	1.6	3.5
3-1J	38.3	35.2	10.0	11.4	1.4	3.8
3-1L	35.5	37.6	10.1	11.3	2.3	3.3
3-4C	54.4	20.4	9.2	10.3	2.1	3.5
3-4D	51.2	24.1	8.9	10.4	1.7	3.6
3-5A	57.7	18.0	9.5	9.8	1.2	3.8
3-12A	37.9	34.5	7.1	15.5	1.9	3.0

The transition between regions where α-Al_2O_3 is detectable by luminescence and where it is not found is approximately bounded by a line between buttons 3-1E and 3-1F, 3-4C and 3-4D, and 3-5A and 3-6A. Comparing the SEM EDS signals of these unoxidized samples reveals that this transition occurs approximately along a line of constant 10.4 at.% Al concentration and Ni:Co ratio of 0.46, as seen in Figure 6.7. Oxidation of the remaining buttons, combined with cross-sectioning and compositional analysis, is required in order to accurately define the boundary between the α-Al_2O_3 and non-forming domains, as well as to assess the specific effects of Al and Ni:Co ratio on oxidation behavior individually.

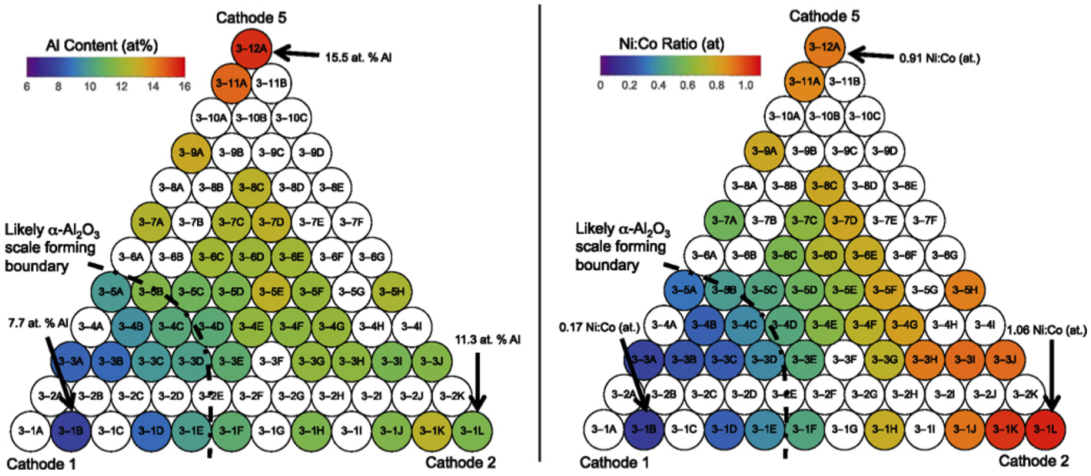

Figure 6.7: Relative positions of combinatorial buttons in the library comprised of Cathodes 1, 2, and 5. The figures are colored by concentrations of Al on the left and Ni:Co ratio on the right for select buttons after solution heat treatment and polishing (measured by EDS). Compositional gradients are visible, with Al content increasing primarily vertically across the library and Ni:Co ratio increasing primarily horizontally.

6.7 Combinatorial Co-base Superalloy Thermodynamic Assessment

In order to provide insight into the thermodynamically favorable sequence of oxide formation, first principles calculations were performed for select combinatorial buttons in the senary Co-Ni-W-Al-Cr-Ta system, representing the approximate corners of the combinatorial library in Figure 6.8 (3-1B, 3-1L, and 3-12A). Among all the possible oxide compounds considered, Al_2O_3 has the largest magnitude formation energy at 0 K at -3.44 eV/atom. As chemical potential of oxygen is increased, it is therefore intuitive that Al_2O_3 is the first oxide to come into thermodynamic equilibrium with the alloy substrate for all compositions considered. This is driven by the superior stability energy of α-Al_2O_3 and the relatively low amount of Al required to form this oxide. As the oxygen chemical potential is allowed to increase further, the sequence of thermodynamically

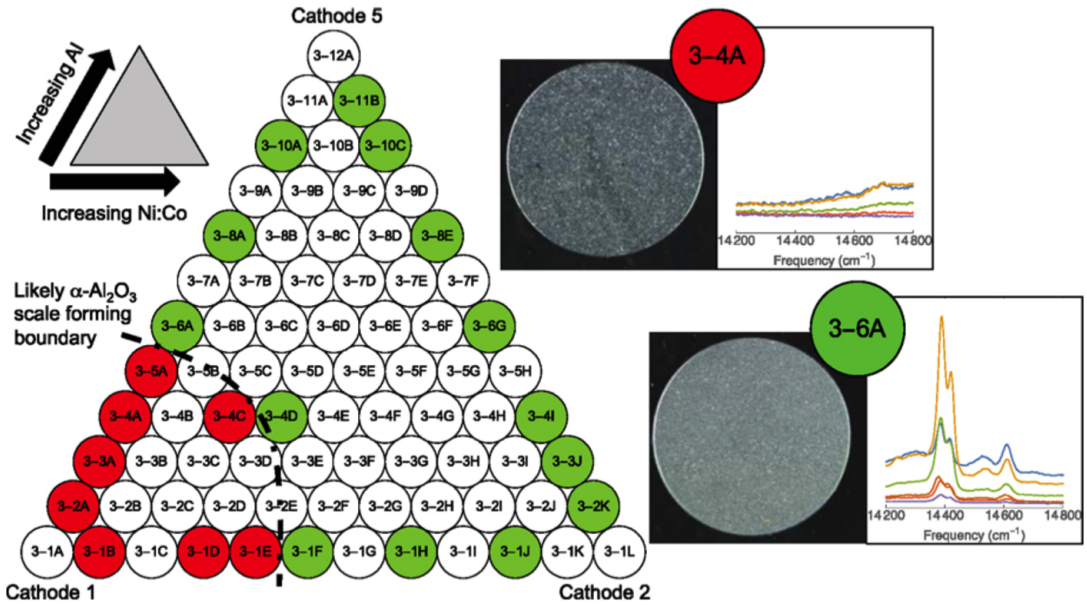

Figure 6.8: Relative positions of combinatorial buttons in the library comprised of Cathodes 1, 2, and 5. The figures are colored by concentrations of Al on the left and Ni:Co ratio on the right for select buttons after solution heat treatment and polishing (measured by EDS). Compositional gradients are visible, with Al content increasing primarily vertically across the library and Ni:Co ratio increasing primarily horizontally.

favorable oxides was found to be $AlTaO_4$, Cr_2O_3, spinel $CoCr_2O_4$, and spinel $CoAl_2O_4$ for the three button compositions calculated (Figure 6.9). Beyond the $CoAl_2O_4$ layer, the scale differs considerably among the three compositions. While all contain $CrWO_4$, $CoTa_2O_6$, $CoCr_2O_4$ at higher oxygen chemical potential, as well as CoO, only the 3-1B and 3-12A compositions were predicted to contain $CoWO_4$, and only 3-1B was calculated to contain WO_2. Additionally, the location of the $CoTa_2O_6$ layer in the stack differs for the 3-12A composition, where it is calculated to lie below the $CrWO_4$ layer. With even greater oxygen potentials, the spinel Co_3O_4 is predicted to become stable, and even higher oxygen potentials are needed before the Ni oxides are stabilized (not included in Figure 6.9). As these calculations are at 0 K, no solid solubility is included in these predictions. A significant implication is that layers with the same structure are immiscible, such as

the $CoAl_2O_4$ and $CoCr_2O_4$ spinels.

6.8 Discussion

No continuous alumina scale is revealed for any of the three exploratory cast Co alloys after the 1 h oxidation tests. The substrate of these alloys contains between 8.55 and 8.82 at.% Al. The Co-1 alloy has an internal alumina volume fraction of 0.47, which is relatively high when compared with the few available quantified critical oxide volume fractions necessary for external scale formation. In addition, the measured γ' solvi of the three cast alloys approach the nominal temperature range of interest above 1100 °C. This suggests that with proper selection of alloying additions, it should be possible to design a multicomponent Co-base γ-γ' alloy that forms an external α-Al_2O_3 scale and has a comparable solvus to Ni-base superalloys for the intended applications. However, based on the results of the cast alloys, it is evident that achieving the combination of goals is non-trivial.

In order to help identify the conditions under which alumina scale is achievable for γ-γ' Co alloys, it would be desirable to model both the thermodynamics and the kinetics of the oxidation reactions, although this is likely computationally intractable for a system this size. First principles calculations at 0 K indicate indicate that α-Al_2O_3 is by far the thermodynamically most stable oxide. A large number of stable Co-containing oxides are also expected at higher oxygen potentials, resulting in non-protective outer layers.

In light of these modeling limitations, an experimental approach based on the synthesis of combinatorial libraries is being used to explore the composition space where alumina scales may be formed in Co-base γ-γ' alloys, and how systematic changes in composition affect the ability of Co alloys to form alumina scale. This work indicates that compositions of xCo-yNi-10W-zAl-2Cr-3.5Ta at.%, where the ratio y/x is at least

0.46, and z is at least 10.4 at.% are likely to yield alumina scales upon oxidation at 1100 °C. It is also important to indicate that the small grain size of the combinatorial buttons likely benefits alumina formation, and therefore the Al content necessary for external scale formation after short times is likely higher at larger grain sizes. In the context of these combinatorial results, all three cast alloys have Al contents somewhat below 10.4 at.%, as shown in Table 6.1, which is the minimum amount necessary for detectable α-Al_2O_3 in the present combinatorial library. In fact, none of the cast alloys are able to form an external α-Al_2O_3. While the cast alloys have higher Cr contents than the combinatorial samples in this library, and it is known that higher Cr contents promote oxidation resistance as noted earlier, the extent of the Cr influence on oxidation behavior remains under investigation based on the remaining cathodes.

Beyond the potential for forming alumina, it is of interest to assess the expected formation of other oxides that may promote or interfere with the formation of the alumina scale. Because the Ni:Co ratio and Al contents of the three cast alloys fall within the ranges explored by the present combinatorial library, one can then compare the thermodynamic predictions for the layered scales with those observed experimentally. The oxide layer ordering predicted in Figure 6.9 is qualitatively consistent with that observed experimentally in the cast alloys. Although the alumina formation was internal, α-Al_2O_3 is found to be the most thermodynamically favorable oxide to form on γ-γ' alloys regardless of Co:Ni ratio or Al content. Only certain layers of those predicted were actually observed in the cast alloy scales. Notably, $AlTaO_4$ was not observed, presumably because this phase was only calculated to be present at small (< 5 %) phase fractions. Additionally, there is also no predicted Ni content in the phases, in contrast with the experimental observations. This discrepancy is most likely a result of the absence of configurational entropy contributions in the calculations because of the implicit assumption of no solubility at 0 K. A cluster expansion technique combined with Monte Carlo simulations can

be used to incorporate the effects of configurational entropy.

Kinetics clearly play a paramount role in determining whether the α-Al_2O_3 scale forms externally or as an internal oxide. This kinetic influence is most apparent in the samples oxidized for times less than 1 h (Figure 6.5), where internal alumina particles are observed to nucleate and remain discrete and form and IOZ underneath other external oxides. It is possible that from the development of non-protective externals oxides formed in addition to the alumina that may alter the mechanisms and kinetics of scale formation and disrupt the process of forming the continuous α-Al_2O_3 scale. Cross-section analysis of oxides grown on the three cast alloys reveals a W-rich oxide enveloping alumina particles in the IOZ of the Co-3 alloy. An inward-growing oxide such as this may have the potential to disrupt external scale growth, however Co-1 and Co-2 both exhibit internal oxidation without the presence of this inward-growing oxide phase. This implies the differentiating factor between internal and external alumina formers in the presence of other competing oxides requires a more comprehensive analysis.

6.9 Summary

We have found that Co-base γ-γ' alloys form alumina scales in air at 1100 °C within the composition window investigated. α-Al_2O_3 is predicted to be the most thermodynamically stable oxide across all the Co-Al-W γ-γ' compositions considered. Because of kinetic factors, this α-Al_2O_3 may form as an undesirable, non-protective assemblage of internal alumina particles within the metal rather than as a continuous, protective scale. Combinatorial experiments revealed that external alumina scale formation in alloys with approximately 7 μm grain size occurs in compositions of xCo-yNi-zAl-10W-2Cr-3.5Ta at.%, where the ratio y/x is at least 0.46 and z is at least 10.4 at.%.

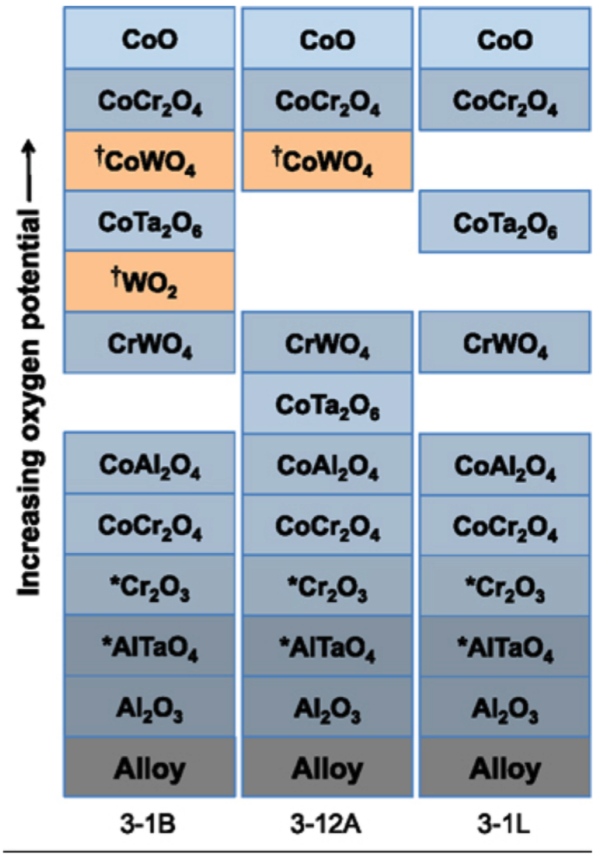

Figure 6.9: Order of thermodynamically favorable oxides with increasing oxygen chemical potential (from bottom to top) in select combinatorial compositions at 0 K, calculated from first principles. Alloy phases calculated with less than 5 % phase fraction are marked (*) and phases calculated to not be present in all compositions are highlighted in orange and marked (†). Samples 3-12A and 3-1L have similar Ni:Co ratios, and samples 3-1B and 3-1L have lower Al content than 3-12A.

Chapter 7

Conclusions and Future Recommendations

7.1 Conclusions

The overall objective of this research was to determine phase stability within the Co-base superalloys in order to inform experiments and increase the high temperature performance of this class of materials. Previous research has demonstrated that these alloys have creep performance comparable to second-generation Ni-base superalloys but exhibit different deformation mechanisms deriving from the different properties of the $L1_2$ phase in the Co-Al-W system. We have used a first-principles based approach using the cluster expansion formalism to examine the stability of a number of important ordered phases in the Co-Al-W ternary system. These and other first principles results have been used both to inform creep experiments and as input to other models. Oxidation modeling using first principles approaches has also been performed for Co-base systems. In this chapter we summarize the key findings of this research and conclude with future recommendations for continued study of Co-base superalloys.

The key findings of this investigation into the phase stability and high-temperature creep performance of Co-base superalloys are as follows:

1. At temperatures above approximately 600 °C, the $L1_2$ γ' phase is stable relative to a three-phase ground state mixture of elemental Co, B2 CoAl, and $D0_{19}$ Co_3W if the B sublattice of the $L1_2$ structure is treated with a binary cluster expansion. This stability derives from the combined effects of configurational and vibrational entropy at elevated temperature. The most stable compositions were found to be rich in W on the B sublattice. The stability energies were relatively small at the elevated temperatures where these alloys are used, on the order of 10 meV.

2. A full ternary cluster expansion of the Co-Al-W system was conducted, including separate FCC, BCC, and HCP cluster expansions. While relatively little solid solubility was observed in the three-phase ground state phases, it was shown that there exists a small $L1_2$ phase field at 1200 K at $Co_3(Al_{0.2},W_{0.8})$. As with the pseudobinary analysis, this stability is small (on the order of 10 meV) and attributable mainly to vibrational effects.

3. Solubility limits of Ti, Ta, and Nb in quinary Co-Al-W-X-Y superalloys were established and single crystals were cast via the conventional Bridgman process. Creep properties at 900 °C and 982 °C were characterized. At the lower temperature, deformation was found to be dominated by the formation of SISFs and at high temperature the deformation is dominated by APB-coupled dislocations through each precipitate. These observations are found to be consistent with first-principles DFT calculations that show SISF energy increasing with increasing temperature.

4. GSF surfaces have been generated from first-principles and used as input for parametric phase-field models of dominant deformation mechanisms in γ' precipitates of Co- and CoNi-base superalloys. Both single AB a/2<110> dislocations and pairs of AB+AC a/2<112> dislocations were considered as they interacted with a γ' particle.

In the Co-base composition, the single AB a/2<110> type dislocation is found to loop the γ' precipitate due to the high APB energy. The AB+AC a/2<112> dislocation configuration shears the γ' precipitate by creating an SISF. In the CoNi-base composition, the AB a/2<110> dislocation shears the precipitate and creates an APB due to the relatively low APB energy, while the AB+AC a/2<112> dislocation configuration creates an SISF ribbon with an APB. These results are consistent with observations made via TEM.

5. High-resolution STEM HAADF imaging, EDS maps, and APT have shown solute segregation in the vicinity of SISFs in Co-base superalloys. This solute segregation was found to be consistent with a change in composition from host γ' phase toward the thermodynamically stable Co_3W bulk phase, although the equilibrium composition of the nanoscale SISFs was not observed to be identical to the bulk phase. First-principles calculations, comprising ground state formation energies, Monte Carlo simulations, and finite temperature vibrational energies qualitatively predict a change in composition toward the Co_3W phase but do not reproduce the results quantitatively. An explicit treatment of a coherently-embedded SISF within the $L1_2$ matrix instead results in better agreement between model and experiment. These experiments and first-principles models conclusively demonstrate the breakdown of bulk thermodynamics at the nanoscale level despite the identical chemical and mechanical environment surrounding the phases considered.

6. The oxidation behavior of several exploratory CoNi-base superalloy compositions was investigated. All alloys were found to form alumina scales in air at 1100 °C. α-Al_2O_3 is predicted to be the most thermodynamically stable oxide, although, due to kinetic factors, it does not necessarily form as a continuous, protective scale. Combinatorial experiments were conducted and external alumina scale formation in alloys with approximately 7 μm grain size occurs in compositions of xCo-yNi-zAl-10W-2Cr-3.5Ta at.%, where the y/x ratio is at least 0.46 at z is at least 10.4 at.%.

7.2 Future Recommendations

This research has sought to built a foundational thermodynamic framework for the study of Co-base superalloys. While conventional CALPHAD-based thermodynamic databases have been shown to have excellent fidelity with experiment in well-calibrated composition domains, they often fail to provide accurate results when extrapolating to regions outside of known compositional space. The ability to determine equilibrium compositions from first-principles in multicomponent alloys presents many difficulties. Most principally is the size of the compositional space that needs to be considered in order to adequately fit a cluster expansion. Future work could use machine learning algorithms to intelligently identify regions of compositional interest in multicomponent systems, thereby limiting the number of calculations needed to rigorously describe quaternary and higher-order systems. This could be combined with rapid experimental assessment of new compositions using techniques such as 3-D printed compositionally-graded materials [120] and combinatorial sputtering approaches [121, 122].

Once this higher-order thermodynamic database is developed for multicomponent systems, an outstanding problem in Co-base superalloys is the modeling of alloy kinetics. In order to do this effectively, relevant hop barriers must be identified and the most relevant energy barriers calculated. Kinetic Monte Carlo simulations can then be performed as in [123] to determine diffusion coefficients in Co-Al-W and higher-order systems.

We observe very different γ' shearing mechanisms in Co-base superallys relative to their Ni-base counterparts at elevated temperature. These differences in creep deformation mechanisms are not attributable to a single materials property but instead the differences likely have dependence on a large number of materials properties and microstructural changes. As these properties are linked with one another, separating out single contributions from specific materials properties on the deformation mechanism

remains outstanding.

Another important problem is the study of antiphase boundary formation that includes the effects of segregation at the boundaries. Modeling the thermodynamics of an antiphase boundary, especially including the effects of vibrational entropy, is complicated by the fact that these faults break local symmetry. The basic thermodynamics of the system are also complicated and would require modeling a quaternary system if an analysis were performed on CoNi-base compositions as was done in our work. Modeling the equilibrium compositions near antiphase boundaries also presents a challenge.

Additional research on the thermodynamics and kinetics of stacking faults that incorporates solute segregation would be useful in understanding the creep deformation process. Like APBs, there is no thermodynamic or kinetic model that appears to predict the equilibrium composition at stacking faults. This is complicated by a number of factors, including the fact that the problem deals with the relatively complex interactions across a four-atom thick stacking fault. Current models do not take into effect solute segregation effects, which plays an important role in the dominant deformation mechanism at a given temperature and strain rate.

Much work remains to be done on Co-base superalloys in order for them to see application in gas turbine engines and other high temperature applications. While the study of Co-base superalloys has improved many existing thermodynamic databases and allowed for the investigation of previously poorly understood deformation mechanisms, improvements in the oxidation properties versus stability of γ' remains a key obstacle. If these alloys are to replace more than just current solid-solution and carbide-strengthened Co-base superalloys, these critical areas must be addressed. It is recommended that the intermediate space between purely Co- and Ni-base superalloys be more rigorously explored in order to find promising compositional domains.

Bibliography

[1] *Annual Energy Outlook 2017*, 2017.

[2] R. C. Reed, *The Superalloys: Fundamentals and Applications*. Cambridge University Press, 2006.

[3] P. C. Evans and M. Annunziata, *Industrial Internet : Pushing the Boundaries of Minds and Machines*, tech. rep., GE, 2012.

[4] Y. Honnorat, *The superalloys of nickel. Key to technologies at high temperature*, *Annales des Mines* (1985) 1–10.

[5] T. Strangman, G. Hoppin, C. Phillips, K. Harris, and R. Schwer, *Development of exothermically cast single-crystal Mar-M247 and derivative alloys*, *Superalloys 1980* (1980) 215–234.

[6] A. Jena and M. Chaturvedi, *The role of alloying elements in the design of nickel-base superalloys*, *J. Mater. Sci.* **19** (1984) 3121–3139.

[7] H. Okamoto, *Al-Ni (aluminum-nickel)*, *Journal of Phase Equilibria* (1993).

[8] M. J. Donachie and S. J. Donachie, *Superalloys Technical Guide 2nd Edition*. ASM International, 2002.

[9] T.M. Pollock and S. Tin, *Nickel-based superalloys for advanced turbine engines: chemistry, microstructure, and properties*, *Journal of Propulsion and Power* **22** (2006) 361–374.

[10] J. Donaldson and S. Clark, *Cobalt in Superalloys*. The Cobalt Develpment Institute, 1985.

[11] R. Jarret and J. Tien, *Effects of cobalt on structure, microchemistry and properties of a wrought nickel-base superalloy*, *Metall. Trans. A* **13** (1982) 1021–1032.

[12] J. Sato, T. Omori, K. Oikawa, I. Ohnuma, R. Kainuma, and K. Ishida, *Cobalt-base high-temperature alloys*, *Science* **312** (2006), no. 5770 90–91.

[13] M. Tsunekane, A. Suzuki, and T.M. Pollock, *Single-crystal solidification of new CoAlW-base alloys*, *Intermetallics* (2011) 636–643.

[14] J. Van Sluytman and T.M. Pollock, *Optimal precipitate shapes in nickel-base γ-γ' alloys*, *Acta Materialia* **60** (2012) 1771–1783.

[15] R. Ricks, A. Porter, and R. Ecob, *The growth of γ' precipitates in nickel-base superalloys*, *Acta Metallurgica* **31** (1983), no. 1 43–53.

[16] T.M. Pollock, J. Dibbern, M. Tsunekane, J. Zhu, and A. Suzuki, *New Co-based γ-γ' high-temperature alloys*, *JOM* **62** (2010), no. 1 58–63.

[17] G. Dmitrieva, V. Vasilenko, and I. Melnik, *Al-Co-W Fusion Diagram in the Co-CoAl-W Part*, *Chem. Mater. Alloys* **1** (2008) 338–342.

[18] E. Lass, M. Williams, C. Campbell, K.-W. Moon, and U. Kattner, *γ' phase stability and phase equilibrium in ternary Co-Al-W at 900 °C*, *Journal of Phase Equilibria and Diffusion* **35** (2014), no. 6 711–723.

[19] W. Johnson, *On the inapplicability of Gibbs phase rule to coherent solids*, *Metall. Trans. A* **18A** (1987) 1093–1097.

[20] E. Lass, R. Grist, and M. Williams, *Phase equilibria and microstructural evolution in ternary Co-Al-W between 750 and 1100 °C*, *Journal of Phase Equilibria and Diffusion* **4** (2016) 387–401.

[21] M.S. Titus, A. Suzuki, and T.M. Pollock, *Creep and directional coarsening in single crystals of new γ-γ' cobalt-base alloy*, *Scripta Mater.* **66** (2012) 574–577.

[22] Y. Cui, X. Zhang, G. Xu, W. Zhu, H. Liu, and Z. Jin, *Thermodynamic assessment of Co-Al-W system and solidification of Co-enriched ternary alloys*, *J. Mater. Sci.* **46** (2011) 2611–2621.

[23] S. Yang, M. Jiang, and L. Wang, *Thermodynamic description of the γ' phase in the Co-Al-W based superalloys*, *Mater. Sci. Forum* **747-748** (2013) 654–658.

[24] J. Zhu, M.S. Titus and T.M. Pollock, *Experimental investigation and thermodynamic modeling of the Co-rich region in the Co-Al-W-Ni quaternary system*, *J. Phase Equilibria Diff.* **35** (2014) 595–611.

[25] P. Wang, W. Xiong, U. Kattner, C. Campbell, E. Lass, O. Kontsevoi, and G. Olson, *Thermodynamic re-assessment of the Al-Co-W System*, *Calphad* **59** (2017) 112–130.

[26] J. Bhattacharya and A. Van der Ven, *Phase stability and nondilute Li diffusion in Spinel $Li_{1+x}Ti_2O_4$*, *Physical Review B* **81** (2010).

[27] A. Natarajan and A. Van der Ven, *A unified description of ordering in HCP Mg-RE alloys*, *Acta Materialia* **124** (2017), no. 1.

[28] J. Goiri and A. Van der Ven, *Phase and structural stability in Ni-Al systems from first principles*, *Physical Review B* **94** (2016).

[29] T.M. Pollock and A.S. Argon, *Directional coarsening in nickel-base single crystals with high volume fractions of coherent precipitates*, *Acta Metallurgica et Materialia* **42** (1994), no. 6 1859 – 1874.

[30] R. Reed, N. Matan, D. Cox, M. Rist, and C. Rae, *Creep of CMSX-4 superalloy single crystals: effects of rafting at high temperature*, *Acta Materialia* **47** (1999) 3367–3381.

[31] G. Leverant and B. Kear, *The mechanism of creep in gamma prime precipitation-hardened nickel-base alloys at intermediate temperatures*, *Metall. Trans. A* **B1** (1970) 491–498.

[32] A. Mottura, A. Janotti, and T. M. Pollock, *A first-principles study of the effect of Ta on the superlattice intrinsic stacking fault energy of $L1_2$-$Co_3(Al,W)$*, *Intermetallics* **28** (2012) 138 – 143.

[33] B. Kear, J. Oblak, and A. Giamei, *Stacking faults in gamma prime $Ni_3(Al,Ti)$ precipitation hardened nickel-base alloys*, *Metall. Trans. I* (1970) 2477–2486.

[34] B. Kear, *Dislocation configurations and work hardening in Cu_3Au crystals*, *Acta Metallurgica* **12** (1964) 555–569.

[35] G. Kresse and J. Hafner, *Ab initio molecular dynamics for liquid metals*, *Physical Review B* **47** (1993), no. 558.

[36] G. Kresse and J. Furthmüller, *Efficiency of ab-initio total energy calculations for metals and semiconductors using a plane-wave basis set*, *Computational materials science* **6** (1996), no. 1 15–50.

[37] G. Kresse and J. Furthmüller, *Efficient iterative schemes for ab initio total-energy calculations using a plane-wave basis set*, *Physical Review B* **54** (1996).

[38] P. Blöchl, *Projector augmented-wave method*, *Physical Review B* (1994) 17953–17979.

[39] J. Perdew, K. Burke, and M. Ernzerhof, *Generalized gradient approximation made simple*, *Physical Review Letters* (1996) 3865–3868.

[40] Y. Zhao and D. G. Truhlar, *Construction of a generalized gradient approximation by restoring the density-gradient expansion and enforcing a tight Lieb-Oxford bound*, *The Journal of chemical physics* **128** (2008), no. 18 184109.

[41] J. Sanchez, F. Ducastelle, and D. Gratias, *Generalized cluster description of multicomponent systems*, *Physica A: Statistical Mechanics and its Applications* **128** (1984), no. 1–2 334 – 350.

[42] D. De Fontaine, *Cluster approach to order-disorder transformations in alloys*, *Solid State Physics* **47** (1994) 33–176.

[43] J. Sanchez, *Cluster expansion and the configurational theory of alloys*, *Physical Review B* **81** (2010).

[44] A. Van der Ven, J. Thomas, Q. Xu, and J. Bhattacharya, *Linking the electronic structure of solids to their thermodynamic and kinetic properties*, *Mathematics and Computers in Simulation* **80** (2010), no. 7 1393 – 1410.

[45] B. Puchala and A. Van der Ven, *Thermodynamics of the Zr-O system from first-principles calculations*, *Physical Review B* **88** (2013), no. 9 094108.

[46] J. Thomas and A. Van der Ven, *Finite-temperature properties of strongly anharmonic and mechanically unstable crystal phases from first principles*, *Physical Review B* **88** (2013).

[47] *CASM*, 2015.

[48] G. Hart, V. Blum, M. Walorski, and A. Zunger, *Evolutionary approach for determining first-principles hamiltonians*, *Nature Materials* **4** (2005), no. 5 391–394.

[49] N. Ashcroft and N. Mermin, *Solid State Physics*. Cengage Learning, 1976.

[50] S. Wei and M.Y. Choum, *Ab initio calculation of force constants and full phonon dispersions*, *Phys. Rev. Lett.* **69** (1992) 2799–2802.

[51] M. Born, *Dynamical theory of crystal lattices*. Oxford Univ. Press, 1966.

[52] M.S. Titus, R.K. Rhein, P.B. Wells, P.C. Dodge, G.B. Viswanathan, M.J. Mills, A. Van der Ven, and T.M. Pollock, *Solute segregation and deviation from bulk thermodynamics at nanoscale crystalline defects*, *Science Advances* **2** (2016), no. 12.

[53] H. Suzuki, *Chemical interaction of solute atoms with dislocations*, *Sci. Rep. Res. Inst. Tohoku University* **A4** (1952).

[54] H. Suzuki, *Segregation of solute atoms to stacking faults*, *J. Phys. Soc. Jpn.* **17** (1962) 322–325.

[55] G. Han, I. Jones, and R. Smallman, *Direct evidence for Suzuki segregation and Cottrell pinning in MP159 superalloy obtained by FEG(S)TEM/EDX*, *Acta Materialia* **51** (2003) 2731–2742.

[56] Y. Koizumi, T. Nukaya, S. Suzuki, S. Kurosu, Y. Li, H. Matsumoto, K. Sato, Y. Tanaka, and A. Chiba, *Suzuki segregation in Co-Ni-based superalloy at 973K: An experimental and computational study by phase-field simulation*, *Acta Materialia* **60** (2012), no. 6 2901 – 2915.

[57] F. Xue, H. Zhou, X. Ding, M. Wang, and Q. Feng, *Improved high temperature stabilty of Co-Al-W-base alloys containing Ti and Ta*, *Material Letters* **112** (2013) 215–218.

[58] A. Elliot, *Directional solidification of large cross-section Ni-base superalloy castings via liquid-metal cooling*. PhD thesis, University of Michigan, 2005.

[59] A.J. Elliot, T.M. Pollock, S. Tin, W.T. King, S.C. Huang, and M.F.X. Gigliotti, *Directional solidification of large superalloy castings with radiation and liquid-metal cooling: A comparative assessment*, *Metall. Trans. A* **35** (2004), no. 10 3221–3231.

[60] A.J. Elliot and T.M. Pollock, *Thermal analysis of the Bridgman and liquid-metal-cooled directional solidification investement casting processes*, *Metall. Trans. A* **38** (2007), no. 4 871–882.

[61] C. Jiang, *First-principles study of $Co_3(Al,W)$ alloys using special quasi-random structures*, *Scripta Mater.* (2008) 1075–1078.

[62] S. Miura, K. Ohkuba, and T. Mohri, *Mechanical properties of Co-Based $L1_2$ intermetallic compound $Co_3(Al,W)$*, *Materials Transactions* **48** (2007) 2403–2408.

[63] J. Saal and C. Wolverton, *Thermodynamic stability of Co-Al-W $L1_2$ γ'*, *Acta Materialia* **61** (2013) 2330–2338.

[64] R.K. Rhein, P.C. Dodge, M.H. Chen, M.S. Titus, T.M. Pollock, and A. Van der Ven, *The role of vibrational and configuration excitations in stabilizing the $L1_2$ structure in Co-rich Co-Al-W Alloys*, *Physical Review B* (2015).

[65] A. Bradley and A. Taylor, *An x-ray analysis of the nickel-aluminum system*, *Proceedings of the Royal Academy of London* (1937).

[66] Q. Xu and A. Van der Ven, *First-principles investigation of migration barriers and point defect complexes in B2–NiAl*, *Intermetallics* **17** (2009), no. 5 319–329.

[67] G. Kresse and D. Joubert, *From ultrasoft pseudopotentials to the projector augmented-wave method*, *Phys. Rev. B* **59** (Jan, 1999) 1758–1775.

[68] J. Perdew, A. Ruzsinszky, G. Csonka, O. Vydrov, G. Scuseria, L. Constantin, X. Zhou, and K. Burke, *Restoring the density-gradient expansion for exchange in solids and surfaces*, *Phys. Rev. Lett.* **102** (2008).

[69] A. van de Walle and G. Ceder, *The effect of lattice vibrations on substitutional alloy thermodynamics*, *Reviews of Modern Physics* **74** (2002).

[70] G. Ceder, *A derivation of the Ising model for the computation of phase diagrams*, *Computational Materials Science* **1** (1993) 144–150.

[71] M. Uhl and J. Kübler, *Exchange-coupled spin-fluctuation theory: application to Fe, Co, and Ni*, *Phys. Rev. Lett.* **77** (1996).

[72] Inorganic Crystal Structure Database (ICSD) 2018.

[73] R.K. Rhein, P.G. Callahan, S.P. Murray, J.-C. Stinville, M.S. Titus, A. Van der Ven, and T.M. Pollock, *Creep behavior of quinary γ'-strengthened Co-based superalloys*, *Metall. Trans. A* **49** (2018), no. 9 4090–4098.

[74] F. Xue, H. Zhou, Q. Shi, X. Chen, H. Chang, M. Wang, and Q. Feng, *Creep behavior in a strengthened Co-Al-W-Ta-Ti single-crystal alloy at 1000°C*, *Scripta Materialia* **97** (2015) 37 – 40.

[75] J. Yen, F. Chang, and S. Chang, *A new criterion for automatic multilevel thresholding*, *IEEE Transactions on Image Processing* **4** (1995), no. 3 370–378.

[76] M. Sezgin and B. Sankur, *Survey over image thresholding techniques and quantitative performance evaluation*, *Journal of Electronic Imaging* **13** (2004), no. 1.

[77] C. Schneider, W. Rasband, and K. Eliceiri, *NIH Image to ImageJ: 25 years of image analysis*, *Nature Methods* **9** (2012), no. 7 671–675.

[78] K. Harris, G. Erickson, and R. Schwer, *Development of the single crystal alloys CMSX-2 and CMSX-3 for advanced technology turbine engines*, *ASME 1983 International Gas Turbine Conference and Exhibit* (1983).

[79] D. Frasier, J. Whetstone, K. Harris, G. Erickson, and R. Schwer, *Process and alloy optimization for CMSX-4 superalloy single crystal airfoils*, *Proceedings Part II of Cost Conference* **5** (1990) 1281–1290.

[80] G. Fuchs, *Improvement of creep strength of a third generation, single-crystal Ni-base superalloy by solution heat treatment*, *Journal of Materials Engineering and Performance* (2002).

[81] M. Hebsur and R. Miner, *Elevated temperature tension, compression and creep-rupture behavior of (001)-oriented single crystal superalloy PWA 1480*, *NASA Technical Memorandum 88950* (1987).

[82] A. Suzuki, H. Inui, and T.M. Pollock, *$L1_2$-Strengthened Cobalt-Base Superalloys*, *Annual Review of Materials* **45** (2015) 345–368.

[83] Y.M. Eggeler, M.S. Titus, A. Suzuki, and T.M. Pollock, *Creep deformation-induced antiphase boundaries in $L1_2$-containing single-crystal cobalt-base superalloys*, *Acta Materialia* **77** (2014) 352–359.

[84] M.S. Titus, Y.M. Eggeler, A. Suzuki, and T.M. Pollock, *Creep-induced planar defects in $L1_2$-containing Co- and CoNi-base single crystal superalloys*, *Acta Materialia* (2015) 530–539.

[85] Y.M. Eggeler, J. Muller, M.S. Titus, A. Suzuki, T.M. Pollock, and E. Spiecker, *Planar defect formation in the γ' phase during high temperature creep in single crystal CoNi-base superalloys*, *Acta Materialia* **113** (2016) 335–349.

[86] K. Tanaka, T. Ohashi, K. Kishida, and H. Inui, *Single-crystal elastic constants of $Co_3(Al,W)$ with the $L1_2$ structure*, *Applied Physics Letters* **91** (2007).

[87] S. K. Makineni, A. Kumar, M. Lenz, P. Kontis, T. Meiners, C. Zenk, S. Zaefferer, G. Eggeler, S. Neumeier, E. Spiecker, D. Raabe, and B. Gault, *On the diffusive phase transformation mechanism assisted by extended dislocations during creep of a single crystal CoNi-based superalloy*, *Acta Materialia* **155** (2018) 362–371.

[88] S. Allen and J. Cahn, *A microscopic theory for antiphase boundary motion and its application to antiphase domain coarsening*, *Acta Metallurgica* **27** (1979), no. 6 1085–1095.

[89] K. Shinagawa, T. Omori, J. Sato, K. Oikawa, I. Ohnuma, R. Kainuma, and K. Ishida, *Phase equilibria and microstructure on γ' phase in Co-Ni-Al-W system*, *Materials Transactions* (2008).

[90] V. Vitek, *Intrinsic stacking faults in body-centered cubic crystals*, *Philosophical Magazine* (1968).

[91] J. Hamilton and S. Foiles, *First-principles calculations of grain boundary theoretical shear strength using transition state finding to determine generalized gamma surface cross sections*, *Phys. Rev. B* **65** (2002).

[92] Y. Wang, Y. Jin, A. Cuitino, and A. Khachaturyan, *Nanoscale phase field microelasticity theory of dislocations: model and 3D simulations*, *Acta Materialia* **49** (2001), no. 10 1847–1857.

[93] C. Shen and Y. Wang, *Phase field model of dislocation networks*, *Acta Materialia* **51** (2003), no. 9 2595–2610.

[94] Y. Zhu, X. Liao, X. Wu, and S. Mathaudhu, *Dislocation-twin interactions in nanocrystalline fcc metals*, *Acta Materialia* **59** (2011), no. 2 812–821.

[95] P. Caron, T. Khan, and P. Veyssiere, *On precipitate shearing by superlattice stacking faults in superalloys*, *Philosophical Magazine A* **57** (1988), no. 6 859–875.

[96] G. Viswanathan, R. Shi, A. Genc, V. Vorontsov, L. Kovarik, C. Rae, and M. Mills, *Segregation at stacking faults within the phase of two Ni-base superalloys following intermediate temperature creep*, *Scripta Materialia* **94** (2015) 5 – 8.

[97] T. Smith, B. Esser, N. Antolin, G. Viswanathan, T. Hanlon, A. Wessman, D. Mourer, W. Windl, D. McComb, and M. Mills, *Segregation and phase formation along stacking faults during creep at intermediate temperatures in a Ni-based superalloy*, *Acta Materialia* **100** (2015) 19 – 31.

[98] L. P. Freund, O. M. Messé, J. S. Barnard, M. Göken, S. Neumeier, and C. M. Rae, *Segregation assisted microtwinning during creep of a polycrystalline L12-hardened Co-base superalloy*, *Acta Materialia* **123** (2017) 295 – 304.

[99] A. Suzuki and T. M. Pollock, *High-temperature strength and deformation of / two-phase Co-Al-W-base alloys*, *Acta Materialia* **56** (2008), no. 6 1288 – 1297.

[100] S. Pennycook, *Z-contrast stem for materials science*, *Ultramicroscopy* **30** (1989), no. 1 58 – 69.

[101] B. D. Forbes, A. J. D'Alfonso, R. E. A. Williams, R. Srinivasan, H. L. Fraser, D. W. McComb, B. Freitag, D. O. Klenov, and L. J. Allen, *Contribution of thermally scattered electrons to atomic resolution elemental maps*, *Phys. Rev. B* **86** (Jul, 2012) 024108.

[102] Z. Chen, M. Weyland, X. Sang, W. Xu, J. Dycus, J. LeBeau, A. D'Alfonso, L. Allen, and S. Findlay, *Quantitative atomic resolution elemental mapping via absolute-scale energy dispersive X-ray spectroscopy*, *Ultramicroscopy* **168** (2016) 7 – 16.

[103] F. Vurpillot, D. Larson, and A. Cerezo, *Improvement of multilayer analyses with a three-dimensional atom probe*, *Surface and Interface Analysis* **36** (2004) 552–558.

[104] M. S. Titus, A. Mottura, G. B. Viswanathan, A. Suzuki, M. J. Mills, and T. M. Pollock, *High resolution energy dispersive spectroscopy mapping of planar defects in $L1_2$-containing Co-base superalloys*, *Acta Materialia* **89** (2015) 423 – 437.

[105] J. Hafner, *Materials simulations using VASP-a quantum perspective to materials science*, *Computer Physics Communications* **177** (2007), no. 1 6 – 13. Proceedings of the Conference on Computational Physics 2006.

[106] A. V. der Ven, J. Thomas, Q. Xu, and J. Bhattacharya, *Linking the electronic structure of solids to their thermodynamic and kinetic properties*, *Mathematics and Computers in Simulation* **80** (2010), no. 7 1393 – 1410. Multiscale modeling of moving interfaces in materials.

[107] J. P. Hirth, *Thermodynamics of stacking faults*, *Metallurgical Transactions* **1** (1970), no. 9 2367.

[108] K. Lu, L. Lu, and S. Suresh, *Strengthening materials by engineering coherent internal boundaries at the nanoscale*, *Science* **324** (2009), no. 5925 349–352, [http://science.sciencemag.org/content/324/5925/349.full.pdf].

[109] C.A. Stewart, R.K. Rhein, A. Suzuki, T.M. Pollock, and C.G. Levi, *Oxide scale formation in novel γ-γ' cobalt-based alloys*, *Superalloys 2016* (2016) 991–999.

[110] A. Evans, D. Clarke, and C. Levi, *The influence of oxides on the performance of advanced gas turbines*, *Journal of the European Ceramics Society* **28** (2008) 1405–1419.

[111] A. Beltran, *The oxidation and hot-corrosion resistance of cobalt-base superalloys*, *Cobalt* **46** (1970) 3.

[112] F. Stott, G. Wood, and J. Stringer, *The influence of alloying elements on the development and maintenance of protective scales*, *Oxidation of Metals* **44** (1995) 113–145.

[113] H. Yan, V. Vorontsov, and D. Dye, *Effect of alloying on the oxidation behavior of Co-Al-W superalloys*, *Corrosion Science* **83** (2014) 382–395.

[114] L. Klein, Y. Shen, M. Killian, and S. Virtanen, *Effect of B and Cr on the high temperature oxidation behavior of novel γ/γ Co-base superalloys*, *Corrosion Science* (2011) 2713–2720.

[115] C.A. Stewart, A. Suzuki, T.M. Pollock, and C.G. Levi, *Rapid assessment of oxidation behavior in Co-based γ/γ' alloys*, *Oxidation of Metals* **90** (2018) 485–498.

[116] M.Weiser, Y.M. Eggeler, E. Spiecker, S. Virtanen, *Early stages of scale formation during oxidation of γ/γ' strengthened single crystal ternary Co-base superalloy at 900 °C*, *Corrosion Science* **135** (2018) 78–86.

[117] L. Klein, A. Bauer, S. Neumeier, M. Göken, and S. Virtanen, *High temperature oxidation of γ/γ'-strengthened Co-base superalloys*, *Corrosion Science* **53** (2011), no. 5 2027–2034.

[118] A. Jain, S. Ong, G. Hautier, W. Chen, W. Richards, S. Dacek, S. Cholia, D. Gunter, D. Skinner, G. Ceder, and K. Persson, *Commentary: The Materials Project: A materials genome approach to accelerating materials innovation*, *APL Materials* (2013).

[119] M. Kinoshita, W. Kingery, and H. Bowen, *Phase separation in NiO-CoO solid solution single crystals*, *Journal of the American Ceramic Society* **56** (1973) 398–399.

[120] D. Miracle, J. Miller, O. Senkov, C. Woodward, M. Uchic, and J. Tiley, *Exploration and development of high entropy alloys for structural applications*, *Entropy* **16** (2014) 494–525.

[121] C. Metting, J. Bunn, E. Underwood, S. Smoak, and J. Hattrick-Simpers, *Combinatorial approach to turbine bond coat discovery*, *ACS Comb. Sci.* **15** (2013) 419–424.

[122] R. Adharapurapu, J. Zhu, V. Dheeradhada, D. Lipkin, and T. Pollock, *A combinatorial investigation of palladium and platinum additions to β-NiAl overlay coatings*, *Acta Materialia* **77** (2014) 379–393.

[123] Q. Xu and A. Van der Ven, *Atomic transport in ordered compounds mediated by local disorder: Diffusion in B2 Ni_xAl_{1-x}*, *Phys. Rev. B* **81** (2010).